

# Scattering theory of topological phase transitions

PROEFSCHRIFT

TER VERKRIJGING VAN  
DE GRAAD VAN DOCTOR AAN DE UNIVERSITEIT LEIDEN,  
OP GEZAG VAN RECTOR MAGNIFICUS  
PROF. MR. C. J. J. M. STOLKER,  
VOLGENS BESLUIT VAN HET COLLEGE VOOR PROMOTIES  
TE VERDEDIGEN OP DONDERDAG 21 NOVEMBER 2013  
KLOKKE 16.15 UUR

DOOR

Ion Cosma Fulga

GEBOREN TE BOEKAREST, ROEMENIË IN 1986

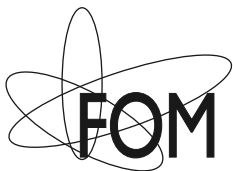
## Promotiecommissie

Promotor: Prof. dr. C. W. J. Beenakker  
Co-promotor: Dr. A. R. Akhmerov (Delft University of Technology)  
Overige leden: Prof. dr. E. R. Eliel  
Dr. V. Vitelli  
Prof. dr. F. Hassler (RWTH Aachen)  
Prof. dr. C. M. Marcus (Kopenhagen University)

Casimir PhD Series, Delft-Leiden, 2013-27  
ISBN 978-90-8593-167-6

Dit werk maakt deel uit van het onderzoekprogramma van de Stichting voor Fundamenteel Onderzoek der Materie (FOM), die deel uit maakt van de Nederlandse Organisatie voor Wetenschappelijk Onderzoek (NWO).

This work is part of the research programme of the Foundation for Fundamental Research on Matter (FOM), which is part of the Netherlands Organisation for Scientific Research (NWO).



Cover: *Trajectories of zeros and poles of the reflection matrix determinant across a topological phase transition in class DIII. Compare with the top right panel of Fig. 3.5.*

*To my parents.*



# Contents

<b>1</b>	<b>Introduction</b>	<b>1</b>
1.1	Preface . . . . .	1
1.2	The scattering matrix . . . . .	3
1.3	Topological invariants . . . . .	5
1.4	Finite size scaling . . . . .	7
1.5	This thesis . . . . .	9
1.5.1	Chapter 2 . . . . .	9
1.5.2	Chapter 3 . . . . .	9
1.5.3	Chapter 4 . . . . .	10
1.5.4	Chapter 5 . . . . .	11
1.5.5	Chapter 6 . . . . .	11
1.5.6	Chapter 7 . . . . .	13
<b>2</b>	<b>Scattering formula for the topological quantum number of a disordered multi-mode wire</b>	<b>19</b>
2.1	Introduction . . . . .	19
2.2	Topological quantum number from reflection matrix . . . . .	20
2.3	Number of end states from topological quantum number .	23
2.3.1	Superconducting symmetry classes . . . . .	23
2.3.2	Chiral symmetry classes . . . . .	26
2.4	Superconducting versus chiral symmetry classes . . . . .	28
2.5	Application to dimerized polymer chains . . . . .	31
2.6	Appendix . . . . .	33
2.6.1	Calculation of the number of end states in class DIII	33
2.6.2	Computing the topological quantum number of a dimerized polymer chain . . . . .	34

<b>3</b>	<b>Scattering theory of topological insulators and superconductors</b>	<b>39</b>
3.1	Introduction . . . . .	39
3.1.1	Dimensional reduction in the quantum Hall effect	40
3.1.2	Outline of the paper . . . . .	41
3.2	Scattering matrix from a Hamiltonian . . . . .	42
3.3	Dimensional reduction . . . . .	46
3.4	Results for one–three dimensions . . . . .	51
3.4.1	Topological invariant in 1D . . . . .	51
3.4.2	Topological invariant in 2D . . . . .	51
3.4.3	Topological invariant in 3D . . . . .	54
3.4.4	Weak invariants . . . . .	55
3.5	Applications and performance . . . . .	56
3.5.1	Performance . . . . .	56
3.5.2	Finite size effects . . . . .	56
3.5.3	Applications . . . . .	58
3.6	Conclusion . . . . .	60
3.7	Appendix . . . . .	61
3.7.1	Introduction to discrete symmetries . . . . .	61
3.7.2	Calculation of the number of poles . . . . .	66
<b>4</b>	<b>Topological quantum number and critical exponent from conductance fluctuations at the quantum Hall plateau transition</b>	<b>71</b>
4.1	Introduction . . . . .	71
4.2	Topological quantum number and conductance resonance	72
4.3	Numerical simulations in a disordered system . . . . .	75
4.4	Discussion and relation to the critical exponent . . . . .	77
4.5	Appendix . . . . .	78
4.5.1	Calculation of the topological quantum number . . . . .	78
4.5.2	Calculation of the critical exponent . . . . .	81
<b>5</b>	<b>Thermal metal-insulator transition in a helical topological superconductor</b>	<b>87</b>
5.1	Introduction . . . . .	87
5.2	Chiral versus helical topological superconductors . . . . .	88
5.3	Class DIII network model . . . . .	91
5.3.1	Construction . . . . .	91
5.3.2	Vortices . . . . .	93
5.3.3	Vortex disorder . . . . .	94
5.4	Topological quantum number and thermal conductance . . . . .	94

5.5	Topological phase transitions . . . . .	96
5.5.1	Phase diagram without disorder . . . . .	96
5.5.2	Scaling of the critical conductivity . . . . .	96
5.5.3	Phase diagram with disorder . . . . .	98
5.5.4	Critical exponent . . . . .	99
5.6	Conclusion . . . . .	100
5.7	Appendix . . . . .	102
5.7.1	Location of the critical point in the network model without disorder . . . . .	102
5.7.2	Finite-size scaling analysis . . . . .	103
<b>6</b>	<b>Adaptive tuning of Majorana fermions in a quantum dot chain</b>	<b>109</b>
6.1	Introduction . . . . .	109
6.2	Generalized Kitaev chain . . . . .	112
6.3	System description and the tuning algorithm . . . . .	113
6.4	Testing the tuning procedure by numerical simulations . . . . .	117
6.5	Conclusion . . . . .	121
6.6	Appendix . . . . .	121
6.6.1	System parameters in numerical simulations . . . . .	121
<b>7</b>	<b>Statistical Topological Insulators</b>	<b>129</b>
7.1	Introduction . . . . .	129
7.2	Construction of an STI topological invariant . . . . .	131
7.3	STIs with reflection symmetry . . . . .	134
7.4	Numerical Simulations . . . . .	134
7.5	Conclusions and discussion . . . . .	138
7.6	Appendix . . . . .	138
7.6.1	Tight-binding construction for statistical topological insulators with reflection symmetry . . . . .	138
7.6.2	Localization on the Majorana triangular lattice by broken statistical reflection symmetry . . . . .	141
	<b>Samenvatting</b>	<b>145</b>
	<b>Summary</b>	<b>147</b>
	<b>List of Publications</b>	<b>151</b>
	<b>Curriculum Vitæ</b>	<b>153</b>





# Chapter 1

## Introduction

### 1.1 Preface

In 1958 Anderson showed that a quantum particle may be localized by disorder, due to the presence of impurities for instance, even if classically localization does not occur [1]. At fixed disorder strength and energy, all quantum states are either localized or delocalized. This insight provides one of the fundamental ingredients for understanding metals and insulators, as well as the transitions that can take place between these states of matter, now known as Anderson transitions [2].

In the decades that followed, metal-insulator transitions were associated with second-order phase transitions by the advent of field-theoretical descriptions of localization [3, 4], as well as the development of one-parameter scaling theory [5]. The latter assumed the existence of a single variable which would describe both the metallic and the insulating properties of a system close to the phase transition. These properties were expected to fall within certain universality classes, in which the behavior of the conductivity and localization length at the critical point would only depend on the dimensionality and symmetries of the system, irrespective of microscopic details.

Besides providing a means of describing the way in which metals turn insulating or vice versa, the scaling theory of localization was also applied to the quantum Hall effect [6]. Systems showing this effect are not metals, but they are not insulating either, exhibiting localized bulk states and extended edge states at the same time. It was nevertheless understood that the transition between different Hall plateaus was a

localization-delocalization transition, which made scaling theory a useful tool in its description. This was unexpected at the time, since the theory in its original form predicted the absence of extended states in two-dimensional systems [5].

In recent years it was realized that the quantum Hall effect is not the only example of a system with an insulating bulk and a conducting edge [7]. In 2005, Kane and Mele showed that graphene in the presence of spin-orbit interaction has robust, extended edge states, protected by time-reversal symmetry [8]. Many proposals followed, making use of spin-orbit interaction, superconductivity, magnetism, and combinations thereof, leading to the rapid development of what is now known as the field of topological insulators and superconductors [9, 10].

Such systems have been predicted to exist in any spatial dimension and are protected by a variety of symmetries, ranging from the originally proposed one, time-reversal, to crystallographic symmetries of the underlying lattice [11], and even symmetries which are not exact, but only present on average (Chapter 7 of this thesis). Several examples have been experimentally observed [12, 13], and the search for potential applications is one of the most active areas of condensed matter research today. Perhaps the most tantalizing is the possibility of using Majorana fermions, edge states which appear in one-dimensional topological superconductors, as the building blocks for decoherence-free quantum computers [14–16].

The discovery of such a wide range of novel phases of matter calls for the characterization of their physical properties, and of the conditions under which they can appear. Transport signatures are experimentally accessible observables, intensely investigated in the search for Majorana fermions [17–19]. Given this connection, it is natural to make use yet again of the scaling theory of localization to describe the nature and universality classes associated with transitions to and between topological phases of matter.

On a more general level, the correspondence between the presence of a bulk insulating gap and conducting boundary states in topological insulators was initially understood in terms of topological band theory [8, 20], which is based on translational symmetry. More often than not however, this symmetry is broken by the presence of impurities, resulting in a disordered system. It is therefore meaningful to seek alternative descriptions, one of which, scattering theory, is the main focus of this

thesis.

In the following, we will provide a brief description of the main tools used throughout this work, such as the scattering matrix, the topological invariant and the scaling theory of localization. While not aiming to be self-contained, it will provide the basic concepts, as well as relevant references.

## 1.2 The scattering matrix

The scattering matrix is one of the central objects of study in this thesis. It can be used to describe many transport features at low temperatures, voltages, and frequencies, whenever interactions between particles are either absent, or treated at the mean-field level [21, 22]. Electronic conduction through a mesoscopic sample can be understood in terms of the transmission probabilities of electrons through a that sample, probabilities which can be determined from the scattering matrix [23–27].

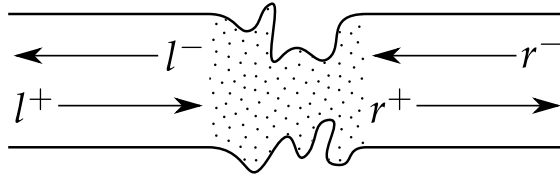


**Figure 1.1.** Central disordered region connected by means of ideal leads to electron reservoirs (not shown). The modes in the left and right leads are labeled with coefficients  $l^\pm$  and  $r^\pm$ , depending on their propagation direction.

To introduce it we will closely follow Ref. [22]. Consider a disordered, phase coherent region connected to two electron reservoirs by means of ideal leads, as shown in Fig. 1.1. Far away from the disordered region, in the translationally invariant ideal leads, the wave function of a particle at the Fermi energy  $E_F$  can be written in terms of the basis states

$$\psi_n^\pm = \phi_n \exp(ik_n x),$$

where  $\phi_n$  is the transversal component,  $k$  is the momentum along the translationally invariant direction of the lead, and  $n = 1, \dots, N$  indexes the states, also known as propagating modes, or scattering channels. Particles incident on the disordered region both from the left and right

leads of Fig. 1.1, can be expressed in this basis in terms of coefficients, which we group in the vector

$$\psi_{\text{in}} = (l_1^+, \dots, l_N^+, r_1^-, \dots, r_N^-)^T.$$

Here,  $\pm$  denotes the sign of the state's velocity, and  $T$  stands for transposition. In an analogous fashion, particles leaving the disordered region can also be characterized by a vector of coefficients:

$$\psi_{\text{out}} = (l_1^-, \dots, l_N^-, r_1^+, \dots, r_N^+)^T.$$

The scattering matrix relates the vectors  $\psi_{\text{in}}$  and  $\psi_{\text{out}}$ :

$$\psi_{\text{out}} = S\psi_{\text{in}}.$$

It is common to express it in terms of its block structure,

$$S = \begin{pmatrix} r & t \\ t' & r' \end{pmatrix}, \quad (1.1)$$

where  $r$  ( $r'$ ) contain the probability amplitudes for a particle to be reflected back into the left (right) lead, and  $t'$ ,  $t$  are composed of probability amplitudes for transmission from left to right and vice versa. The matrix  $S$  is unitary, meaning that its adjoint is equal to its inverse,  $S^\dagger = S^{-1}$ , owing to current conservation. It is also subjected to other constraints depending on the symmetries of the scattering region, many of which are highlighted in Chapters 2 and 3.

Conductance at zero temperature can be written in terms of the transmission probability of electrons through a sample

$$G = G_0 \text{tr} tt^\dagger = G_0 \text{tr} t't'^\dagger, \quad (1.2)$$

where the second equality sign is a consequence of the unitarity of  $S$ , and  $G_0$  is the conductance quantum, which in the case of electrical transport is  $e^2/h$ .

Expressions like Eq. (1.2) carry over also to the case of superconductors, where charge is not a good quantum number, and  $G$  then refers to heat conductance through the sample. Finally, the block structure of  $S$  can be further exploited to analyze specific scattering processes.

An example used in this thesis is Andreev conductance [28], the charge transfer process by which a current in the metallic lead is converted to a supercurrent in the superconducting region. To express it

in terms of the scattering matrix, it is convenient to introduce an additional grading and consider scattering processes of electrons and holes separately. Each of the reflection blocks in Eq. (1.1) then reads

$$r = \begin{pmatrix} r_{ee} & r_{eh} \\ r_{he} & r_{hh} \end{pmatrix}, \quad (1.3)$$

where  $r_{ee(hh)}$  represent the usual electron (hole) reflection. The off-diagonal blocks  $r_{eh(he)}$  describe the process of Andreev reflection, by which an incoming electron is converted into a Cooper pair inside the superconductor, and a hole is reflected back out. Given this grading, the Andreev conductance is written as [29, 30]

$$G/G_0 = N - \text{tr } r_{ee} r_{ee}^\dagger + \text{tr } r_{eh} r_{eh}^\dagger \quad (1.4)$$

with  $N$  the number of propagating modes in the metallic lead.

In Chapter 6, Andreev conductance is used to adaptively tune a system to a spot in parameter space where the topologically non-trivial phase is most robust.

### 1.3 Topological invariants

A system is called a topologically non-trivial insulator (or superconductor) whenever it is insulating in the bulk, but has a fixed number of gapless states at its surface. These conducting boundary states are *topologically protected*, which means that deformations of the system or its parameters will not remove any of them as long as the bulk stays insulating, and as long as certain symmetries are preserved.

The first known example of such a system is the integer quantum Hall effect [31]. When a two-dimensional electron gas is subjected to a strong magnetic field, the quantized electron cyclotron orbits lead to the formation of highly degenerate energy levels, called Landau levels. Whenever the Fermi energy lies between two levels, the bulk of the system is insulating. However, the edges are not. one way to visualize this behavior is to imagine classical trajectories of electrons close to the boundary, called *skipping orbits* (see Fig. 1.2).

A remarkable feature of these systems is that the existence and robustness of the conducting edge states is actually a property of the insulating bulk. This bulk-boundary correspondence ensures that even

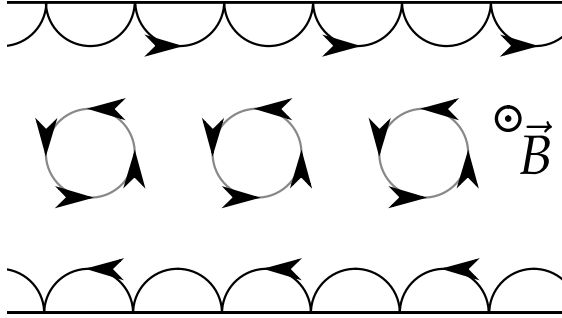


**Figure 1.2.** Two-dimensional electron gas placed in a strong magnetic field  $\vec{B}$ . The electrons in the center of the sample have localized, classical cyclotron orbits, whereas those close to the boundary reflect off of it, forming so called skipping orbits which contribute to transport.

if the system is cut into multiple pieces, as long as the bulk gap is not closed, then each individual piece will behave just like the whole, having conducting states along its surface.

It is natural to ask whether one can write down an expression which counts the number of edge states starting only from the bulk. In 1982, Thouless, Kohmoto, Nightingale, and den Nijs did just that [32], deriving a quantity now known as the TKNN invariant. Given a translationally invariant two-dimensional bulk characterized by Bloch wave functions  $|u_\alpha(\mathbf{k})\rangle$ , this integer, also known as the Chern number, reads

$$n_\alpha = \frac{1}{2\pi} \int d^2\mathbf{k} \nabla \times i \langle u_\alpha(\mathbf{k}) | \nabla_{\mathbf{k}} | u_\alpha(\mathbf{k}) \rangle. \quad (1.5)$$

Physically, the above quantity may be understood in terms of the Berry phase [33] of the wave functions  $|u_\alpha(\mathbf{k})\rangle$ . When adiabatically evolved over a closed loop in momentum space, they acquire a geometric phase given by

$$\gamma_\alpha = \oint_{\mathcal{C}} d\mathbf{k} \cdot i \langle u_\alpha(\mathbf{k}) | \nabla_{\mathbf{k}} | u_\alpha(\mathbf{k}) \rangle.$$

When the contour of integration  $\mathcal{C}$  extends over the entire Brillouin zone, one can use Stokes' theorem to express it as a surface integral over the Brillouin zone, which leads to the expression (1.5).

It is now known that the quantum Hall effect is but one of multiple possible topological insulators. This has triggered an active interest

in finding new expressions for topological invariants which would apply to these new systems, in finding more efficient expressions, or even approximations. The main focus of Chapters 2 and 3 is to write down expressions for topological invariants which can be efficiently evaluated, and which do not require translational invariance.

## 1.4 Finite size scaling

According to the single parameter scaling hypothesis [5], the conductance of a system having a linear size  $L$  depends on all microscopic details through a single quantity,  $\xi$ . This parameter is called correlation length, or localization length, depending on whether one describes a metal or an insulator. The dimensionless conductance is a function of the ratio between these lengths,  $g(L/\xi)$ , given a dimensionality and a set of symmetries obeyed by the system. With varying system size, the flow of the dimensionless conductance can be described within the scaling theory of localization by the equation

$$\frac{d \ln g}{d \ln L} = \beta(g). \quad (1.6)$$

In other words, the logarithmic derivative of the conductance depends on the conductance itself, and the functional form of this dependence is given by the *beta function*,  $\beta(g)$ .

In metals, larger samples will exhibit more conductance, meaning  $\beta > 0$ , while in insulators  $g \sim \exp(-L/\xi)$  (and therefore  $\beta < 0$ ), since all wave functions are localized as

$$|\psi(\mathbf{r})|^2 \sim \exp(-|\mathbf{r} - \mathbf{r}_0|/\xi). \quad (1.7)$$

This implies that exactly at the transition between an insulating and a metallic phase,  $\beta = 0$  and the conductance of the system, called *critical conductance*, is scale invariant. Additionally, the localization length  $\xi$  of Eq. (1.7) must diverge at the transition point, its behavior being parametrized by a *critical exponent*,  $\nu$ . For a system parameter  $\alpha$  (strength of disorder, chemical potential, etc.) that tunes between a metallic and an insulating phase, with a transition at the critical point  $\alpha_c$ , the localization length diverges as one approaches the transition as

$$\xi \sim |\alpha - \alpha_c|^{-\nu}. \quad (1.8)$$

One expects the critical exponent  $\nu$  to be universal, meaning that for a given dimensionality and set of system symmetries, it should not depend on microscopic details.

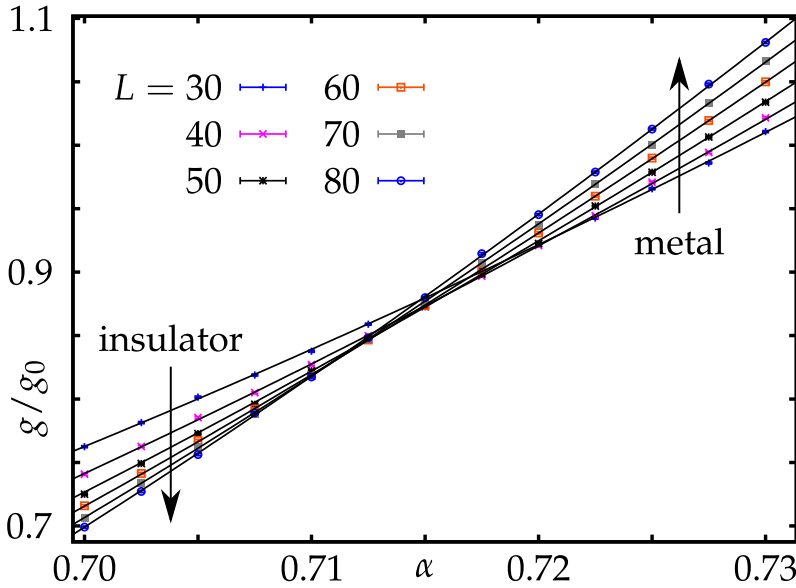


**Figure 1.3.** Conductance of the model studied in Chapter 5 as a function of a parameter tuning through a metal to insulator phase transition,  $\alpha$ . On the left side of the plot, the conductance decreases with system size,  $\beta < 0$ , so the system is in an insulating phase, whereas on the right side it shows the opposite behavior,  $\beta > 0$ , indicating a metallic phase. The curves do not intersect at the same point on the plot due to finite size corrections. This apparent shift in the value of the transition point needs to be taken into account when fitting the data (black lines).

The single parameter scaling hypothesis however is only valid in the limit of large system sizes, and in practice finite size corrections can occur [34]. They may manifest themselves as apparent shifts in the values of the critical point  $\alpha_c$  and of the critical conductance as a function of  $L$  (see Fig. 1.3). Whenever they appear, an accurate determination of the universal properties of a phase transition requires systematically taking these corrections into account. This should be done by considering both the effect of non-linearities on the relevant scaling variable, and the presence of irrelevant scaling variables, which vanish in the large  $L$  limit.

In Chapters 4 and 5, two transitions are considered, and the critical



exponent is computed for each one.

## 1.5 This thesis

In the following, we will give a brief summary of the contents of each thesis chapter.

### 1.5.1 Chapter 2

The topological quantum number  $\mathcal{Q}$  of a superconducting or chiral insulating wire counts the number of protected bound states at the end points. We determine  $\mathcal{Q}$  from the matrix  $r$  of reflection amplitudes from one of the ends, generalizing the known result in the absence of time-reversal and chiral symmetry to all five topologically non-trivial symmetry classes.

The formula takes the form of the determinant, Pfaffian, or matrix signature of  $r$ , depending on whether  $r$  is a real matrix, a real antisymmetric matrix, or a Hermitian matrix. We apply this formula to calculate the topological quantum number of  $N$  coupled dimerized polymer chains, including the effects of disorder in the hopping constants.

The scattering theory relates a topological phase transition to a conductance peak of quantized height and with a universal (symmetry class independent) line shape. Two peaks which merge are annihilated in the superconducting symmetry classes, while they reinforce each other in the chiral symmetry classes.

### 1.5.2 Chapter 3

The topological invariant of a topological insulator (or superconductor) is given by the number of symmetry-protected edge states present at the Fermi level. Despite this fact, established expressions for the topological invariant require knowledge of all states below the Fermi energy.

Here we propose a way to calculate the topological invariant employing solely its scattering matrix at the Fermi level, without knowledge of the full spectrum. Generalizing the work done in Chapter 2 for quantum wires, we provide a dimensional reduction recipe which allows to compute topological invariants in higher dimensions.

The approach based on scattering matrices requires much less information than Hamiltonian-based approaches (surface versus bulk), so it is numerically more efficient. Since our formulation is not based on translational symmetry, as is the case when using topological band theory, it is also more naturally suited to the study of disordered systems. Additionally, it provides a direct connection between the topological invariant of a system and its transport properties, leading to novel signatures of topological phase transitions, as will be discussed in the next chapter.

Finally, this method provides us with a new way of visualizing topological phase transitions. In many cases, the invariant can be determined by examining the zeros and poles of the reflection matrix determinant,  $\det r$ , when applying twisted boundary conditions to the system. Across the phase transition, capturing the evolution of the zeros and poles, in movie format for instance [35], allows to determine “by eye” the symmetries of the system, the point at which the invariant changes, as well as possible re-entrant behavior.

### 1.5.3 Chapter 4

The conductance of a two-dimensional electron gas at the transition from one quantum Hall plateau to the next has sample-specific fluctuations as a function of magnetic field and Fermi energy. Here we identify a universal feature of these mesoscopic fluctuations in a Corbino geometry: The amplitude of the magnetoconductance oscillations has an  $e^2/h$  resonance in the transition region, signaling a change in the topological quantum number of the insulating bulk.

One way of understanding how this occurs relates back to the previous chapter. The change of invariant across the plateau transition can be visualized in terms of the evolution of the zeros and poles of  $\det r$  under twisted boundary conditions. A zero implies the existence of a fully transmitted bulk mode, which passes through the system exactly at the phase transition point, for the right twist angle.

In a Corbino geometry, varying the magnetic field and Fermi energy, besides tuning through plateau transitions, also has the effect of winding the twist angle. Therefore, along each line separating different quantum Hall phases there is a quasi-periodic conductance resonance, corresponding to the fully transmitted bulk mode.

This resonance also provides a scaling variable for the critical exponent of the phase transition. By looking at  $\det r$  and its zeros, one can determine when the phase transition happens and on which side of the transition the system is. Using this information, we construct a scaling variable which is signed, in contrast to the positive-definite ones usually studied in the context of the quantum Hall effect (the conductance or Lyapunov exponents). Remarkably, the scaling variable yields a value for the critical exponent consistent with previous work, but without the need to correct for finite size effects in the form of irrelevant exponents.

### 1.5.4 Chapter 5

Two-dimensional superconductors with time-reversal symmetry have a  $\mathbb{Z}_2$  topological invariant, that distinguishes phases with and without helical Majorana edge states.

In this chapter we perform conductance scaling with varying system size using a model belonging to symmetry class DIII, in order to map its phase diagram. The latter consists of insulating regions, where the thermal conductance decreases with increasing system size, separated by metallic ones, in which larger samples have more conductance.

Using single parameter scaling theory, we determine the universal features across the metal-insulator transitions, finding a critical exponent  $\nu \approx 2.0$ , about twice the known value in a chiral superconductor. In order to give an accurate estimate, we take into account finite size effects both in the form of non-linearities of the relevant scaling variable, as well as in irrelevant scaling exponents.

Transport properties determine both the phase diagram, as well as the universal features of the model. Additionally, given the results of Chapter 3, they also allow us to compute the topological invariant. Therefore, the system we study is introduced directly in terms of its scattering matrix, as opposed to a tight-binding model: it is a *network model*.

### 1.5.5 Chapter 6

As mentioned previously, one of the most sought after applications of topological superconductors is the use of Majorana fermions, particles which are their own anti-particles, as building blocks for quantum

computers. Majoranas were predicted to occur as end states of one-dimensional topological superconductors, and could be identified by their transport signature: a conductance peak at zero bias voltage. There are many theoretical proposals to realize them, and recent experimental works have observed a zero bias peak in superconducting quantum wires (see Fig.1.4).

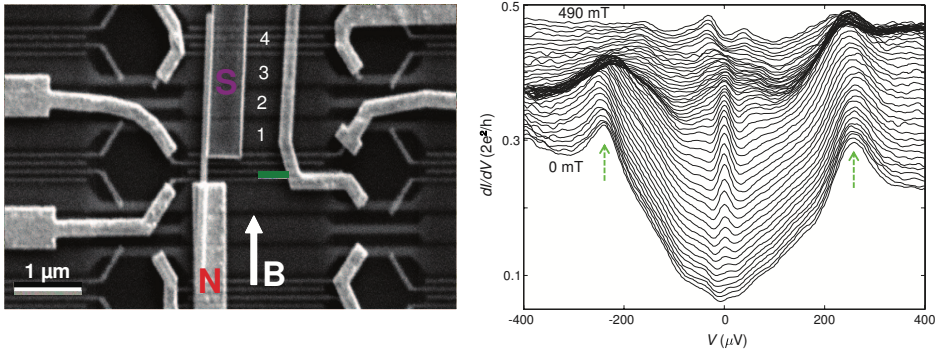


**Figure 1.4.** Left panel: experimental setup, showing a nanowire coupled to a superconductor (S) and subjected to an external magnetic field (B). A normal metal lead (N) is attached, so that conductance measurements can be performed. Right panel: conductance of the system as a function of bias voltage, for different magnetic field strengths. For a range of magnetic fields, the curves show a zero bias peak, an indicator for Majorana fermions. Taken from Ref. [17], and reproduced with permission from AAAS.

However, given the complex, hard to tune, disordered nature of the considered systems, it is hard to identify this peak exclusively with Majorana physics. Several proposals exist which reproduce similar transport signatures in the absence of topologically protected end states.

We propose a way of overcoming these obstacles by constructing a one-dimensional topological superconductor in a bottom-up fashion, as a linear array of quantum dots. In this way, we gain the ability to separately tune each dot, as well the coupling between them. With a high degree of control over system sub-components, one can unambiguously tune the system to a point deep in the non-trivial phase, with well-localized Majorana fermions at its ends.

In our setup, conductance measurements serve not only to indicate the presence of Majoranas, but are a vital part of the tuning process. Andreev conductance spectroscopy tells us how each sub-component

behaves, and which parameters to address at every step of the adaptive tuning procedure.

### 1.5.6 Chapter 7

The quantum Hall effect studied in Chapter 4 has topologically protected edge states, in the sense that a perturbation cannot remove these states as long as the bulk gap is maintained. Such a definition carries over to other topological insulators, but additionally requires that system symmetries be preserved. For example, the model studied in Chapter 5 is protected by both particle-hole and time-reversal symmetry. If any of the two is broken, then it becomes possible to smoothly deform the system and remove the edge states.

In this chapter, we study the robustness of edge states when the symmetries protecting them are broken. The question is of particular significance in the case of topological insulators protected by symmetries of the lattice: translations, mirror, or rotations for instance. In any realistic experimental setup, impurities will lead to a breaking of lattice symmetries, and therefore also of edge state protection.

Remarkably, we find that the edge states survive as long as the symmetry is preserved on average. This allows us to define a class of insulators with gapless surface states protected from localization due to the statistical properties of a disordered ensemble, rather than the exact symmetries of each individual sample.

We show that these insulators are topological, being characterized by a  $\mathbb{Z}_2$  invariant, and provide a general recipe for their construction using an average mirror symmetry. This significantly extends the list of possible non-trivial phases, as every topological insulator gives rise to an infinite number of classes of “statistical topological insulators” in higher dimensions.



# Bibliography

- [1] P. W. Anderson, *Phys. Rev.* **109**, 1492 (1958).
- [2] F. Evers and A. D. Mirlin, *Rev. Mod. Phys.* **80**, 1355 (2008).
- [3] P. A. Lee and T. V. Ramakrishnan, *Rev. Mod. Phys.* **57**, 287 (1985).
- [4] B. Kramer and A. MacKinnon, *Rep. Prog. Phys.* **56**, 1469 (1993).
- [5] E. Abrahams, P. W. Anderson, D. C. Licciardello, and T. V. Ramakrishnan, *Phys. Rev. Lett.* **42**, 673 (1979).
- [6] B. Huckestein, *Rev. Mod. Phys.* **67**, 357 (1995).
- [7] S. Ryu, A. Schnyder, A. Furusaki, and A. Ludwig, *New J. Phys.* **12**, 065010 (2010).
- [8] C.L. Kane and E.J. Mele, *Phys. Rev. Lett.* **95**, 226801 (2005).
- [9] M. Z. Hasan and C. L. Kane, *Rev. Mod. Phys.* **82**, 3045 (2010).
- [10] X.-L. Qi and S.-C. Zhang, *Rev. Mod. Phys.* **83**, 1057 (2011).
- [11] L. Fu, *Phys. Rev. Lett.* **106**, 106802 (2011).
- [12] M. König, S. Wiedmann, Christoph Brüne, A. Roth, H. Buhmann, L. W. Molenkamp, X.-L. Qi, and S.-C. Zhang, *Science* **318**, 766 (2007).
- [13] D. Hsieh, D. Qian, L. Wray, Y. Xia, Y. S. Hor, R. J. Cava, and M. Z. Hasan, *Nature* **452**, 970 (2008).
- [14] C. Nayak, S. H. Simon, A. Stern, M. Freedman, S. Das Sarma, *Rev. Mod. Phys.* **80**, 1083 (2008) .
- [15] J. Alicea, *Rep. Prog. Phys.* **75**, 076501 (2012).

- 
- [16] C. W. J. Beenakker, *Annu. Rev. Con. Mat. Phys.* **4**, 113 (2013).
- [17] V. Mourik, K. Zuo, S. M. Frolov, S. R. Plissard, E. P. A. M. Bakkers, and L. P. Kouwenhoven, *Science* **336**, 1003 (2012).
- [18] M. T. Deng, C. L. Yu, G. Y. Huang, M. Larsson, P. Caroff, and H. Q. Xu, *Nano Lett.* **12**, 6414 (2012).
- [19] A. Das, Y. Ronen, Y. Most, Y. Oreg, M. Heiblum, and H. Shtrikman, *Nat. Phys.* **8**, 887 (2012).
- [20] B. A. Bernevig, T. L. Hughes, and S. C. Zhang, *Science* **314** (2006).
- [21] C.W.J. Beenakker and H. van Houten, *Solid State Physics* **44**, 1 (1991).
- [22] C. W. J. Beenakker, *Rev. Mod. Phys.* **69**, 731 (1997).
- [23] R. Landauer, *IBM J. Res. Dev.* **1**, 223 (1957).
- [24] R. Landauer, *Z. Phys. B* **68**, 217 (1987).
- [25] Y. Imry, *Directions in Condensed Matter Physics*, World Scientific, Singapore (1986).
- [26] M. Büttiker, *Phys. Rev. Lett.* **57**, 1761 (1986).
- [27] M. Büttiker, *IBM J. Res. Dev.* **32**, 317 (1988).
- [28] A. F. Andreev, *Sov. Phys. JETP* **19**, 1228 (1964).
- [29] A. L. Shelankov, *JETP Lett.* **32**, 122 (1980).
- [30] G. E. Blonder, M. Tinkham, and T. M. Klapwijk, *Phys. Rev. B* **25**, 4515 (1982).
- [31] K. von Klitzing, G. Dorda, and M. Pepper, *Phys. Rev. Lett.* **45**, 494 (1980).
- [32] D. J. Thouless, M. Kohmoto, M. P. Nightingale, and M. den Nijs, *Phys. Rev. Lett.* **49**, 405 (1982).
- [33] M. V. Berry, *Proc. R. Soc. Lond. A* **392**, 45 (1984).
- [34] K. Slevin and T. Ohtsuki, *Phys. Rev. Lett.* **82**, 382 (1999) .



- 
- [35] Movies of the zeros and poles of the reflection matrix determinant in three different symmetry classes, across their respective phase transitions, can be found at <http://arxiv.org/src/1106.6351v4/anc>. A detailed explanation can be found in Chapter 3.



## Chapter 2

# Scattering formula for the topological quantum number of a disordered multi-mode wire

### 2.1 Introduction

The bulk-boundary correspondence in the quantum Hall effect equates the number  $\mathcal{Q}$  of occupied Landau levels in the two-dimensional bulk to the number of propagating states at the edge, which is the quantity measured in electrical conduction [1, 2]. Thouless *et al.* identified  $\mathcal{Q}$  as a topological quantum number [3], determined by an invariant integral of the Hamiltonian  $H(k)$  over the Brillouin zone.

One-dimensional wire geometries can also be classified by a topological quantum number, which then counts the number of stable (“topologically protected”) bound states at the end points. Examples exist in chiral insulators (such as a dimerized polyacetylene chain [4]) and in superconductors (such as a chiral  $p$ -wave wire [5]). In the former case the end states are half-integer charged solitons, in the latter case they are charge-neutral Majorana fermions.

Following the line of thought from the quantum Hall effect, one might ask whether the number  $\mathcal{Q}$  of these end states can be related to a transport property (electrical conduction for the insulators and thermal

conduction for the superconductors). The basis for such a relationship would be an alternative formula for  $\mathcal{Q}$ , not in terms of  $H(\mathbf{k})$  [5–10], but in terms of the scattering matrix  $S$  of the wire, connected at the two ends to electron reservoirs.

This analysis was recently carried out for the superconducting  $p$ -wave wire [11], which represents one of the five symmetry classes with a topologically nontrivial phase in a wire geometry [12, 13]. In this paper we extend the scattering theory of the topological quantum number to the other four symmetry classes, including the polyacetylene chain as an application.

The outline is as follows. In the next section we show how to construct a topological invariant  $\mathcal{Q}$  from the reflection matrix  $r$  (which is a subblock of  $S$ ). Depending on the presence or absence of particle-hole symmetry, time-reversal symmetry, spin-rotation symmetry, and chiral (or sublattice) symmetry, this relation takes the form of a determinant, Pfaffian, or matrix signature (being the number of negative eigenvalues), see Table 2.1. In Sec. 2.3 we demonstrate that this  $\mathcal{Q}$  indeed counts the number of topologically protected end states. The connection to electrical or thermal conduction is made in Sec. 2.4, where we contrast the effect of disorder on the conductance in the superconducting and chiral insulating symmetry classes. We conclude in Sec. 2.5 with the application to polyacetylene.

## 2.2 Topological quantum number from reflection matrix

The classification of topological phases is commonly given in terms of the Hamiltonian of a closed system [14]. For the open systems considered here, the scattering matrix provides a more natural starting point. In an  $N$ -mode wire the scattering matrix  $S$  is a  $2N \times 2N$  unitary matrix, relating incoming to outgoing modes. The presence or absence, at the Fermi energy  $E_F$ , of particle-hole symmetry, time-reversal symmetry, spin-rotation symmetry, and chiral (or sublattice) symmetry restricts  $S$  to one of ten subspaces of the unitary group  $\mathcal{U}(2N)$ . In a one-dimensional wire geometry, five of these Altland-Zirnbauer symmetry classes [15] can be in a topological phase, distinguished by an integer-valued quantum number  $\mathcal{Q}$ .

The symmetries of the scattering matrix in the five topological sym-

symmetry class	D	DIII	BDI	AIII	CII
topological phase	$\mathbb{Z}_2$	$\mathbb{Z}_2$	$\mathbb{Z}$	$\mathbb{Z}$	$\mathbb{Z}$
particle-hole symmetry	$S = S^*$			$\times$	$S = \Sigma_y S^* \Sigma_y$
time-reversal symmetry	$\times$	$S = -S^T$	$S = S^T$	$\times$	$S = \Sigma_y S^T \Sigma_y$
spin-rotation symmetry	$\times$		$\checkmark$	$\checkmark$ or $\times$	$\times$
chiral symmetry	$\times$	$S^2 = -1$	$S^2 = 1$		
reflection matrix	$r = r^*$	$r = r^* = -r^T$	$r = r^* = r^T$	$r = r^T$	$r = r^T = \Sigma_y r^T \Sigma_y$
topological quantum number	sign Det $r$	sign Pf $ir$	$\nu(r)$	$\nu(r)$	$\frac{1}{2}\nu(r)$

**Table 2.1.** Classification of the symmetries of the unitary scattering matrix  $S$  at the Fermi level in an  $N$ -mode wire geometry, and relation between the topological quantum number  $Q$  and the reflection submatrix  $r$ . For  $\mathbb{Z}_2$  topological phases  $Q$  is given in terms of the sign of the determinant (Det) or Pfaffian (Pf) of  $r$ . For  $\mathbb{Z}$  topological phases the relation is in terms of the number  $\nu$  of negative eigenvalues of  $r$ .

metry classes are summarized in Table 2.1. For each class we have chosen a basis for the incoming and outgoing modes at the Fermi level in which the symmetry relations have a simple form. (In the next section we will be more specific about the choice of basis.) Notice that the chiral symmetry operation is the combination of particle-hole and time-reversal symmetry (if both are present).

Topological phases are characterized by a resonance at the Fermi level, signaling the presence of one or more quasi-bound states at the end-points of the wire with vanishingly small excitation energy. (If the wire is superconducting, these excitations are Majorana fermions [5].) It is therefore natural to seek a relation between the topological quantum number  $Q$  and the reflection matrix, which is an  $N \times N$  submatrix relating incoming and reflected modes from one end of the wire,

$$S = \begin{pmatrix} r & t' \\ t & r' \end{pmatrix}. \quad (2.1)$$

The wire has two ends, so there are two reflection matrices  $r$  and  $r'$ . Unitarity ensures that the Hermitian matrix products  $rr^\dagger$  and  $r'r'^\dagger$  have the same set of reflection eigenvalues  $\tanh^2 \lambda_n \in (0, 1)$ , numbered by the mode index  $n = 1, 2, \dots, N$ . The real number  $\lambda_n$  is the so-called Lyapunov exponent. The transmission eigenvalues  $T_n = 1 - \tanh^2 \lambda_n = 1/\cosh^2 \lambda_n$  determine the conductance  $G \propto \sum_n T_n$  of the wire. (Depending on the system, this can be a thermal or an electrical conductance.) The topological phases have an excitation gap, so the  $T_n$ 's are exponentially small in general, except when the gap closes at a transi-

tion between two topological phases. A topological phase transition can therefore be identified by a sign change of a Lyapunov exponent [16–19].

The Lyapunov exponents are the radial variables of the polar decomposition of the scattering matrix, given by [20]

$$S = \begin{pmatrix} O_1 & 0 \\ 0 & O_2 \end{pmatrix} \begin{pmatrix} \tanh \Lambda & (\cosh \Lambda)^{-1} \\ (\cosh \Lambda)^{-1} & -\tanh \Lambda \end{pmatrix} \begin{pmatrix} O_3 & 0 \\ 0 & O_4 \end{pmatrix} \quad (2.2a)$$

in class D,

$$S = \begin{pmatrix} O_1 & 0 \\ 0 & O_2 \end{pmatrix} \begin{pmatrix} (\tanh \Lambda) \otimes i\sigma_y & (\cosh \Lambda)^{-1} \otimes i\sigma_y \\ (\cosh \Lambda)^{-1} \otimes i\sigma_y & -(\tanh \Lambda) \otimes i\sigma_y \end{pmatrix} \begin{pmatrix} O_1^T & 0 \\ 0 & O_2^T \end{pmatrix} \quad (2.2b)$$

in class DIII,

$$S = \begin{pmatrix} O_1 & 0 \\ 0 & O_2 \end{pmatrix} \begin{pmatrix} \tanh \Lambda & (\cosh \Lambda)^{-1} \\ (\cosh \Lambda)^{-1} & -\tanh \Lambda \end{pmatrix} \begin{pmatrix} O_1^T & 0 \\ 0 & O_2^T \end{pmatrix} \quad (2.2c)$$

in class BDI,

$$S = \begin{pmatrix} U_1 & 0 \\ 0 & U_2 \end{pmatrix} \begin{pmatrix} \tanh \Lambda & (\cosh \Lambda)^{-1} \\ (\cosh \Lambda)^{-1} & -\tanh \Lambda \end{pmatrix} \begin{pmatrix} U_1^\dagger & 0 \\ 0 & U_2^\dagger \end{pmatrix} \quad (2.2d)$$

in class AIII,

$$S = \begin{pmatrix} Q_1 & 0 \\ 0 & Q_2 \end{pmatrix} \begin{pmatrix} (\tanh \Lambda) \otimes \sigma_0 & (\cosh \Lambda)^{-1} \otimes \sigma_0 \\ (\cosh \Lambda)^{-1} \otimes \sigma_0 & -(\tanh \Lambda) \otimes \sigma_0 \end{pmatrix} \begin{pmatrix} Q_1^\dagger & 0 \\ 0 & Q_2^\dagger \end{pmatrix} \quad (2.2e)$$

in class CII, in terms of a real diagonal matrix  $\Lambda = \text{diag}(\lambda_1, \lambda_2, \dots)$  and complex unitary matrices  $U_p$  (satisfying  $U_p^{-1} = U_p^\dagger$ ), real orthogonal matrices  $O_p$  (satisfying  $O_p^{-1} = O_p^\dagger = O_p^T$ ), and quaternion symplectic matrices  $Q_p$  (satisfying  $Q_p^{-1} = Q_p^\dagger = \Sigma_y Q_p^T \Sigma_y$ ). The matrices  $\Sigma_i = \sigma_i \oplus \sigma_i \oplus \dots \oplus \sigma_i$  are block diagonal in terms of  $2 \times 2$  Pauli matrices  $\sigma_i$  (with  $\sigma_0$  the  $2 \times 2$  unit matrix). There are  $N$  distinct  $\lambda_n$ 's in classes D, BDI, and AIII, but only  $N/2$  in classes DIII and CII (because of a twofold Kramers degeneracy of the transmission eigenvalues).

The transmission eigenvalues only determine the Lyapunov exponents up to a sign. To fix the sign, we demand in class D and DIII that  $\text{Det } O_p = 1$ , so  $O_p \in \text{SO}(N)$ . Then the  $\lambda_n$ 's can be ordered uniquely as [19]  $|\lambda_1| < \lambda_2 < \lambda_3 < \dots$ , so there can be at most a single negative Lyapunov exponent. In the other three classes there is no sign ambiguity since  $\tanh \lambda_n$  is an eigenvalue of the reflection matrix  $r$  itself —

which is a Hermitian matrix in classes BDI, AIII, and CII. There is then no constraint on the number of negative Lyapunov exponents [16].

If we start from an initial state with all  $\lambda_n$ 's positive, then the number  $\mathcal{Q}$  of (distinct) negative Lyapunov exponents in a final state counts the number of topological phase transitions that separate initial and final states. In class D this produces the relation  $\mathcal{Q} = \text{sign Det } r$  from Refs. 18, 11, relating topological quantum number and determinant of reflection matrix.

In class DIII the determinant of  $r$  is always positive, but we can use the Pfaffian of the antisymmetric reflection matrix to count the number of negative  $\lambda_n$ 's, so we take  $\mathcal{Q} = \text{sign Pf } r$ . [In view of the identity  $\text{Pf } XYX^T = (\text{Det } X)(\text{Pf } Y)$ , one has  $\text{Pf } r = (\text{Det } O_1)\text{Pf } (\Lambda \otimes i\sigma_y) = \prod_n \tanh \lambda_n$ .]

In classes BDI and AIII the matrix signature  $\mathcal{Q} = \nu(r)$  of the Hermitian matrix  $r$  gives the number of negative eigenvalues, equal to the number of negative  $\lambda_n$ 's. In class CII we take  $\mathcal{Q} = \frac{1}{2}\nu(r)$  to obtain the number of distinct negative  $\lambda_n$ 's, because each eigenvalue is twofold degenerate.

These topological quantum numbers are defined relative to a particular reference state, chosen to have all positive Lyapunov exponents. We would like to relate  $\mathcal{Q}$  to the number of end states at zero excitation energy, and then chose a reference state such that this relationship takes a simple form. This is worked out in the next section, with the resulting expressions for  $\mathcal{Q}$  given in Table 2.1.

## 2.3 Number of end states from topological quantum number

We consider first the superconducting symmetry classes D and DIII and then the chiral symmetry classes BDI, AIII, and CII. The symmetry class D was treated in detail in Ref. 11 and is included here for completeness and for comparison with class DIII.

### 2.3.1 Superconducting symmetry classes

Electron-hole symmetry in a superconductor relates the energy - dependent creation and annihilation operators by  $\gamma^\dagger(E) = \gamma(-E)$ . Since therefore  $\gamma^\dagger = \gamma$  at  $E = 0$ , an excitation at zero energy is a Majorana fermion,

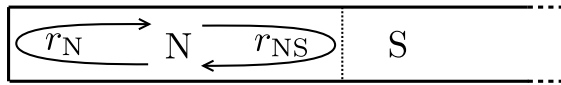


**Figure 2.1.** Superconducting wire (S) connected to a normal-metal lead (N) which is closed at one end. A bound state at the Fermi level can form at the NS interface, characterized by a unit eigenvalue of the product  $r_N r_{NS}$  of two matrices of reflection amplitudes (indicated schematically by arrows).

equal to its own antiparticle. The end states in symmetry classes D and DIII are so-called Majorana bound states [5]. In the open systems considered here, where the superconducting wire is connected to semi-infinite normal-metal leads, the end states are actually only quasi-bound states, but they still manifest themselves as a resonance in a conduction experiment [21, 22].

The topological quantum number in class D should give the parity of the number  $\mathcal{N}$  of Majorana bound states at one end of the wire:  $\mathcal{N}$  is even ( $Q = 1$ ) in the topologically trivial phase, while  $\mathcal{N}$  is odd ( $Q = -1$ ) in the topologically nontrivial phase. In class DIII all states are twofold Kramers degenerate so  $\mathcal{N}$  is to be replaced by  $\mathcal{N}/2$ .

Let us now verify that the determinant and Pfaffian expressions for the topological charge in Table 2.1 indeed give this bound state parity. We transform the quasi-bound states into true bound states by terminating the normal-metal lead at some distance far from the normal-superconductor (NS) interface (see Fig. 2.1). For the same purpose we assume that the superconducting wire is sufficiently long that transmission of quasiparticles from one end to the other can be neglected. The reflection matrix  $r_{NS}$  from the NS interface is then an  $N \times N$  unitary matrix. The number of modes  $N = 2M$  is even, because there is an equal number of electron and hole modes.

The condition for a bound state at the Fermi level is

$$\text{Det}(1 - r_N r_{NS}) = 0, \quad (2.3)$$

where  $r_N$  is the reflection matrix from the terminated normal-metal lead. In the electron-hole basis the matrix  $r_N$  has the block-diagonal form

$$r_N = \begin{pmatrix} U_N & 0 \\ 0 & U_N^* \end{pmatrix}. \quad (2.4)$$

The matrix  $U_N$  is an  $M \times M$  unitary matrix of electron reflection amplitudes. The corresponding matrix for hole reflections is  $U_N^*$  because of



particle-hole symmetry at the Fermi level.

The reflection matrix from the NS interface has also off-diagonal blocks,

$$r_{\text{NS}} = \begin{pmatrix} r_{ee} & r_{eh} \\ r_{he} & r_{hh} \end{pmatrix}. \quad (2.5)$$

Particle-hole symmetry relates the complex reflection matrices  $r_{he} = r_{eh}^*$  (from electron to hole and from hole to electron) and  $r_{ee} = r_{hh}^*$  (from electron to electron and from hole to hole).

### Class D

A unitary transformation,

$$r = \Omega r_{\text{NS}} \Omega^\dagger, \quad \Omega = \sqrt{\frac{1}{2}} \begin{pmatrix} 1 & 1 \\ -i & i \end{pmatrix}, \quad (2.6)$$

produces a real reflection matrix  $r = r^*$ . This is the so-called Majorana basis used for class D in Table 2.1. The determinant is unchanged by the change of basis,  $\text{Det } r_{\text{NS}} = \text{Det } r$ .

The condition (2.3) for a bound state reads, in terms of  $r$ ,

$$\text{Det}(1 + O_{\text{N}} r) = 0, \quad (2.7)$$

with  $O_{\text{N}} = -\Omega r_{\text{NS}} \Omega^\dagger$  an orthogonal matrix. The number  $\mathcal{N}$  of bound states is the number of eigenvalues  $-1$  of the  $2M \times 2M$  orthogonal matrix  $O_{\text{N}} r$ , while the other  $2M - \mathcal{N}$  eigenvalues are either equal to  $+1$  or come in conjugate pairs  $e^{\pm i\phi}$ . Hence  $\text{Det } O_{\text{N}} r = (-1)^{\mathcal{N}}$  and since  $\text{Det } O_{\text{N}} = 1$  we conclude that  $\text{Det } r = (-1)^{\mathcal{N}}$ , so indeed the determinant of the reflection matrix gives the bound state parity in class D.

### Class DIII

Time-reversal symmetry in class DIII requires

$$A_{\text{NS}} \equiv i \Sigma_y r_{\text{NS}} = -A_{\text{NS}}^{\text{T}}, \quad (2.8)$$

with  $\Sigma_y = \sigma_y \oplus \sigma_y \oplus \cdots \oplus \sigma_y$ . Instead of Eq. (2.6) we now define

$$r = \Omega A_{\text{NS}} \Omega^{\text{T}}. \quad (2.9)$$

(The matrix  $\Sigma_y$  acts on the spin degree of freedom, hence it commutes with  $\Omega$ , which acts on the electron-hole degree of freedom.) In this basis  $r = r^*$  is still real, as required by particle-hole symmetry, while the time-reversal symmetry requirement reads  $r = -r^T$ . This is the basis used for class DIII in Table 2.1.

The Pfaffians in the two bases are related by

$$\text{Pf } r = (\text{Det } \Omega)(\text{Pf } A_{\text{NS}}) = (-1)^{N/4} \text{Pf } A_{\text{NS}}.$$

Each electron and each hole mode has a twofold Kramers degeneracy, so the total number of modes  $N$  is an integer multiple of four. The relation can be written equivalently as

$$\text{Pf } ir = \text{Pf } A_{\text{NS}}. \quad (2.10)$$

This identity is at the origin of the factor  $i$  appearing in the class DIII expression for the topological quantum number in Table 2.1.

The condition (2.3) for a bound state can be rewritten as

$$\text{Det } (A_N - r) = [\text{Pf } (A_N - r)]^2 = 0, \quad (2.11)$$

where  $A_N \equiv \Omega(i\Sigma_y r_N^\dagger)\Omega^T$ , as well as  $r$ , are antisymmetric orthogonal matrices. In App. 2.6.1 we show that the multiplicity  $\mathcal{N}$  of the number of solutions to Eq. (2.11) satisfies

$$(-1)^{\mathcal{N}/2} = (\text{Pf } A_N)(\text{Pf } r). \quad (2.12)$$

Since, in view of Eq. (2.4),

$$\text{Pf } A_N = (\text{Det } \Omega)|\text{Pf } (i\Sigma_y U_N^\dagger)|^2 = (-1)^{N/4}, \quad (2.13)$$

we conclude that  $(-1)^{N/4} \text{Pf } r \equiv \text{Pf } ir$  gives the parity of the number  $\mathcal{N}/2$  of Kramers degenerate bound states. This is the topological quantum number for class DIII listed in Table 2.1.

### 2.3.2 Chiral symmetry classes

In the chiral symmetry classes BDI, AIII, and CII we wish to relate the number  $\nu(r)$  of negative eigenvalues of the reflection matrix  $r$  to the number of quasi-bound states at the end of the wire. As before, we transform these end states into true bound states by terminating the wire

and assume that the transmission probability through the wire is negligibly small (so  $r$  is unitary). While in the superconducting symmetry classes we could choose a normal metal lead as a unique termination, in the chiral classes there is more arbitrariness in the choice of the unitary reflection matrix  $r_0$  of the termination.

Since reflection matrices in the chiral classes are Hermitian (see Table 2.1), we can decompose

$$r_0 = U_0 \mathcal{S}_{n_0} U_0^\dagger, \quad \mathcal{S}_{n_0} = \begin{pmatrix} \mathbf{1}_{N-n_0} & 0 \\ 0 & -\mathbf{1}_{n_0} \end{pmatrix}, \quad (2.14)$$

where  $U_0$  is an  $N \times N$  unitary matrix,  $n_0 = \nu(r_0)$ , and  $\mathbf{1}_{n_0}$  is an  $n_0 \times n_0$  unit matrix. (Unitarity restricts the eigenvalues to  $\pm 1$ .) Similarly,

$$r = U_1 \mathcal{S}_{n_1} U_1^\dagger, \quad (2.15)$$

with  $\nu(r) = n_1$ .

Time-reversal symmetry with (without) spin-rotation symmetry restricts the unitary matrices  $U_0$  and  $U_1$  to the orthogonal (symplectic) subgroup, but to determine the number of bound states we only need the unitarity.

The condition  $\text{Det}(1 - r_0 r) = 0$  for a zero-energy bound state takes the form

$$\text{Det}(1 - \mathcal{S}_{n_0} U \mathcal{S}_{n_1} U^\dagger) = 0, \quad (2.16)$$

with  $U = U_0^\dagger U_1$ . We seek the minimal multiplicity  $\mathcal{N}$  of the solutions of this equation, for arbitrary  $U$ . (There may be more solutions for a special choice of  $U$ , but these do not play a role in the characterization of the topological phase.)

We divide  $U$  into four rectangular subblocks,

$$U = \begin{pmatrix} M_{N-n_0, N-n_1} & M_{N-n_0, n_1} \\ M_{n_0, N-n_1} & M_{n_0, n_1} \end{pmatrix}, \quad (2.17)$$

where  $M_{n,m}$  is a matrix of dimensions  $n \times m$ . Since

$$1 - \mathcal{S}_{n_0} U \mathcal{S}_{n_1} U^\dagger = 2 \begin{pmatrix} 0 & M_{N-n_0, n_1} \\ M_{n_0, N-n_1} & 0 \end{pmatrix} U^\dagger, \quad (2.18)$$

in view of unitarity of  $U$ , the bound state equation (2.16) simplifies to

$$\text{Det} \begin{pmatrix} 0 & M_{N-n_0, n_1} \\ M_{n_0, N-n_1} & 0 \end{pmatrix} = 0. \quad (2.19)$$

For any matrix  $M_{n,m}$  with  $n < m$  there exist at least  $m - n$  independent vectors  $v$  of rank  $m$  such that  $M_{n,m}v = 0$ . Therefore Eq. (2.19) has at least  $|n_0 + n_1 - N|$  independent solutions, hence

$$\mathcal{N} = |\nu(r) + \nu(r_0) - N|. \quad (2.20)$$

This is the required relation between the topological quantum number  $\mathcal{Q} = \nu(r)$  (in class BDI, AIII) or  $\mathcal{Q} = \frac{1}{2}\nu(r)$  (in class CII) and the minimal number of bound states  $\mathcal{N}$  at one end of the wire, for arbitrary termination of the wire. In the special case of termination by a reflection matrix  $r_0 = -\mathbf{1}_N \Rightarrow \nu(r_0) = N$ , the relation takes the simple form  $\mathcal{N} = \mathcal{Q}$  (in class BDI, AIII) and  $\mathcal{N} = 2\mathcal{Q}$  (in class CII).

So far we considered one of the two ends of the wire, with reflection matrix  $r$ . The other end has reflection matrix  $r' = -r$  [see Eq. (2.2)], so  $\nu(r') = N - \nu(r)$ . Termination of that end by a reflection matrix  $r'_0$  produces a minimal number  $\mathcal{N}'$  of bound states given by

$$\mathcal{N}' = |\nu(r) - \nu(r'_0)|. \quad (2.21)$$

For  $r'_0 = \mathbf{1}_N \Rightarrow \nu(r'_0) = 0$  we have the simple relation  $\mathcal{N}' = \mathcal{Q}$  (in class BDI, AIII) and  $\mathcal{N}' = 2\mathcal{Q}$  (in class CII). The (minimal) number of bound states at the two ends is then the same, but in general it may be different, depending on how the wire is terminated [23, 24]. This arbitrariness in the chiral symmetry classes is again in contrast to the superconducting classes, where Majorana bound states come in pairs at opposite ends of the wire.

## 2.4 Superconducting versus chiral symmetry classes

As a first application of our general considerations, we contrast the effect of disorder and intermode scattering on topological phase transitions in the superconducting and chiral symmetry classes. We focus on the symmetry classes D and BDI, which in the single-mode case are identical, so that the effect of intermode scattering is most apparent.

In both these classes there is particle-hole symmetry, which implies that we can choose a basis such that the Hermitian Hamiltonian  $H$  satisfies

$$H^* = -H. \quad (2.22)$$

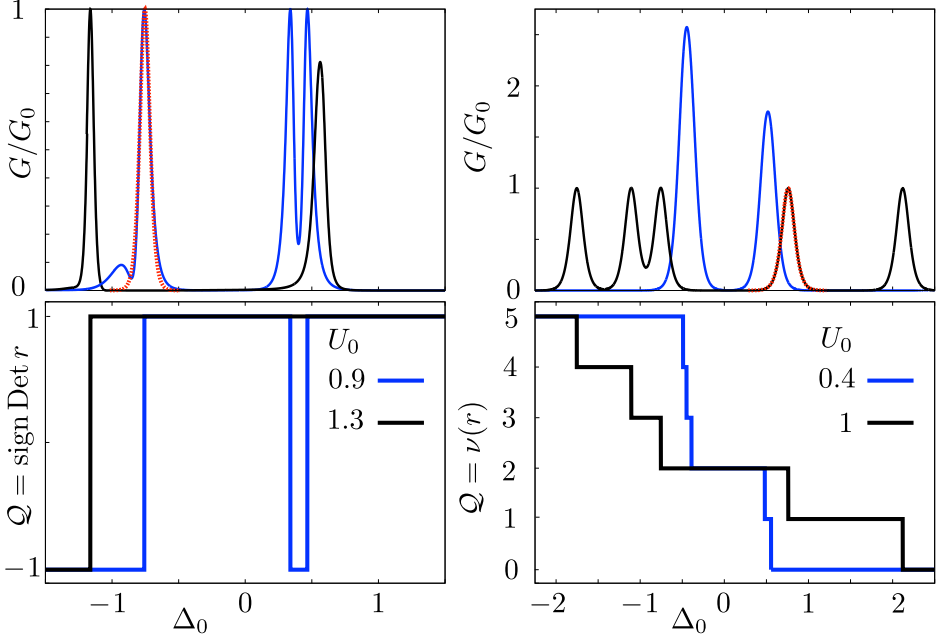


**Figure 2.2.** Conductance  $G$  (top panels) and topological quantum number  $Q$  (bottom panels) in the superconducting class D (left panels) and the chiral class BDI (right panels). The black and blue curves are calculated from the Hamiltonian (2.23), for a single disorder realization in a wire with  $N = 5$  modes. The red dotted curve show the universal line shape (2.28) of an isolated conductance peak. Energies  $\Delta_0$  and  $U_0$  are measured in units of  $\hbar v_F / \delta L$  for  $\delta L = L/10$ .

We assume for simplicity that the  $N$  right-moving and left-moving modes all have the same Fermi velocity  $v_F$ . To first order in momentum  $p = -i\hbar\partial/\partial x$  the Hamiltonian then takes the form

$$H = v_F p \mathbf{1}_N \otimes \sigma_z + \Delta_0 \mathbf{1}_N \otimes \sigma_y + U_0 [iA(x) \otimes \sigma_z + iB(x) \otimes \sigma_x + C(x) \otimes \sigma_y], \quad (2.23)$$

with  $\mathbf{1}_N$  the  $N \times N$  unit matrix. The  $N \times N$  matrices  $A$  and  $B$  are real antisymmetric, while  $C$  is real symmetric. (For  $N = 1$  this model Hamiltonian was used in Ref. 11.)

The Hamiltonian (2.23) respects all the symmetries present in class D, but in class BDI the additional chiral symmetry requires

$$\sigma_x H \sigma_x = -H. \quad (2.24)$$

This implies that the matrix  $B \equiv 0$  in class BDI.

The transfer matrix  $\mathcal{M}$  relates the wave function  $\Psi(x)$  at the two ends of the disordered wire (of length  $L$ ):  $\Psi(L) = \mathcal{M}\Psi(0)$ . At the Fermi level (zero energy)  $\mathcal{M}$  follows upon integration of the wave equation  $H\Psi = 0$  from  $x = 0$  to  $x = L$ ,

$$\mathcal{M} = \mathcal{T} \exp \left\{ \frac{1}{\hbar v_F} \int_0^L dx \left( -\Delta_0 \mathbb{1}_N \otimes \sigma_x + U_0 [A(x) \otimes \sigma_0 + iB(x) \otimes \sigma_y - C(x) \otimes \sigma_x] \right) \right\}. \quad (2.25)$$

The symbol  $\mathcal{T}$  indicates the ordering of the noncommuting matrices in order of decreasing  $x$ .

The Pauli matrices in Eq. (2.25) define a  $2 \times 2$  block structure for the  $2N \times 2N$  transfer matrix. The  $N \times N$  reflection matrix  $r$  and transmission matrix  $t$  follow from this block structure by solving

$$\begin{pmatrix} t \\ 0 \end{pmatrix} = \mathcal{M} \begin{pmatrix} 1 \\ r \end{pmatrix}. \quad (2.26)$$

The reflection matrix gives the topological quantum number,  $\mathcal{Q} = \text{sign Det } r$  in class D and  $\mathcal{Q} = \nu(r)$  in class BDI. The transmission matrix gives the conductance

$$G = G_0 \text{Tr } tt^\dagger. \quad (2.27)$$

In class D this is a thermal conductance (with  $G_0 = \pi^2 k_B^2 \tau_0 / 6h$ , at temperature  $\tau_0$ ), while in class BDI this is an electrical conductance (with  $G_0 = 2e^2/h$ ).

We model a disordered wire in class D by taking a Gaussian distribution (zero average, unit variance) of the independent matrix elements of  $A(x), B(x), C(x)$ , piecewise constant over a series of segments of length  $\delta L \ll L$ . In class BDI we use the same model with  $B \equiv 0$ .

In Fig. 2.2 we plot the conductance and topological quantum number as a function of  $\Delta_0$  for different values of  $U_0$ , calculated in class D and BDI for a single realization of the disorder. A change in  $\mathcal{Q}$  is accompanied by a peak in  $G$ , quantized at  $G_0$  if the topological phase transitions are well separated [11]. The difference between the  $\mathbb{Z}_2$  superconducting topological phase and the  $\mathbb{Z}$  chiral topological phase becomes evident when conductance peaks merge: In the superconducting class D the

conductance peaks annihilate, while in the chiral class BDI a maximum of  $N$  conductance peaks can reinforce each other.

Also shown in Fig. 2.2 is that a single isolated conductance peak at  $\Delta_0 = \Delta_c$  has the same line shape as a function of  $\delta = (\Delta_0 - \Delta_c)/\Gamma$ ,

$$G_{\text{peak}}(\delta) = \frac{G_0}{\cosh^2 \delta}, \quad (2.28)$$

in both the superconducting and chiral symmetry classes. (The width  $\Gamma$  of the peak is not universal.) We have checked that the line shape in the other three symmetry classes also has the same form (2.28), so this is a general statement. One cannot, therefore, distinguish the  $\mathbb{Z}_2$  and  $\mathbb{Z}$  topological phases by studying a single phase transition. This is a manifestation of the super-universality of Gruzberg, Read, and Vishveshwara [19].

## 2.5 Application to dimerized polymer chains

We conclude with an application in a physical system. Such an application was given for the superconducting symmetry class D in Ref. 11, so here we concentrate on the chiral classes. We consider a dimerized polymer chain such as polyacetylene, with alternating long and short bonds, described by the Su-Schrieffer-Heeger Hamiltonian [25]. This is a tight-binding Hamiltonian, which in the continuum limit takes the form of the class BDI Hamiltonian (2.23) [26]. Our goal is to obtain the  $\mathbb{Z}$  topological quantum number of  $N$  coupled polymer chains from the reflection matrix.

The single-chain electronic Hamiltonian is [25–27]

$$H = - \sum_{n=1}^{N_L} t_{n+1,n} (c_{n+1}^\dagger c_n + c_n^\dagger c_{n+1}), \quad (2.29a)$$

$$t_{n+1,n} = t_0 - \alpha(u_{n+1} - u_n), \quad (2.29b)$$

with  $t_0$  and  $\alpha$  nearest-neighbor (real) hopping constants and  $c_n$  the electron annihilation operator at site  $n$ . (The spin degree of freedom plays no role and is omitted.) Chiral (or sublattice) symmetry means that  $H \mapsto -H$  if  $c_n \mapsto -c_n$  on all even-numbered or on all odd-numbered sites. We take  $N_L$  even, so that the chain contains an equal number of sites on each sublattice.

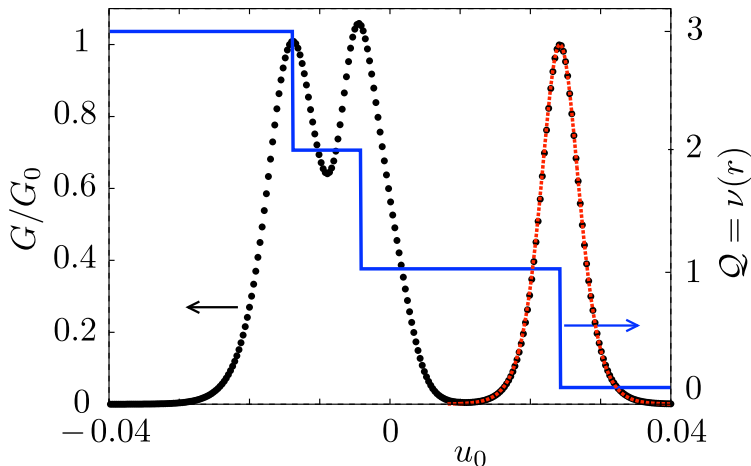


**Figure 2.3.** Conductance (black dotted line, left axis) and topological quantum number (blue solid line, right axis) of  $N = 3$  coupled polymer chains (each containing  $N_L = 300$  sites). These curves are calculated from the reflection and transmission matrices, obtained from the Hamiltonian (2.29) for  $t_0 = 1$ ,  $\alpha = 1$ , and  $t_{\text{inter}} = 0.1$ , for a single realization of the random  $\delta u_n$ 's (having a Gaussian distribution with zero average and standard deviation 0.2). The red dotted curve shows the universal line shape (2.28) of an isolated conductance peak.

Following Jackiw and Semenoff [26] we ignore the atomic dynamics, assuming that the electrons hop in a prescribed atomic displacement field of the dimerized form  $u_n = (-1)^n u_0 + \delta u_n$ . Disorder is accounted for by random displacements  $\delta u_n$ , chosen independently on  $N$  parallel chains. Nearest neighbors on adjacent chains are coupled by an inter-chain hopping constant  $t_{\text{inter}}$ , which we take non-fluctuating for simplicity.

The reflection and transmission matrices  $r$  and  $t$  were computed from the Hamiltonian (2.29) via the transfer matrix, as outlined in App. 2.6.2. In Fig. 2.3 we show the topological quantum number  $\mathcal{Q}$  (equal to the number  $\nu(r)$  of negative eigenvalues of the Hermitian reflection matrix  $r$ ), as well as the electrical conductance  $G = G_0 \text{Tr} tt^\dagger$  (with  $G_0 = 2e^2/h$ ). These two quantities are plotted as a function of the dimerization parameter  $u_0$ , to illustrate the topological phase transition, but unlike the excitation gap  $\Delta_0$  in a superconducting wire this is not an externally controllable parameter.



The case  $N = 3$  plotted in Fig. 2.3 is a  $\mathbb{Z}$  topological phase, and each change in the topological quantum number is accompanied by a peak of quantized conductance. The lineshape again has the universal form (2.28).

## 2.6 Appendix

### 2.6.1 Calculation of the number of end states in class DIII

We wish to prove that the multiplicity  $\mathcal{N}$  of the number of solutions of the bound state equation (2.11) satisfies Eq. (2.12), for arbitrary antisymmetric orthogonal matrices  $A_N$  and  $r$  of dimension  $N \times N$ , with  $N = 2M$  and  $M$  an even integer.

We use that any antisymmetric orthogonal matrix can be factorized as  $A_N = O_N i\Sigma_y O_N^T$ ,  $r = O_{NS} i\Sigma_y O_{NS}^T$ , in terms of orthogonal matrices  $O_N$  and  $O_{NS}$ . These factorizations relate a Pfaffian to a determinant,  $\text{Pf } A_N = \text{Det } O_N$ ,  $\text{Pf } r = \text{Det } O_{NS}$ .

We seek the multiplicity  $\mathcal{N}$  of the number of solutions of

$$[\text{Pf}(A_N - r)]^2 = 0 \Leftrightarrow [\text{Pf}(i\Sigma_y - Oi\Sigma_y O^T)]^2 = 0, \quad (2.30)$$

with  $O = O_N^T O_{NS}$  an orthogonal matrix.

We consider the secular equation for the twofold degenerate eigenvalues  $z_n$  of the matrix  $i\Sigma_y Oi\Sigma_y O^T$ ,

$$\begin{aligned} 0 &= \text{Det}(z - i\Sigma_y Oi\Sigma_y O^T) = \text{Det}(zi\Sigma_y + Oi\Sigma_y O^T) \\ &= [\text{Pf}(zi\Sigma_y + Oi\Sigma_y O^T)]^2 = \left[ \prod_{n=1}^M (z - z_n) \right]^2 \Leftrightarrow \\ 0 &= \text{Pf}(zi\Sigma_y + Oi\Sigma_y O^T) = c \prod_{n=1}^M (z - z_n) = 0. \end{aligned} \quad (2.31)$$

The value  $c = 1$  of the prefactor follows by sending  $z$  to infinity. By filling in  $z = 0$  we find that

$$\text{Pf}(Oi\Sigma_y O^T) = \text{Det } O = \prod_{n=1}^M z_n. \quad (2.32)$$

The  $\mathcal{N}/2$  bound state solutions have  $z_n = -1$ , the remaining  $M - \mathcal{N}/2$  solutions have either  $z_n = 1$  or conjugate pairs  $z_n = e^{\pm i\phi}$ . Hence

$$\prod_{n=1}^M z_n = (-1)^{\mathcal{N}/2} = \text{Det } O = (\text{Pf } A_N)(\text{Pf } r), \quad (2.33)$$

as we set out to prove.

## 2.6.2 Computing the topological quantum number of a dimerized polymer chain

To simplify the notation we outline the calculation of the topological quantum number for the case  $N = 1$  of a single polymer chain, when the transmission matrix  $r$  is a scalar and we may take  $\mathcal{Q} = \frac{1}{2}(1 - \mathcal{Q}')$  with  $\mathcal{Q}' = \text{sign } r \in \{-1, 1\}$ . (The multi-chain case, with  $\mathcal{Q} = \nu(r) \in \{0, 1, 2, \dots, N\}$ , is analogous.)

From the tight-binding Hamiltonian (2.29) we directly read off the zero-energy transfer matrix  $\tilde{\mathcal{M}}$  in the site basis,

$$\begin{pmatrix} t_{n+1,n}\psi_n \\ \psi_{n+1} \end{pmatrix} = \tilde{\mathcal{M}}_n \begin{pmatrix} t_{n,n-1}\psi_{n-1} \\ \psi_n \end{pmatrix}, \quad (2.34)$$

$$\tilde{\mathcal{M}}_n = \begin{pmatrix} 0 & t_{n+1,n} \\ -1/t_{n+1,n} & 0 \end{pmatrix}. \quad (2.35)$$

The normalization factors in Eq. (2.34) have been inserted so that the current operator has the site-independent form  $\mathcal{I} = \sigma_y$ .

To obtain the scattering matrix we need to transform from the site basis to a basis of left-movers and right-movers, in which the current operator equals  $\sigma_z$  rather than  $\sigma_y$ . This change of basis is realized by the matrix  $\Omega$  from Eq. (2.6),

$$\Omega^T \sigma_y \Omega^* = \sigma_z. \quad (2.36)$$

Multiplying the transfer matrices we find for the entire chain (containing an even number of sites  $N_L$ ):

$$\tilde{\mathcal{M}} = \tilde{\mathcal{M}}_{N_L} \tilde{\mathcal{M}}_{N_L-1} \cdots \tilde{\mathcal{M}}_2 \tilde{\mathcal{M}}_1 = \begin{pmatrix} X & 0 \\ 0 & 1/X \end{pmatrix}, \quad (2.37)$$

$$\mathcal{M} = \Omega^T \tilde{\mathcal{M}} \Omega^* = \frac{1}{2X} \begin{pmatrix} X^2 + 1 & X^2 - 1 \\ X^2 - 1 & X^2 + 1 \end{pmatrix}, \quad (2.38)$$

with the definition

$$X = (-1)^{N_L/2} \prod_{n=1}^{N_L/2} \frac{t_{2n+1,2n}}{t_{2n,2n-1}}. \quad (2.39)$$

We obtain the reflection and transmission amplitudes from  $\mathcal{M}$  with the help of Eq. (2.26). The result is

$$r = \frac{1 - X^2}{1 + X^2}, \quad t = \frac{2X}{1 + X^2}, \quad (2.40)$$

so the topological quantum number is given by

$$\begin{aligned} \mathcal{Q}' &= \text{sign}(1 - X^2) \\ &= \text{sign} \left( \prod_{n=1}^{N_L/2} t_{2n,2n-1}^2 - \prod_{n=1}^{N_L/2} t_{2n+1,2n}^2 \right). \end{aligned} \quad (2.41)$$

If all hopping constants are close to  $t_0 > 0$  we may simplify this expression to

$$\mathcal{Q}' = \text{sign} \left( \sum_{n=1}^{N_L/2} [t_{2n,2n-1} - t_{2n+1,2n}] \right). \quad (2.42)$$

In the absence of disorder, when  $t_{2n,2n-1} = t_0 - 2\alpha u_0$ ,  $t_{2n+1,2n} = t_0 + 2\alpha u_0$ , this reduces further to  $\mathcal{Q}' = -\text{sign} \alpha u_0$ , so we recover the original criterion that the dimerized polymer chain has bound states at the ends if the weaker bond is at the end [25].



# Bibliography

- [1] B. I. Halperin, Phys. Rev. B **25**, 2185 (1982).
- [2] M. Büttiker, Phys. Rev. B **38**, 9375 (1988).
- [3] D. J. Thouless, M. Kohmoto, M. P. Nightingale and M. den Nijs, Phys. Rev. Lett. **49**, 405 (1982).
- [4] R. Jackiw and J. R. Schrieffer, Nucl. Phys. B **190**, 253 (1981).
- [5] A. Yu. Kitaev, Phys. Usp. **44** (suppl.), 131 (2001).
- [6] X.-L. Qi, T. L. Hughes, and S.-C. Zhang, Phys. Rev. B **81**, 134508 (2010).
- [7] B. Béri, Phys. Rev. B **81**, 134515 (2010).
- [8] P. Ghosh, J. D. Sau, S. Tewari, and S. Das Sarma, Phys. Rev. B **82**, 184525 (2010).
- [9] A. P. Schnyder and S. Ryu, Phys. Rev. B **84**, 060504(R) (2011).
- [10] T. A. Loring and M. B. Hastings, Europhys. Lett. **92**, 67004 (2010);  
M. B. Hastings and T. A. Loring, Ann. Phys. **326** 1699 (2011).
- [11] A. R. Akhmerov, J. P. Dahlhaus, F. Hassler, M. Wimmer, and C. W. J. Beenakker, Phys. Rev. Lett. **106**, 057001 (2011).
- [12] M. Z. Hasan and C. L. Kane, Rev. Mod. Phys. **82**, 3045 (2010).
- [13] X.-L. Qi and S.-C. Zhang, Rev. Mod. Phys. **83**, 1057 (2011).
- [14] S. Ryu, A. P. Schnyder, A. Furusaki, and A. W. W. Ludwig, New J. Phys. **12**, 065010 (2010).

- [15] A. Altland and M. R. Zirnbauer, *Phys. Rev. B* **55**, 1142 (1997).
- [16] P. W. Brouwer, C. Mudry, B. D. Simons, and A. Altland, *Phys. Rev. Lett.* **81**, 862 (1998); P. W. Brouwer, A. Furusaki, and C. Mudry, *Phys. Rev. B* **67**, 014530 (2003).
- [17] O. Motrunich, K. Damle, and D. A. Huse, *Phys. Rev. B* **63**, 224204 (2001).
- [18] F. Merz and J. T. Chalker, *Phys. Rev. B* **65**, 054425 (2002).
- [19] I. A. Gruzberg, N. Read, and S. Vishveshwara, *Phys. Rev. B* **71**, 245124 (2005).
- [20] In Eq. (2.2) we assumed  $\text{Tr } S = 0$  for the three chiral symmetry classes (BDI, AIII, CII), which means that there is no imbalance between the number of degrees of freedom of opposite chirality (equal number of sites on each sublattice in the case of a bipartite lattice). More generally,  $S$  has  $N + p$  eigenvalues equal to  $+1$  and  $N - p$  eigenvalues equal to  $-1$ , so  $\text{Tr } S = 2p$  (with  $p \in \{-N, \dots, -1, 0, 1, \dots, N\}$ ). The reflection matrices  $r$  and  $r'$  then each have  $|p|$  fully reflected modes, and the polar decomposition (2.2) applies to the remaining  $N - |p|$  modes.
- [21] K. T. Law, P. A. Lee, and T. K. Ng, *Phys. Rev. Lett.* **103**, 237001 (2009).
- [22] M. Wimmer, A. R. Akhmerov, J. P. Dahlhaus, and C. W. J. Beenakker, *New J. Phys.* **13**, 053016 (2011).
- [23] P. W. Brouwer, E. Racine, A. Furusaki, Y. Hatsugai, Y. Morita, and C. Mudry, *Phys. Rev. B* **66**, 014204 (2002).
- [24] The equality  $\nu(r) + \nu(r') = N$  holds for  $\text{Tr } S = 0$ , so for balanced chiralities. More generally, for  $\text{Tr } S = 2p$  one has  $\nu(r) + \nu(r') = N - p$ . If the wire is terminated by reflection matrices  $r_0 = -\mathbf{1}_N$ ,  $r'_0 = \mathbf{1}_N$ , the number of end states at the two ends differs by  $p$ .
- [25] W. P. Su, J. R. Schrieffer, and A. J. Heeger, *Phys. Rev. Lett.* **42**, 1698 (1979); *Phys. Rev. B* **22**, 2099 (1980).
- [26] R. Jackiw and G. Semenoff, *Phys. Rev. Lett.* **50**, 439 (1983).
- [27] M. Rice and G. Mele, *Phys. Rev. Lett.* **49**, 1455 (1982).

# Chapter 3

## Scattering theory of topological insulators and superconductors

### 3.1 Introduction

Given a Hamiltonian  $H(\mathbf{k})$  of a band insulator or a superconductor and its symmetries as a function of the momentum  $\mathbf{k}$  in  $d$ -spatial dimensions, a topological invariant  $\mathcal{Q}(H)$  can be defined. It counts the number of surface states insensitive to disorder which are present at an interface between the system and the vacuum. In each spatial dimension exactly 5 out of 10 Altland-Zirnbauer symmetry classes (distinguished by time-reversal symmetry  $\mathcal{T}$ , particle-hole symmetry  $\mathcal{P}$ , and chiral/sub-lattice symmetry  $\mathcal{C}$ ) [1] allow for a nontrivial topological invariant [2, 3].

The evaluation of the topological invariant conventionally involves an integral over a  $d$ -dimensional Brillouin zone of some function of the Hamiltonian. Recently, various approximations to the topological invariant have been developed which require only the knowledge of eigenvalues and eigenvectors of the Hamiltonian at one point in momentum space (rather than in the entire Brillouin zone) [4–6].

Despite the fact that these approximations are more efficient, we argue that they do not use one important property of a topological invariant. By definition, the topological invariant describes the properties of the system at the Fermi level, namely the number of edge states. This observation suggests that it should be possible to calculate the topologi-

cal invariant without knowing the full spectrum of the Hamiltonian, but rather calculating only properties of the system at its Fermi energy. For one-dimensional (1D) systems, this was demonstrated in Ref. 7. Here, we show that *for any dimensionality* the topological invariant can be obtained from the scattering matrix of the system at the Fermi level.

Our results offer two benefits. Firstly, since the scattering matrix contains less degrees of freedom than the Hamiltonian, the computation of the topological invariant is much more efficient. Secondly, the scattering matrix relates the topological invariant to transport properties, suggesting ways to probe the topological phase by electrical or thermal conduction measurements [8, 9].

The approach is based on dimensional reduction: We relate the scattering matrix in  $d$  dimensions to a Hamiltonian in  $d - 1$  dimensions. Our scheme of dimensional reduction does not preserve the symmetry, unlike the field theory based scheme of Ref. 10. Instead our dimensional reduction preserves the topological invariant, similarly to the dimensional reduction of clean Dirac-like Hamiltonians of Ref. 11.

In the remainder of the introduction we first illustrate our approach by revisiting the familiar example of the integer quantum Hall effect. Subsequently, we present a brief outline of the paper.

### 3.1.1 Dimensional reduction in the quantum Hall effect

A 2D system exhibiting the integer quantum Hall effect is a topological insulator in the symmetry class A (all symmetries broken). It is characterized by a quantized transverse conductance  $\sigma_{xy} = ng_0$  with  $n \in \mathbb{Z}$  and  $g_0 = e^2/h$ . The quantum number  $n$  is a topological invariant (the so-called Chern number) of the Hamiltonian [12]. It equals the number of protected chiral edge states at the Fermi level, each of which contributes  $e^2/h$  to the transverse conductance [13, 14].

Charge pumping provides an alternative way to relate the topological invariant to a quantized transport property: inserting a flux quantum inside a quantum Hall sample rolled-up to a cylinder adiabatically pumps  $n$  electrons across the sample [15]. There exists a scattering matrix formulation of charge pumping [16, 17], which allows to express pumped charge per cycle (in units of  $e$ ),

$$Q = \frac{1}{2\pi i} \int_0^{2\pi} d\varphi \frac{d}{d\varphi} \log \det r(\varphi), \quad (3.1)$$



through the flux dependence of the reflection block  $r(\varphi)$  of the scattering matrix of one lead [18]. Here  $\varphi$  denotes the dimensionless flux  $\Phi = \hbar\varphi/e$  and the system is assumed to be insulating such that the reflection matrix  $r(\varphi)$  is unitary. Equation (3.1) is nothing but the winding number of  $\det r(\varphi)$  when  $\varphi$  is varied from 0 to  $2\pi$ , which is a topological invariant.

The winding number occurs in a different context in the theory of topological insulators. The topological invariant of a one-dimensional Hamiltonian  $H(k)$  with chiral/sub-lattice symmetry

$$H(k) = \begin{pmatrix} 0 & h(k) \\ h^\dagger(k) & 0 \end{pmatrix}, \quad (3.2)$$

is expressed via the winding number given by [19, 20]

$$\mathcal{Q}(H) = \frac{1}{2\pi i} \int_0^{2\pi} dk \frac{d}{dk} \log \det h(k). \quad (3.3)$$

Here momentum  $k$  is measured in units of  $\hbar/a$ , with  $a$  the lattice constant. We see that upon the identification  $h \equiv r$  and  $k \equiv \varphi$  we are able to express the topological invariant in a 2D system without any symmetries as the topological invariant of an effective Hamiltonian in 1D with chiral symmetry. We will show that a similar dimensional reduction applies to all topological invariants in all dimensions.

### 3.1.2 Outline of the paper

As a prerequisite for the dimensional reduction, we have to open up the system to obtain a scattering matrix from a given Hamiltonian. Section 3.2 explains how this can be done. This section may be skipped on first reading. The dimensional reduction proceeds along the following lines: First we form out of a scattering matrix  $S$  a reflection block  $r(\mathbf{k})$  from one surface of the system, when all the dimensions except one are closed by twisted periodic boundary conditions. Then, the effective Hamiltonian  $H_{d-1}(\mathbf{k})$  in one dimension lower is defined according to the simple rule

$$H_{d-1}(\mathbf{k}) \equiv r(\mathbf{k}), \quad \text{with chiral symmetry}, \quad (3.4a)$$

$$H_{d-1}(\mathbf{k}) \equiv \begin{pmatrix} 0 & r(\mathbf{k}) \\ r^\dagger(\mathbf{k}) & 0 \end{pmatrix}, \quad \text{without chiral symmetry}. \quad (3.4b)$$

In Sec. 3.3 we show how to evaluate  $r(\mathbf{k})$  given the scattering matrix  $S$  of the initial system and prove that the reduced Hamiltonian  $H_{d-1}$  has the same topological invariant as the original  $H$ , i.e.  $\mathcal{Q}(H_{d-1}) = \mathcal{Q}(H)$ .

After the general proof we turn to the particular ways to evaluate the topological invariant in 1–3 dimensions in Sec. 3.4. In 1D we show that our expressions coincide with the ones derived in Ref. 7 in a different way, without using dimensional reduction. For 2D we formulate the evaluation of the topological invariant as a generalized eigenvalue problem. For 3D topological insulators in class AII the topological invariant reduces to a product of 2D invariants, while the other symmetry classes require usage of a Bott index [6]. We also mention how weak topological invariants fit into our approach.

We consider the numerical efficiency of our method and show examples of its application in Sec. 3.5. We also compare the finite size effects of different approximations to the topological invariant, and introduce the ‘fingerprint’ of phase transitions between different topological phases in 2D. Finally, we conclude in Sec. 3.6.

## 3.2 Scattering matrix from a Hamiltonian

This section contains the necessary preliminaries: the definition of scattering matrix and a proof that the shape of the Fermi surface can be calculated from the scattering matrix.

While the formulas in this section are needed for the actual implementation of our method of dimensional reduction, the method itself can be understood without them. This section can thus be skipped at first reading.

Any Hamiltonian  $H(\mathbf{k})$  of a translationally invariant system with a finite range hopping can be brought to the tight-binding form by choosing a sufficiently large unit cell

$$H(\mathbf{k}) = H + \sum_{i=0}^d t_i e^{ik_i} + \sum_{i=0}^d t_i^\dagger e^{-ik_i}. \quad (3.5)$$

Here  $\mathbf{k}$  is a  $d$ -dimensional vector of Bloch momenta,  $H$  is the on-site Hamiltonian, and  $t_i$  are the hoppings in positive  $i$ -direction. We start our consideration from opening the system and attaching  $2d$  fictitious leads to it. First we attach  $d$  sites to the original system without on-site

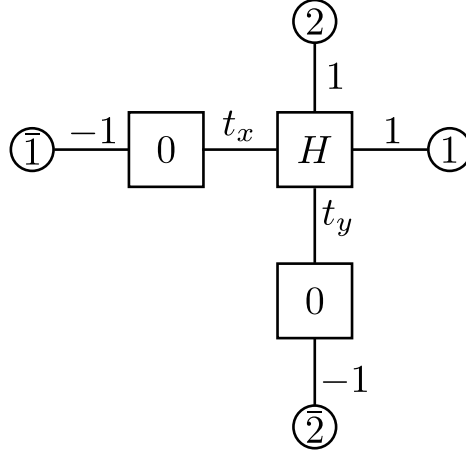


**Figure 3.1.** Sketch of the tight binding model used to attach leads in order to open-up the Hamiltonian  $H(k)$  of (3.5). In 2D we introduce four leads shown as circles labeled by  $1$ ,  $\bar{1}$ ,  $2$ , and  $\bar{2}$ . The on-site terms (boxes) are connected by hoppings (lines). The additional trivial hoppings  $1$  and  $-1$  are introduced such that the lead properties drop out when twisted periodic boundary conditions are applied. For the Mahaux-Weidenmüller formula (3.8), the three nodes form the on-site Hamiltonian  $\tilde{H}$  which is then connected via the trivial hoppings to ideal leads.

Hamiltonian, and connect them with hoppings  $t_i$  to the system. The Hamiltonian of this ‘unfolded’ system becomes

$$\tilde{H} = \begin{pmatrix} H & t^\dagger \\ t & 0 \end{pmatrix}, \quad (3.6)$$

$$t = (t_1, t_2, \dots, t_d)^T. \quad (3.7)$$

In the next step we attach the fictitious leads to the unfolded system, as illustrated in Fig. 3.1 for the case of two dimensions. The hopping to the leads in positive  $i$ -direction is chosen to be equal to  $+1$ , and in the negative  $i$ -direction to be equal to  $-1$ .

We are now ready to construct the scattering matrix of the open system by using the Mahaux-Weidenmüller formula [21] (see also Appendix 3.7.1)

$$S = 1 + 2\pi i W^\dagger (\tilde{H} - i\pi W W^\dagger)^{-1} W. \quad (3.8)$$

The coupling  $W$  between the lead and the system is equal to  $w\sqrt{\rho}$ , with  $w$  the hopping from the lead to the system, and  $\rho$  the density of states

in the lead. We choose  $\rho = 1/w\pi$ , such that

$$W = \frac{1}{\sqrt{\pi}} \begin{pmatrix} 1 & 0 & 1 & 0 & \cdots & 1 & 0 \\ 0 & -1 & 0 & 0 & & 0 & 0 \\ 0 & 0 & 0 & -1 & & 0 & 0 \\ \vdots & & & & \ddots & & \vdots \\ 0 & 0 & 0 & 0 & \cdots & 0 & -1 \end{pmatrix}; \quad (3.9)$$

here, we have set  $w = 1$  for convenience. The values of hopping and the lead density of states are chosen such that in the process of rolling-up, the fictitious leads drop out.

The scattering matrix (3.8) relates the incoming states in the leads to the outgoing ones:

$$\begin{pmatrix} \psi_1 \\ \psi_{\bar{1}} \\ \psi_2 \\ \psi_{\bar{2}} \\ \vdots \\ \psi_d \\ \psi_{\bar{d}} \end{pmatrix}_{\text{out}} = S \begin{pmatrix} \psi_1 \\ \psi_{\bar{1}} \\ \psi_2 \\ \psi_{\bar{2}} \\ \vdots \\ \psi_d \\ \psi_{\bar{d}} \end{pmatrix}_{\text{in}}. \quad (3.10)$$

To prove that the scattering matrix contains all of the information about the Fermi level at energy  $E_F = 0$ , we impose twisted periodic boundary conditions on the scattering states:

$$\begin{pmatrix} \psi_1 \\ \psi_{\bar{1}} \\ \psi_2 \\ \psi_{\bar{2}} \\ \vdots \\ \psi_d \\ \psi_{\bar{d}} \end{pmatrix}_{\text{in}} = Z(\mathbf{k}) \begin{pmatrix} \psi_1 \\ \psi_{\bar{1}} \\ \psi_2 \\ \psi_{\bar{2}} \\ \vdots \\ \psi_d \\ \psi_{\bar{d}} \end{pmatrix}_{\text{out}}, \quad (3.11)$$

with the twist matrix  $Z(\mathbf{k})$  given by

$$Z(\mathbf{k}) \equiv \begin{pmatrix} 0 & e^{ik_1} & 0 & \cdots & 0 \\ e^{-ik_1} & 0 & & & \vdots \\ 0 & & \ddots & & 0 \\ \vdots & & & 0 & e^{ik_d} \\ 0 & \cdots & 0 & e^{-ik_d} & 0 \end{pmatrix}. \quad (3.12)$$

We show that Eqs. (3.10) and (3.11) have a solution for a given  $k$  if and only if the equation  $H(\mathbf{k})\psi = 0$  has a nontrivial solution. The condition for the nontrivial solution of Eqs. (3.10) and (3.11) to exist is

$$\det[S - Z(\mathbf{k})] = 0. \quad (3.13)$$

Performing block-wise inversion of  $\tilde{H} - i\pi WW^\dagger$  yields

$$S = 1 + 2iW^\dagger \begin{pmatrix} J & -iJt^\dagger \\ -itJ & i - tJt^\dagger \end{pmatrix} W, \quad (3.14)$$

$$J = (H_0 - id - it^\dagger t)^{-1}. \quad (3.15)$$

We simplify this expression further by noting that

$$S = \gamma_z + 2i\gamma_z U^\dagger J U, \quad U = (1 \quad -it^\dagger) W, \quad (3.16)$$

with  $\gamma_z$  the third Pauli matrix in the direction space. We now write

$$\begin{aligned} \det[S - Z(\mathbf{k})] &= \det \left[ 1 + \gamma_z Z(\mathbf{k}) + 2iU^\dagger J U \right] \quad (3.17) \\ &= \det J \det[1 + \gamma_z Z(\mathbf{k})] \\ &\quad \times \det \left( J^{-1} + 2iU[1 + \gamma_z Z(\mathbf{k})]U^\dagger \right) \\ &= \det J \det[1 + \gamma_z Z(\mathbf{k})] \det H(\mathbf{k}). \end{aligned}$$

Since both  $J$  and  $1 + \gamma_z Z(\mathbf{k})$  are nonsingular, the last identity means that  $\det[S - Z(\mathbf{k})]$  and  $\det H(\mathbf{k})$  can only be zero simultaneously, which is what we set out to prove.

This proof shows that the Fermi surfaces as defined by the original Hamiltonian and the scattering matrix are identical. This is the reason why it is at all possible to determine the topological invariant using solely the scattering matrix  $S$ . Even though the scattering matrix only describes scattering at the Fermi level, it contains information about the complete Brillouin zone, and thus cannot be obtained from a long wavelength or low energy expansion of the Hamiltonian, but requires the complete Hamiltonian. Note however that the scattering matrix at a single energy contains less information about the system than the Hamiltonian: in order to determine the Hamiltonian from the scattering matrix, the inverse scattering problem has to be solved which requires knowledge of the scattering matrix at all the energies.

The size of the scattering matrix (3.8) is  $2d$ -times larger than the size of Hamiltonian. However, if the Hamiltonian is local on a large  $d$ -dimensional lattice with size  $L^d$ , the hoppings  $t_i$  are very sparse. This allows to efficiently eliminate all of the modes except the ones that are coupled to the hoppings. The resulting scattering matrix is of size  $2dL^{d-1}$ , and accordingly for large systems it is a dense matrix of much smaller dimensions than the Hamiltonian.

### 3.3 Dimensional reduction

The aim of this section is to provide a route to the topological classification of scattering matrices by elimination of one spatial dimensions. This approach of dimensional reduction is inspired by the transport properties of topological systems. When applied to 1D systems it reproduces the results of Ref. 7, and in quantum Hall systems it reproduces the relation between adiabatic pumping and the Chern number of Refs. 15, 18.

We begin from substituting the first  $2(d-1)$  equations from (3.11) into (3.10). This is equivalent to applying twisted periodic boundary conditions to all of the dimensions except the last one, which is left open. Then we study the reflection from the  $d$ -direction back onto itself. The reflection is given by

$$\psi_{d,\text{out}} = r(\mathbf{k})\psi_{d,\text{in}}, \quad (3.18)$$

$$r(\mathbf{k}) = D - C[A - Z_{d-1}(\mathbf{k})]^{-1}B, \quad (3.19)$$

with  $Z_{d-1}$  given by Eq. (3.12) in  $d-1$  dimensions. The matrices  $A$ ,  $B$ ,  $C$ , and  $D$  are sub-blocks of  $S$  given by

$$\begin{aligned} A &= \begin{pmatrix} S_{1,1} & \cdots & S_{1,\overline{d-1}} \\ \vdots & \ddots & \vdots \\ S_{\overline{d-1},1} & \cdots & S_{\overline{d-1},\overline{d-1}} \end{pmatrix}, & B &= \begin{pmatrix} S_{1,d} \\ \vdots \\ S_{\overline{d-1},d} \end{pmatrix}, \\ C &= (S_{d,1} \quad \cdots \quad S_{d,\overline{d-1}}), & D &= (S_{d,d}). \end{aligned} \quad (3.20)$$

To study topological properties of  $r(\mathbf{k})$  we construct an effective Hamiltonian  $H_{d-1}(\mathbf{k})$  which has band gap closings whenever  $r(\mathbf{k})$  has zero eigenvalues. In classes possessing chiral symmetry one may choose a basis such that  $r(\mathbf{k}) = r^\dagger(\mathbf{k})$ . If chiral symmetry is absent, there is no

Hermiticity condition on  $r$ , so we double the degrees of freedom to construct a single Hermitian matrix out of a complex one. The effective Hamiltonian is then given by

$$H_{d-1}(\mathbf{k}) \equiv r(\mathbf{k}), \quad \text{with chiral symmetry,} \quad (3.21a)$$

$$H_{d-1}(\mathbf{k}) \equiv \begin{pmatrix} 0 & r(\mathbf{k}) \\ r^\dagger(\mathbf{k}) & 0 \end{pmatrix}, \quad \text{without chiral symmetry.} \quad (3.21b)$$

It is straightforward to verify that in both cases the Hamiltonian  $H_{d-1}(\mathbf{k})$  has band gap closings simultaneously with the appearance of vanishing eigenvalues of  $r(\mathbf{k})$ .

If  $r(\mathbf{k})$  has chiral symmetry,  $H_{d-1}(\mathbf{k})$  does not have it. On the other hand, if  $r(\mathbf{k})$  has no chiral symmetry, then

$$H_{d-1}(\mathbf{k}) = -\tau_z H_{d-1}(\mathbf{k}) \tau_z, \quad (3.22)$$

with  $\tau_z$  the third Pauli matrix in the space of the doubled degrees of freedom. This means that in that case  $H_{d-1}(\mathbf{k})$  acquires chiral symmetry.

The way in which the dimensional reduction changes the symmetry class is summarized in Fig. 3.2. The transformation of symmetries of  $r(\mathbf{k})$  into symmetries of  $H_{d-1}(\mathbf{k})$  is straightforward in all of the cases, except the time-reversal symmetry in symmetry classes AII and AI. There we have  $r(\mathbf{k}) = \pm r^T(-\mathbf{k})$ , and hence

$$\begin{aligned} H_{d-1}(\mathbf{k}) &\equiv \begin{pmatrix} 0 & r(\mathbf{k}) \\ r^\dagger(\mathbf{k}) & 0 \end{pmatrix} \\ &= \begin{pmatrix} 0 & \pm r(-\mathbf{k})^T \\ \pm [r^T(-\mathbf{k})]^\dagger & 0 \end{pmatrix} = \pm \tau_x H_{d-1}^*(-\mathbf{k}) \tau_x. \end{aligned} \quad (3.23)$$

The details of the symmetry properties of  $r$  and  $H$ , as well as the relations between these symmetries are given in App. 3.7.1.

The way the symmetry class of the  $d$ -dimensional Hamiltonian transforms into the symmetry class of  $H_{d-1}(\mathbf{k})$  expresses the Bott periodicity of the topological classification of symmetry classes [2]. Namely, symmetry classes A and AIII transform into each other, and the other 8 classes with anti-unitary symmetries are shifted by one, as shown in Table 3.1. This reproduces the natural succession of symmetry classes that appears in the context of symmetry breaking [22] (see also Appendix 3.7.1). The combined effects of the change in dimensionality and in symmetry class is that the Hamiltonians  $H(\mathbf{k})$  and  $H_{d-1}(\mathbf{k})$  have the same topological classification.

		particle-hole symmetry		
		- 1	×	1
time-reversal symmetry	- 1	<b>CII</b> $\mathcal{T} : r(\mathbf{k}) = \sigma_y r^T(-\mathbf{k}) \sigma_y$ $\mathcal{P} : \boxed{r(\mathbf{k}) = \sigma_y r^*(-\mathbf{k}) \sigma_y}$ $\mathcal{P} : H(\mathbf{k}) = -\tau_z \sigma_y H^*(-\mathbf{k}) \sigma_y \tau_z$ $\mathcal{T} : \boxed{\tilde{H}(\mathbf{k}) = \sigma_y H^*(-\mathbf{k}) \sigma_y}$	<b>AII</b> $\mathcal{T} : \boxed{r(\mathbf{k}) = -r^T(-\mathbf{k})}$ $\mathcal{T} : \boxed{\tilde{H}(\mathbf{k}) = \sigma_y H^*(-\mathbf{k}) \sigma_y}$	<b>DIII</b> $\mathcal{T} : H(\mathbf{k}) = \tau_y H^*(-\mathbf{k}) \tau_y$ $\mathcal{P} : \boxed{\tilde{H}(\mathbf{k}) = -\tau_x H^*(-\mathbf{k}) \tau_x}$ $\mathcal{T} : r(\mathbf{k}) = -r^T(-\mathbf{k})$ $\mathcal{P} : \boxed{r(\mathbf{k}) = -r^*(-\mathbf{k})}$
	×	<b>C</b> $\mathcal{P} : \boxed{r(\mathbf{k}) = \sigma_y r^*(-\mathbf{k}) \sigma_y}$ $\mathcal{P} : \boxed{\tilde{H}(\mathbf{k}) = -\sigma_y H^*(-\mathbf{k}) \sigma_y}$	<b>A</b> $\boxed{r(\mathbf{k})}$ - no symmetry $\boxed{\tilde{H}(\mathbf{k}) = H^\dagger(\mathbf{k})}$ $\mathcal{C} : \boxed{r(\mathbf{k}) = r^\dagger(\mathbf{k})}$ $\mathcal{C} : \boxed{H(\mathbf{k}) = -\tau_z H(\mathbf{k}) \tau_z}$	<b>D</b> $\mathcal{P} : \boxed{\tilde{H}(\mathbf{k}) = -H^*(-\mathbf{k})}$ $\mathcal{P} : \boxed{r(\mathbf{k}) = -r^*(-\mathbf{k})}$
	1	<b>CI</b> $\mathcal{P} : \boxed{r(\mathbf{k}) = -\sigma_y r^*(-\mathbf{k}) \sigma_y}$ $\mathcal{T} : r(\mathbf{k}) = -\sigma_y r^T(-\mathbf{k}) \sigma_y$ $\mathcal{T} : \boxed{\tilde{H}(\mathbf{k}) = \tau_x H^*(-\mathbf{k}) \tau_x}$ $\mathcal{P} : H(\mathbf{k}) = -\tau_y H^*(-\mathbf{k}) \tau_y$	<b>AI</b> $\mathcal{T} : \boxed{r(\mathbf{k}) = r^T(-\mathbf{k})}$ $\mathcal{T} : \boxed{\tilde{H}(\mathbf{k}) = H^*(-\mathbf{k})}$	<b>BDI</b> $\mathcal{T} : H(\mathbf{k}) = \tau_z H^*(-\mathbf{k}) \tau_z$ $\mathcal{P} : \boxed{\tilde{H}(\mathbf{k}) = -H^*(-\mathbf{k})}$ $\mathcal{P} : \boxed{r(\mathbf{k}) = r^*(-\mathbf{k})}$ $\mathcal{T} : r(\mathbf{k}) = r^T(-\mathbf{k})$

**Figure 3.2.** Symmetry properties of  $r(\mathbf{k})$  and  $H(\mathbf{k})$  in the ten symmetry classes. Time-reversal symmetry is denoted by  $\mathcal{T}$ , particle-hole symmetry by  $\mathcal{P}$ . The signs at the top and left of the table denote either the absence ( $\times$ ) of a corresponding symmetry, or the value of the squared symmetry operator. The entries of the table with a gray background have an additional chiral symmetry  $\mathcal{C}$ , which always has the form shown in the AIII entry of the table. In particular, we always chose a basis such that  $r(\mathbf{k}) = r^\dagger(\mathbf{k})$  in the chiral symmetry classes. The way symmetry classes transform under our definition of  $H_{d-1}$ , cf. (3.21), is denoted by the arrows; the double arrow implies a doubling of degrees of freedom as in Eq. (3.21b). Going along an arrow, the symmetry of the reflection block  $r(\mathbf{k})$  (marked by a solid box) transforms into the symmetry of the reduced Hamiltonian (marked by a dashed box). In the chiral classes, there is an additional symmetry (not marked by a box) which can be obtained from the other by combining it with the chiral symmetry,  $H(\mathbf{k}) = -\tau_z H(\mathbf{k}) \tau_z$  and  $r(\mathbf{k}) = r^\dagger(\mathbf{k})$ , respectively.

We now turn to prove that for localized systems topological invariants  $\mathcal{Q}(H)$  and  $\mathcal{Q}(H_{d-1})$  are identical. This correspondence was proven in 1D in Ref. 7, so here we accomplish the proof in higher dimensions.

First of all, we observe that a topologically trivial Hamiltonian can be deformed into a bunch of completely decoupled localized orbitals without closing its gap. In a sufficiently large system, this also means that the gap of  $H_{d-1}(\mathbf{k})$  does not close during this process. For a system



Symmetry class	$d$							
	1	2	3	4	5	6	7	8
A	-	$\mathbb{Z}$	-	$\mathbb{Z}$	-	$\mathbb{Z}$	-	$\mathbb{Z}$
AIII	$\mathbb{Z}$	-	$\mathbb{Z}$	-	$\mathbb{Z}$	-	$\mathbb{Z}$	-
AI	-	-	-	$\mathbb{Z}$	-	$\mathbb{Z}_2$	$\mathbb{Z}_2$	$\mathbb{Z}$
BDI	$\mathbb{Z}$	-	-	-	$\mathbb{Z}$	-	$\mathbb{Z}_2$	$\mathbb{Z}_2$
D	$\mathbb{Z}_2$	$\mathbb{Z}$	-	-	-	$\mathbb{Z}$	-	$\mathbb{Z}_2$
DIII	$\mathbb{Z}_2$	$\mathbb{Z}_2$	$\mathbb{Z}$	-	-	-	$\mathbb{Z}$	-
AII	-	$\mathbb{Z}_2$	$\mathbb{Z}_2$	$\mathbb{Z}$	-	-	-	$\mathbb{Z}$
CII	$\mathbb{Z}$	-	$\mathbb{Z}_2$	$\mathbb{Z}_2$	$\mathbb{Z}$	-	-	-
C	-	$\mathbb{Z}$	-	$\mathbb{Z}_2$	$\mathbb{Z}_2$	$\mathbb{Z}$	-	-
CI	-	-	$\mathbb{Z}$	-	$\mathbb{Z}_2$	$\mathbb{Z}_2$	$\mathbb{Z}$	-

**Table 3.1.** (Color online) Topological classification of the ten symmetry classes in different dimensions. Combinations of symmetry class and dimensionality which support non-trivial topological invariants are indicated by the type of the topological invariant ( $\mathbb{Z}$  or  $\mathbb{Z}_2$ ). Classes which support only trivial insulators are denoted by '-'. The arrows indicate the change of symmetry class upon dimensional reduction as discussed in the main text. The topmost symmetries A and AIII (which do not have any anti-unitary symmetries) transform into each other, whereas the remaining 8 classes (with anti-unitary symmetries) exchange cyclically. The dimensional reduction changes the symmetry class, but preserves the topological invariant ('-',  $\mathbb{Z}$ , or  $\mathbb{Z}_2$ ).

of decoupled orbitals,  $r(\mathbf{k})$  and accordingly  $H_{d-1}(\mathbf{k})$  are momentum-independent (and hence  $H_{d-1}(\mathbf{k})$  is topologically trivial). This means that a sufficiently large system with trivial  $H(\mathbf{k})$  maps onto a trivial  $H_{d-1}(\mathbf{k})$  under the scheme of dimensional reduction outlined above.

Let us now consider an interface between two systems with different bulk Hamiltonians  $H$  and  $H'$ , shown in Fig. 3.3. If the Hamiltonians  $H_{d-1}$  and  $H'_{d-1}$  constructed out of reflection blocks of the two systems have different topological invariants, a topologically protected zero energy edge state in  $d - 1$  dimensions must appear at the interface between

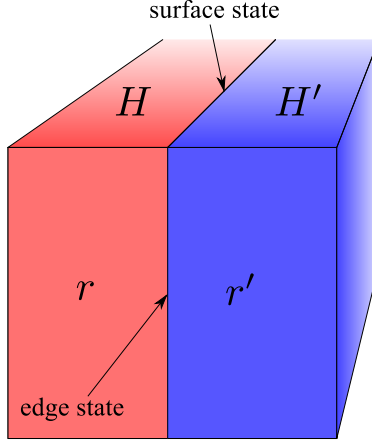


**Figure 3.3.** A system in  $d$  dimensions consisting out of two parts with different Hamiltonians  $H$  and  $H'$ . Reflection blocks of the scattering matrix  $r$  and  $r'$  are used to define the lower dimensional Hamiltonians  $H_{d-1}$  and  $H'_{d-1}$ . We prove the correspondence between topological invariants in  $d$  and  $d - 1$  dimensions using the relation between the surface state at the interface between  $H$  and  $H'$  and the edge state at the interface between  $H_{d-1}$  and  $H'_{d-1}$ .

them. Recalling that a zero energy edge state in  $d - 1$  dimension corresponds to a perfectly transmitting mode of the original  $d$ -dimensional system, we conclude that  $H$  and  $H'$  have different topological invariants.

Conversely, if  $H$  and  $H'$  have different topological invariants, there exists a transmitting mode at the interface between two parts of the system, which appears irrespective of system size and microscopic details of the interface. This means that it is not possible to construct an interface between  $H_{d-1}$  and  $H'_{d-1}$  which would be completely gapped.

Finally, the edge states in  $d - 1$  dimension have to have the same group properties as the surface states in  $d$  dimensions, leading us to the conclusion that  $\mathcal{Q}(H) = \mathcal{Q}(H_{d-1})$ , as we set out to prove. The topology-preserving property of our dimensional reduction procedure is the same as that of the mapping from a general  $d$ -dimensional Hamiltonian to a  $d + 1$ -dimensional Hamiltonian presented in Ref. 23.

At this point one might wonder why we apply the dimensional reduction only once. Indeed, the reduced Hamiltonian  $H_{d-1}$  can be straightforwardly approximated by a tight-binding Hamiltonian on a  $d - 1$  dimensional lattice using a Fourier transform. This allows to repeat the procedure of dimensional reduction until we arrive at a zero

dimensional Hamiltonian. We stop at the first dimensional reduction for practical purposes, since the advantage of considering only Fermi level properties is achieved already at the first step.

### 3.4 Results for one–three dimensions

#### 3.4.1 Topological invariant in 1D

We begin by verifying that we recover the 1D results of Ref. 7, where the topological invariant was related to the scattering matrix without going through the procedure of dimensional reduction. Dimensional reduction in this case brings us to a zero-dimensional Hamiltonian. The topological invariant of a zero-dimensional Hamiltonian without symmetry between positive and negative energies (symmetry classes A, AI, and AII) is given just by the number of states below the Fermi level. In class AII Kramers' degeneracy makes this number always even. In addition, in 0D there exist two  $\mathbb{Z}_2$  topological insulators in symmetry classes D and BDI. The topological number is in that case the ground state fermion parity, or the Pfaffian of the Hamiltonian in the basis where it is antisymmetric. To summarize,

$$\mathcal{Q}(H) = \nu(H), \quad \text{for A, AI, and AII,} \quad (3.24a)$$

$$\mathcal{Q}(H) = \text{Pf } iH, \quad \text{for D and BDI,} \quad (3.24b)$$

where  $\nu(A)$  denotes the number of negative eigenvalues of the Hermitian matrix  $A$ . Substituting  $H$  from Eqs. (3.21) yields

$$\mathcal{Q} = \nu(r), \quad \text{for AIII, BDI, and CII} \quad (3.25a)$$

$$\mathcal{Q} = \text{Pf } ir, \quad \text{for DIII,} \quad (3.25b)$$

$$\begin{aligned} \mathcal{Q} &= \text{Pf} \begin{pmatrix} 0 & ir \\ -ir^T & 0 \end{pmatrix} \\ &= \det r, \quad \text{for D.} \end{aligned} \quad (3.25c)$$

We confirm that the Eqs. (3.25) are in agreement with Ref. 7.

#### 3.4.2 Topological invariant in 2D

Starting from 2D, the dimensional reduction brings us to a 1D Hamiltonian. In this subsection we first review the known expressions for

the topological invariants of 1D Hamiltonians, and then describe how to efficiently evaluate it for the effective Hamiltonian (3.21). The  $\mathbb{Z}$  topological insulators in 1D (classes AIII, BDI, and CII) are characterized by a winding number [19, 20]

$$H(k) \equiv \begin{pmatrix} 0 & h(k) \\ h^\dagger(k) & 0 \end{pmatrix}, \quad (3.26)$$

$$\mathcal{Q}(H) = \frac{1}{2\pi i} \int_0^{2\pi} dk \frac{d}{dk} \log \det h(k),$$

for AIII, BDI, and CII. (3.27)

The topological invariant for the Hamiltonian in class D is given by Kitaev's formula [24]

$$\mathcal{Q}(H) = \text{sign} \left[ \frac{\text{Pf } H(0)}{\text{Pf } H(\pi)} \right], \quad \text{for D.} \quad (3.28)$$

Finally, in class DIII the expression for the topological invariant was derived in Ref. 25:

$$\begin{aligned} \mathcal{Q}(H) &= \frac{\text{Pf}[U_{\mathcal{T}}h(\pi)]}{\text{Pf}[U_{\mathcal{T}}h(0)]} \exp \left[ -\frac{1}{2} \int_0^\pi dk \frac{d}{dk} \log \det h(k) \right] \\ &= \frac{\text{Pf}[U_{\mathcal{T}}h(\pi)]}{\text{Pf}[U_{\mathcal{T}}h(0)]} \frac{\sqrt{\det h(0)}}{\sqrt{\det h(\pi)}}, \quad \text{for DIII,} \end{aligned} \quad (3.29)$$

where the square root is defined through analytic continuation over the first half of the Brillouin zone,  $h$  is defined by Eq. (3.26), and  $U_{\mathcal{T}}$  is the unitary part of the time reversal operator  $\mathcal{T} = U_{\mathcal{T}}\mathcal{K}$ .

Substituting Eq. (3.21) into the expressions for topological charge we get

$$\mathcal{Q} = \frac{1}{2\pi i} \int_0^{2\pi} dk \frac{d}{dk} \log \det r(k), \quad \text{for A, C, D} \quad (3.30a)$$

$$\mathcal{Q} = \frac{\text{Pf}[U_{\mathcal{T}}r(\pi)]}{\text{Pf}[U_{\mathcal{T}}r(0)]} \frac{\sqrt{\det r(0)}}{\sqrt{\det r(\pi)}}, \quad \text{for AII,} \quad (3.30b)$$

$$\mathcal{Q} = \text{sign} \left[ \frac{\text{Pf } r(0)}{\text{Pf } r(\pi)} \right], \quad \text{for DIII.} \quad (3.30c)$$

In order to efficiently evaluate the integral given in Eq. (3.27), and the analytic continuation in Eq. (3.30b) using Eq. (3.19), we define a new

variable  $z = e^{ik}$ . Then we perform an analytic continuation of  $\det r(z)$  to the complex plane from the unit circle  $|z| = 1$ . To find zeros and poles of  $\det r(z)$  we use

$$\det r(z) = \det \begin{pmatrix} A - Z_1(k) & B \\ C & D \end{pmatrix} / \det [A - Z_1(k)], \quad (3.31)$$

where

$$Z_1(k) = \begin{pmatrix} 0 & e^{ik} \\ e^{-ik} & 0 \end{pmatrix} = \begin{pmatrix} 0 & z \\ z^{-1} & 0 \end{pmatrix};$$

Equation (3.31) follows from Eq. (3.19) and the determinant identity

$$\det(D - CM^{-1}B) = \det \begin{pmatrix} M & B \\ C & D \end{pmatrix} / \det M. \quad (3.32)$$

Since both the numerator and the denominator of Eq. (3.31) are finite at any finite value of  $z$ , the roots of the numerator  $z_n$  are the zeros of  $\det r(z)$ , and the roots of the denominator  $w_n$  are the poles. In App. 3.7.2 we show that due to unitarity of the scattering matrix, the poles of  $\det r(z)$  never cross the unit circle. By multiplying the second column of the numerator of Eq. (3.31) by  $z$  we bring the problem of finding roots  $z_n$  of this numerator to the generalized eigenvalue problem,

$$\begin{pmatrix} S_{1,1} & -1 & S_{1,2} \\ S_{\bar{1},1} & 0 & S_{\bar{1},2} \\ S_{2,1} & 0 & S_{2,2} \end{pmatrix} \psi_n = z_n \begin{pmatrix} 0 & -S_{1,\bar{1}} & 0 \\ 1 & -S_{\bar{1},\bar{1}} & 0 \\ 0 & -S_{2,\bar{1}} & 0 \end{pmatrix} \psi_n, \quad (3.33)$$

which can be efficiently evaluated. The roots  $w_n$  of the denominator can also be found by solving the generalized eigenvalue problem,

$$\begin{pmatrix} S_{1,1} & -1 \\ S_{\bar{1},1} & 0 \end{pmatrix} \psi_n = w_n \begin{pmatrix} 0 & -S_{1,\bar{1}} \\ 1 & -S_{\bar{1},\bar{1}} \end{pmatrix} \psi_n. \quad (3.34)$$

Since the poles of  $\det r(z)$  never cross the unit circle, in classes A, C, and D the topological invariant is given by

$$\mathcal{Q} = \#\{z_n : |z_n| < 1\} - N_1, \quad \text{for A, C, and D,} \quad (3.35)$$

i.e., the number of  $z_n$ 's inside the unit circle minus the number of modes  $N_1$  in the direction 1. In class AII (quantum spin Hall insulator) the

topological invariant is given by

$$\mathcal{Q} = \frac{\prod_n \sqrt{i \frac{1+z_n}{1-z_n}}}{\prod_n \sqrt{(-i) \frac{1+w_n}{1-w_n}}} \times \frac{\text{Pf } U_{\mathcal{T}} r(\pi)}{\text{Pf } U_{\mathcal{T}} r(0)} \quad \text{for AII}, \quad (3.36)$$

with the branch cut of the square root along the negative real axis. Note that the linear fractional transformation  $z \mapsto i(1+z)/(1-z)$  maps the upper half of the unit circle onto the negative real axis. In symmetry class DIII the evaluation of the topological invariant is most straightforward, and yields

$$\mathcal{Q} = \text{sign} \left[ \frac{\text{Pf } r(0)}{\text{Pf } r(\pi)} \right] \quad \text{for DIII}. \quad (3.37)$$

The physical meaning of the topological invariant in class A is quantized pumping of charge as a response to magnetic flux. In the quantum spin Hall insulator in class AII the invariant can be interpreted either as time-reversal polarization pumping [26], or as pumping of spin which is quantized along an unknown axis [27, 28]. In the superconducting classes C, D, and DIII it is an analogous thermal or gravitational response [29, 30].

### 3.4.3 Topological invariant in 3D

Turning now to 3D, we need to consider topological invariants of 2D Hamiltonians. The symmetry class with the simplest expression for the topological invariant in terms of the scattering matrix in 3D is AII. The 2D topological invariant of a system in class DIII (into which AII transforms upon dimensional reduction) is a product [25] of the topological invariants (3.29) of 1D Hamiltonians obtained by setting one of the momenta to 0 or  $\pi$ ,

$$\mathcal{Q}[H(k_1, k_2)] = \mathcal{Q}[H(k_1, 0)] \mathcal{Q}[H(k_1, \pi)], \quad (3.38)$$

with  $\mathcal{Q}[H(k_1)]$  given by Eq. (3.29). Substituting Eq. (3.21) into this expression we obtain

$$\mathcal{Q} = \frac{\text{Pf}[U_{\mathcal{T}} r(\pi, 0)]}{\text{Pf}[U_{\mathcal{T}} r(0, 0)]} \frac{\sqrt{\det r(0, 0)}}{\sqrt{\det r(\pi, 0)}} \times \frac{\text{Pf}[U_{\mathcal{T}} r(\pi, \pi)]}{\text{Pf}[U_{\mathcal{T}} r(0, \pi)]} \frac{\sqrt{\det r(0, \pi)}}{\sqrt{\det r(\pi, \pi)}}, \quad \text{for AII}. \quad (3.39)$$

Direct evaluation of the Hamiltonian topological invariant in 2D in classes with nontrivial Chern number (A, C, D), and in class AII is hard because of the need to fix the gauge throughout the Brillouin zone [12, 26]. It is usually more efficient to use a method which relies on the real space structure of  $H$  evaluated in a single point in momentum space [4, 5, 31, 32]. These methods using the Bott index or a similar expression for the topological invariant require the so-called band-projected position operators:  $x_P = P \exp(2\pi i x) P$  and  $y_P = P \exp(2\pi i y) P$ . Here  $P$  is the projector on the states of the Hamiltonian with negative energies, and  $x$  and  $y$  are the coordinate operators in the unit cell of the system. In order to evaluate these operators in our case we note that the eigenvalues of the effective Hamiltonian in the symmetry classes of interest approach  $\pm 1$  when the original system becomes localized. In that case  $P = (1 - r)/2$  [with  $r \equiv r(0, 0)$ ], and we can avoid the need to calculate the projector explicitly if we approximate  $x_P$  and  $y_P$  by

$$x_P \approx (1 + r)/2 + (1 - r)e^{2\pi i x}(1 - r)/4, \quad (3.40)$$

$$y_P \approx (1 + r)/2 + (1 - r)e^{2\pi i y}(1 - r)/4. \quad (3.41)$$

Using the 2D Hamiltonian expressions from Ref. 33 we arrive at a scattering formula for the 3D topological invariant,

$$Q = \frac{1}{2\pi} \text{Im tr log}[x_P y_P x_P^\dagger y_P^\dagger], \quad \text{for AIII, CI, DIII.} \quad (3.42)$$

The symmetry class CII in 3D transforms upon dimensional reduction to class AII in 2D. The expressions for the Pfaffian-Bott index required to calculate the topological invariant for a 2D Hamiltonian in class AII are quite involved. We do not give them here, but refer the interested reader to Eqs. (7), (9), and (10) of Ref. 4.

### 3.4.4 Weak invariants

All of the algorithms described above apply directly to the weak topological invariants [34, 35, 10]. In order to evaluate a weak invariant one just needs to eliminate one of the dimensions by setting the momentum along that dimension to either 0 or  $\pi$ , and to evaluate the appropriate topological invariant for the resulting lower dimensional system. The only caveat is that since weak topological indices do not survive doubling of the unit cell, the thickness of the system in the transverse direction should be equal to the minimal unit cell. In the same fashion

(eliminating one momentum or more) one can calculate the presence of surface states [36] in chiral superconductors and Fermi arcs [37] in 3D systems.

## 3.5 Applications and performance

### 3.5.1 Performance

The complexity of the Hamiltonian expressions scales with linear system size  $L$  as  $L^2$  in 1D, and as  $L^{3d}$  in higher dimensions. In contrast, the complexity of the scattering matrix expressions scales proportionally to  $L$  in 1D and to  $L^{3d-3}$  in higher dimensions [38, 39]. All the subsequent operations have the same or a more favorable scaling. We use the algorithm of Ref. 40 to calculate the Pfaffian of an arbitrary skew-symmetric matrix.

We have verified that using the scattering matrix method allows to efficiently calculate the topological invariant of a quantum Hall system and of the BHZ model [41] discretized on a square lattice with a size of  $1000 \times 1000$ . This improves considerably on previously reported [4, 42] results of up to  $50 \times 50$  lattice sites for the BHZ model.

In 3D the improvement in performance is not as large because the values of  $L$  that we can reach are smaller. Nevertheless, we have confirmed that it is possible to calculate the topological invariant of 3D systems in classes AII and DIII using a 4-band model on a cubic lattice with system size  $50 \times 50 \times 50$ . This is a significant improvement over the  $12 \times 12 \times 12$  size, reported for Hamiltonian-based methods [6].

In addition to tight-binding models, our method applies very naturally to various network models [43–45], which are favorite models for the phase transitions. Hamiltonian-based approaches are not applicable to the network models, since those only have a scattering matrix, and no lattice Hamiltonian. We have checked that calculating a topological invariant of the Chalker-Coddington network model of size  $1000 \times 1000$  only takes several minutes on modern hardware.

### 3.5.2 Finite size effects

The expressions for the topological invariant given in terms of the scattering matrix in Sec. 3.4 do not coincide with  $\mathcal{Q}(H)$  very close to the



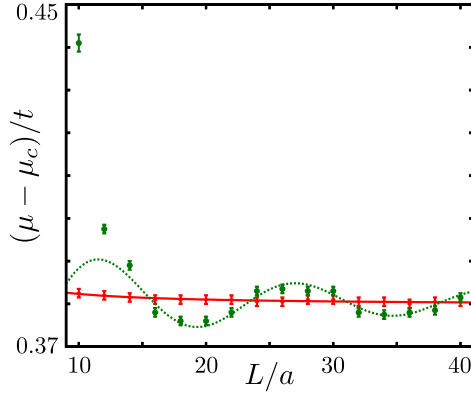


**Figure 3.4.** The value of the chemical potential  $\mu_c$  where the ensemble averaged topological invariant equals to 0.5, as a function of system size  $L$ . Red: topological invariant defined in terms of the scattering matrix, from Eq. (3.35). Green: topological invariant obtained from the Hamiltonian expression of Ref. 4. Lines represent fits as described in the text.

transition. This is a finite size effect. In order to estimate the importance of finite size effects we have computed the shift of the transition point between the  $n = 0$  and  $n = 1$  plateaus of a disordered quantum Hall system as a function of size. We have used a square lattice discretization (lattice constant  $a$ ) of a single band tight binding model with nearest neighbor hopping  $t = 1$ . The magnetic flux per unit cell of the lattice was fixed at  $0.4\hbar/e$ . We used on-site disorder homogeneously distributed on an interval  $[-0.05, 0.05]$ .

The transition point is defined as the value of the chemical potential  $\mu_c$  at which the disorder-averaged topological invariant equals 0.5. We have compared two expressions for the topological invariant: the scattering matrix expression (3.35) and the Hamiltonian expression from Ref. 4. The results are shown in Fig. 3.4. We fit the data obtained via the scattering matrix approach to the function  $f(L) = c_1 + c_2/L$  obtaining a value  $c_2 \approx 0.026$ . In the case of the expression of Ref. 4, the finite size effects are best fit to the function  $g(L) = c'_1 + c'_2 \sin(c_3 L + c_4)/L$ , with  $c'_2 \approx 0.116$ . We conclude that the finite size effects of our algorithm are significantly lower.

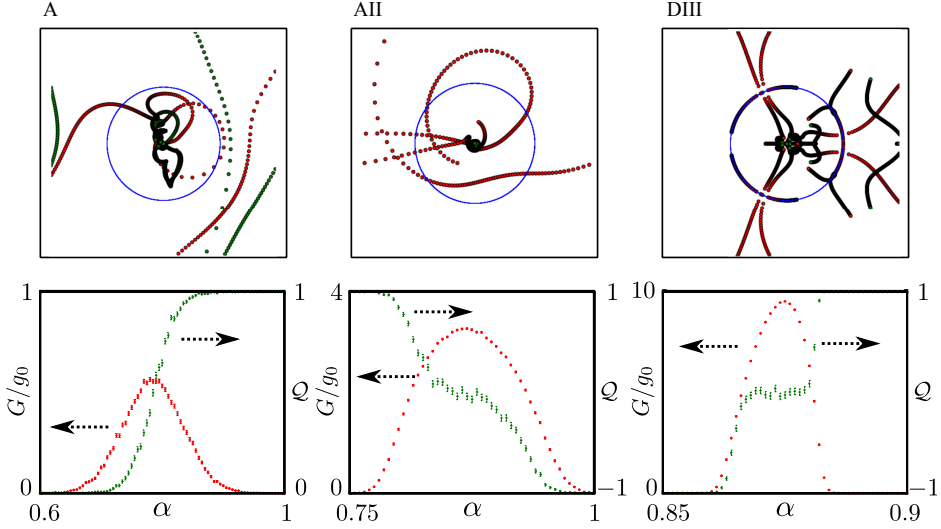


**Figure 3.5.** Top panel: Evolution of the poles (green dots) and the zeros (red dots) of  $\det r(z)$  as a function of a parameter  $\alpha$  which tunes through the topological phase transition in classes A, AII, and DIII in 2D. Shown is the complex plane with the unit circle  $|z| = 1$  indicated in blue. Time-reversal symmetry in AII and DIII implies that for every zero/pole at  $z_0$  there is additionally one at  $1/z_0$ . In DIII, there is additional particle-hole symmetry which additionally dictates zeros/poles at  $z_0^*$  and  $1/z_0^*$ . The phase transition happens when at least one of the zeros crosses the unit circle. This event coincides with a change of the topological invariant  $Q$  (green) defined by Eqs. (3.35 – 3.37), as shown in the bottom panels.

### 3.5.3 Applications

In 2D we illustrate our approach by applying it to network models in classes A, AII, and DIII. In class A we use the Chalker-Coddington network model [43]. In classes AII and DIII we have used the quantum spin Hall network model of Ref. 45. In class DIII we have set the link phases to zero in order to ensure particle-hole symmetry. In each of these cases the parameter which tunes through the transition is the angle  $\alpha$  related to reflection probability at a node of the network by  $R = \cos^2 \alpha$ .

Our results are summarized in Fig. 3.5. Top panels show the evolution of zeros and poles of  $\det r(z)$  across the phase transition — the ‘fingerprint’ of a topological phase transition [46]. There are no symmetry constraints on this fingerprint in class A. The time-reversal symmetry

ensures that for every zero or pole at  $z_0$  there is another one at  $1/z_0$ . The particle-hole symmetry translates into the mirror symmetry with respect to the real axis: for every zero or pole at  $z_0$  there is one at  $z_0^*$ . The bottom panels show the behavior of the topological invariant and of the conductance  $G = \text{tr } t^\dagger t$ , with  $t$  the transmission matrix through the system. The simulations were performed on systems of size  $300 \times 300$  in each of the symmetry classes and averaged over 1000 samples. The presence of plateaus around zero in the curves for the topological invariant coincides with the presence of a metallic phase in the phase diagram of symmetry classes AII and DIII.

Although we introduced the topological invariant through transport properties, it does not always have the same features as the conductance. The topological invariant characterizes winding of scattering modes in the transverse direction. Accordingly, in a system with a large ratio of width  $W$  to the length  $L$ , the width of the transition of the topological invariant is reduced. The width of the peak in the conductance, on the contrary, is reduced if  $W/L$  becomes small. This is in agreement with what we observe in numerical simulations. We have calculated the topological invariant and conductance averaged over 1000 disorder realizations in the Chalker-Coddington network model in systems with  $W = 300$  and  $L = 60$  and vice versa. The results are shown in Fig. 3.6 and they agree with our expectations.

We have also studied a 3D topological system in class AII on a cubic lattice. We have used a simplified version of the Hamiltonian of Ref. 47:

$$H = \begin{pmatrix} \mathcal{M}(\mathbf{k}) & vk_z & 0 & vk_- \\ vk_z & -\mathcal{M}(\mathbf{k}) & vk_- & 0 \\ 0 & vk_+ & \mathcal{M}(\mathbf{k}) & -vk_z \\ vk_+ & 0 & -vk_z & -\mathcal{M}(\mathbf{k}) \end{pmatrix} - \mu \quad (3.43)$$

discretized on cubic lattice with lattice constant  $a$ , where  $k_\pm = k_x \pm ik_y$ , and  $\mathcal{M}(\mathbf{k}) = M - \alpha k^2$ . The Hamiltonian parameters were chosen to be  $\alpha = a^2$ ,  $v = a$ . We chose  $\mu = \mu_0 + \delta\mu$  with  $\mu_0 = 0.4$ , and  $\delta\mu$  being a random uncorrelated variable uniformly distributed in the interval  $[-2, 2]$ . The topological invariant defined by Eq. (3.39) as well as the longitudinal conductance for a  $20 \times 20 \times 20$  system averaged over 100 disorder realizations are shown in Fig. 3.7 as a function of  $M$ . We observe that, analogously to the two-dimensional case, the presence of a metallic phase is accompanied by a plateau in the topological charge at a value of zero.

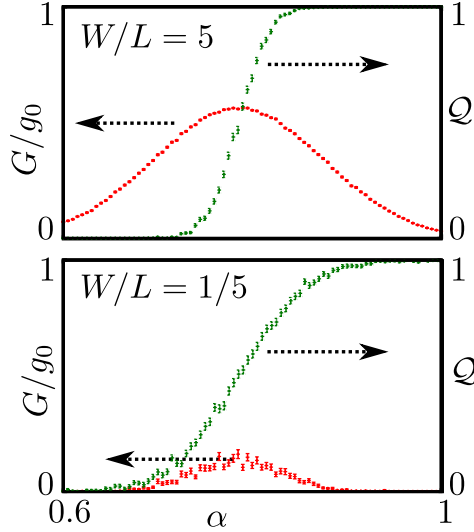


**Figure 3.6.** Average topological invariant  $\mathcal{Q}$  (3.35) and longitudinal conductance  $G$  of a disordered quantum Hall sample for different aspect ratios as a function of the mixing angle  $\alpha$ .

### 3.6 Conclusion

In conclusion, we have introduced a procedure of dimensional reduction which relates a scattering matrix of a  $d$ -dimensional system to a Hamiltonian in  $d - 1$  dimensions with a different symmetry class, but with the same topological invariant as the original system. When applied repeatedly this dimensional reduction procedure serves as an alternative derivation of the Bott periodicity of topological insulators and superconductors.

Since our approach uses only Fermi surface properties it is much more efficient than existing alternatives which require the analysis of the full spectrum. We have described how to implement our method efficiently in all the symmetry classes in 1–3 dimensions. We have verified that it allows to analyze much larger systems than previously possible.

This paper focused on the description of the method and we only touched on a few applications at the end. More applications can be envisaged and we believe that the scattering approach will lead to the discovery of new observable physics at topological phase transitions.

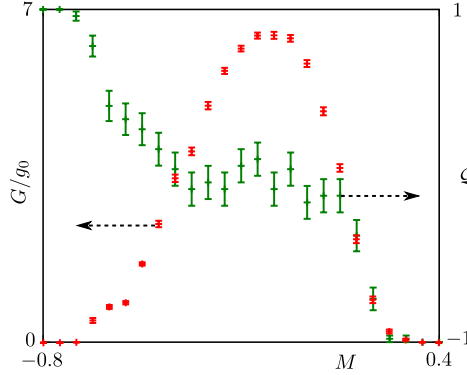


**Figure 3.7.** Conductance and topological invariant (3.39) for a disordered 3D topological insulator in class AII.

## 3.7 Appendix

### 3.7.1 Introduction to discrete symmetries

Here we define the three core discrete symmetries, and the corresponding symmetry constraints on the Hamiltonians and on the scattering matrices. We also specify how to choose the symmetry representation we used in Fig. 3.2.

#### Definitions and properties of discrete symmetries

The discrete symmetries are defined as follows: The time reversal symmetry operator  $\mathcal{T}$  is an anti-unitary operator. When it is applied to an arbitrary eigenstate  $\psi$  of the Hamiltonian  $H$  at energy  $\varepsilon$ , returns an eigenstate of the Hamiltonian at the same energy:

$$H\psi = \varepsilon\psi \Rightarrow H\mathcal{T}\psi = \varepsilon\mathcal{T}\psi \quad (3.44a)$$

On the other hand, the anti-unitary particle-hole symmetry operator  $\mathcal{P}$  returns an eigenstate with opposite energy when applied to any eigenstate of the Hamiltonian:

$$H\psi = \varepsilon\psi \Rightarrow H\mathcal{P}\psi = -\varepsilon\mathcal{P}\psi \quad (3.44b)$$

Chiral symmetry  $\mathcal{C}$  also reverses energy, but unlike the other two has a unitary operator.

All three symmetries  $\mathcal{T}, \mathcal{P}, \mathcal{C}$  are  $\mathbb{Z}_2$  symmetries, so the symmetry operators must square to a phase factor.

In an arbitrary basis the symmetry operators are represented by

$$\mathcal{T} = U_{\mathcal{T}}\mathcal{K}, \quad \mathcal{P} = U_{\mathcal{P}}\mathcal{K}, \quad \mathcal{C} = U_{\mathcal{C}}, \quad (3.45)$$

with  $\mathcal{K}$  denoting the complex conjugation, and  $U_{\mathcal{T}}, U_{\mathcal{P}},$  and  $U_{\mathcal{C}}$  unitary matrices. Since  $\exp(i\phi) = \mathcal{T}^2 = U_{\mathcal{T}}U_{\mathcal{T}}^*$ , and its determinant  $\det U_{\mathcal{T}}U_{\mathcal{T}}^*$  is real, we obtain  $U_{\mathcal{T}}U_{\mathcal{T}}^* = \pm 1$ ; similarly  $U_{\mathcal{P}}U_{\mathcal{P}}^* = \pm 1$ . In other words, every anti-unitary symmetry comes in two flavors, squaring either to  $+1$  or to  $-1$ . No such constraint applies to chiral symmetry, which may square to an arbitrary phase factor  $\exp(i\phi)$ . This factor however can always be set to zero by choosing  $U_{\mathcal{C}} \rightarrow U_{\mathcal{C}} \exp(-i\phi/2)$ .

The symmetry constraints on the Hamiltonian

$$H = \mathcal{T}H\mathcal{T}^{-1} = U_{\mathcal{T}}H^*U_{\mathcal{T}}^\dagger \quad (3.46a)$$

$$H = -\mathcal{P}H\mathcal{P}^{-1} = -U_{\mathcal{P}}H^*U_{\mathcal{P}}^\dagger \quad (3.46b)$$

$$H = -\mathcal{C}H\mathcal{C}^{-1} = -U_{\mathcal{C}}HU_{\mathcal{C}}^\dagger. \quad (3.46c)$$

follow immediately from the definition of the symmetries, Eq. (3.44).

### Relation between discrete symmetries and translational invariance

In addition to the basic properties, the discrete symmetries in periodic systems are required to commute with the coordinate operator. So for any Bloch wave written as

$$\psi(\mathbf{r}) = e^{i\mathbf{p}\mathbf{r}}\psi(0), \quad (3.47)$$

with  $\mathbf{r}$  coordinate in a translationally-invariant system, and  $\psi(0)$  the wave function inside a single unit cell, the action of the symmetry operators is:

$$\mathcal{T}\psi(\mathbf{r}) = e^{-i\mathbf{p}\mathbf{r}}\mathcal{T}\psi(0), \quad (3.48a)$$

$$\mathcal{P}\psi(\mathbf{r}) = e^{-i\mathbf{p}\mathbf{r}}\mathcal{P}\psi(0), \quad (3.48b)$$

$$\mathcal{C}\psi(\mathbf{r}) = e^{i\mathbf{p}\mathbf{r}}\mathcal{C}\psi(0). \quad (3.48c)$$

Since the velocity of a Hamiltonian eigenstate at energy  $\varepsilon$  and momentum  $\mathbf{p}$  is  $v = d\varepsilon/d\mathbf{p}$ , time-reversal and chiral symmetries reverse the velocity, while particle-hole symmetry keeps the velocity invariant.

### Symmetry constraints on scattering matrix

In order to figure out what the symmetry constraints on the scattering matrices are, we first review the basic properties of the scattering matrices. Scattering matrices act in the space of asymptotic scattering states outside of the scattering region. This space contains two non-intersecting subspaces: the subspace of incoming modes and the subspace of outgoing modes. The incoming modes are all the plane waves with velocity in the direction of the scattering region, and the outgoing modes are all the plane waves with velocity pointing away from the scattering region. Let  $\psi_n^{\text{in}}$  be a basis in the space of incoming modes, and  $\psi_n^{\text{out}}$  a basis in the space of outgoing modes. Conventionally all the modes are normalized such that current operator in the basis of  $\psi^{\text{in}}$  is the identity matrix, and the negative identity matrix in the basis of  $\psi^{\text{out}}$ .

The matrix elements of the scattering matrix  $S$  satisfy

$$(H - \varepsilon) \left( \psi_n^{\text{in}} + \sum_m S_{mn} \psi_m^{\text{out}} + \psi^{\text{loc}} \right) = 0, \quad (3.49)$$

with  $\psi^{\text{loc}}$  a wave-function localized near the scattering region.

As derived in the previous subsection, time-reversal and chiral symmetries change the velocity to its opposite, while particle-hole symmetry leaves the velocity invariant. This means that scattering states transform under the discrete symmetries in the following manner:

$$\begin{aligned} \mathcal{T} \psi_n^{\text{in}} &= \sum_m (V_{\mathcal{T}})_{nm} \psi_m^{\text{out}}, \\ \mathcal{T} \psi_n^{\text{out}} &= \sum_m (Q_{\mathcal{T}})_{nm} \psi_m^{\text{in}}, \\ \mathcal{C} \psi_n^{\text{in}} &= \sum_m (V_{\mathcal{C}})_{nm} \psi_m^{\text{out}}, \\ \mathcal{C} \psi_n^{\text{out}} &= \sum_m (Q_{\mathcal{C}})_{nm} \psi_m^{\text{in}}, \\ \mathcal{P} \psi_n^{\text{out}} &= \sum_m (V_{\mathcal{P}})_{nm} \psi_m^{\text{out}}, \\ \mathcal{P} \psi_n^{\text{in}} &= \sum_m (Q_{\mathcal{P}})_{nm} \psi_m^{\text{in}}. \end{aligned} \quad (3.50)$$

The additional constraints on the type of time-reversal, particle-hole,

and chiral symmetries require

$$\pm 1 = \mathcal{T}^2 = V_{\mathcal{T}} Q_{\mathcal{T}}^*, \quad (3.51a)$$

$$\pm 1 = \mathcal{P}^2 = V_{\mathcal{P}} V_{\mathcal{P}}^* = Q_{\mathcal{P}} Q_{\mathcal{P}}^*, \quad (3.51b)$$

$$1 = \mathcal{C}^2 = V_{\mathcal{C}} Q_{\mathcal{C}}. \quad (3.51c)$$

Applying time-reversal symmetry to Eq. (3.49) and using Eqs. (3.50) we get

$$(H - \varepsilon) \left( V_{\mathcal{T}} \psi_n^{\text{out}} + \sum_m S_{mn}^* Q_{\mathcal{T}} \psi_m^{\text{in}} + \mathcal{T} \psi^{\text{loc}} \right) = 0, \quad (3.52)$$

where we have also used that  $H$  is time-reversal invariant. Comparing with Eq. (3.49), we get

$$S^{-1} = Q_{\mathcal{T}}^T S^* V_{\mathcal{T}}, \quad (3.53)$$

which we can be reduced to

$$S = V_{\mathcal{T}}^T S^T Q_{\mathcal{T}}^*. \quad (3.54a)$$

Similarly, the chiral and the particle-hole symmetry constraints on  $S$  are:

$$S = V_{\mathcal{C}}^T S^+ V_{\mathcal{C}}^T, \quad (3.54b)$$

$$S = V_{\mathcal{P}}^T S^* Q_{\mathcal{P}}^*. \quad (3.54c)$$

Naturally, the constraints imposed by chiral and particle-hole symmetry only hold at zero excitation energy, since these symmetries anti-commute with the Hamiltonian. Finally, the symmetry constraints on the reflection matrix are identical to Eqs. (3.54), since  $r$  is a diagonal sub-block of  $S$ .

### Choice of symmetry representation and mapping from scattering matrix to Hamiltonian symmetries

The choice of symmetry representation is fully specified by choice of unitary matrices  $U_{\mathcal{O}}$ ,  $V_{\mathcal{O}}$ , and  $Q_{\mathcal{O}}$  ( $\mathcal{O} = \mathcal{T}, \mathcal{P}$ , or  $\mathcal{C}$ ). The symmetry representations used in the main text were chosen to make the mapping from the reflection matrix to an effective Hamiltonian most straightforward. In order to reach this aim, we always choose  $V_{\mathcal{O}} = \pm Q_{\mathcal{O}}$  for each of the three symmetries. Whenever chiral symmetry is present, we use

$$U_{\mathcal{C}} = \tau_z, \quad V_{\mathcal{C}} = Q_{\mathcal{C}} = 1. \quad (3.55)$$



Our choices of  $V$  and  $Q$  for the other two symmetries with

$$V_{\mathcal{T}} = V_{\mathcal{P}} \equiv V, \quad Q_{\mathcal{T}} = Q_{\mathcal{P}} \equiv Q \quad (3.56)$$

depend on the specific symmetry class. When  $\mathcal{P}^2 = -1$  (symmetry classes C, CI, CII) we choose  $V = \sigma_y$ , and we choose  $V = 1$  in symmetry classes D, DIII, and BDI, where  $\mathcal{P}^2 = 1$ . The relative sign between  $V$  and  $Q$  follows from Eq. (3.51):

$$Q = \mathcal{P}^2 \mathcal{T}^2 V. \quad (3.57)$$

In the remaining two classes AI and AII we choose  $V = 1$ , and  $Q = \mathcal{T}^2$ . Symmetry representations of the effective Hamiltonians follow immediately from Eqs. (3.21).

Finally we show how symmetry operators change upon creating an effective Hamiltonian from a reflection matrix. The effective Hamiltonian created from a reflection matrix with chiral symmetry satisfies

$$H = \mathcal{P}^2 \mathcal{T}^2 V H^* V, \quad (3.58)$$

so that the resulting symmetry of the effective Hamiltonian is particle-hole if  $\mathcal{P}^2 \mathcal{T}^2 = -1$ , and time-reversal if  $\mathcal{P}^2 \mathcal{T}^2 = 1$ . The symmetry operator of this symmetry squares to  $VV^*$ . If a reflection matrix has only time-reversal symmetry, then the time-reversal and particle-hole symmetry constraints on the effective Hamiltonian have the form

$$H = \pm V \otimes \tau_x H^* V \otimes \tau_x, \quad (3.59a)$$

$$H = \mp V \otimes \tau_y H^* V \otimes \tau_y, \quad (3.59b)$$

where the sign is determined by the choice of representation of the symmetry of  $r$ . Hence the symmetries of the effective Hamiltonian satisfy  $\mathcal{T}^2 = -\mathcal{P}^2$ . Finally, for an effective Hamiltonian constructed from a reflection matrix with only particle-hole symmetry, the resulting symmetry constraints on the Hamiltonian are

$$H = \pm V \otimes \tau_0 H^* V \otimes \tau_0, \quad (3.60a)$$

$$H = \mp V \otimes \tau_z H^* V \otimes \tau_z, \quad (3.60b)$$

so that both symmetry operators square to the same value.

### 3.7.2 Calculation of the number of poles

We prove that the equation

$$\det[A - Z_1(k)] = 0 \quad (3.61)$$

has  $N_1$  solutions with  $z = e^{ik}$  inside the unit circle, and  $N_1$  solutions outside of the unit circle as long as  $A^\dagger A$  only has eigenvalues less than one, which is generically the case since  $A$  is a sub-block of a unitary matrix  $S$ . Let us assume that  $\psi$  is an eigenvector of the corresponding eigenvalue problem:

$$A\psi = Z_1(k)\psi, \quad (3.62)$$

with an eigenvalue with  $|z| = 1$ . In this case  $Z_1^\dagger(k)Z_1(k) = 1$ . We come to a contradiction by considering the following inequality:

$$\psi^\dagger\psi > \psi^\dagger A^\dagger A\psi = \psi^\dagger Z_1^\dagger(k)Z_1(k)\psi = \psi^\dagger\psi \quad (3.63)$$

So we conclude that there are no solutions of  $\det[A - Z_1(k)] = 0$  with  $z$  on the unit circle. Next, we observe that for  $A = 0$  there are exactly  $N_1$  of  $\det[A - Z_1(k)] = 0$  with  $z = 0$  and  $N_1$  solutions with  $z = \infty$ . Since these solutions never cross the unit circle when  $A$  is smoothly deformed, we come to the statement we set to prove.

# Bibliography

- [1] A. Altland and M. R. Zirnbauer, *Phys. Rev. B* **55**, 1142 (1997).
- [2] A. Kitaev, *AIP Conf. Proc.* **1134**, 22 (2009).
- [3] A. P. Schnyder, S. Ryu, A. Furusaki, and A. W. W. Ludwig, *AIP Conf. Proc.* **1134**, 10 (2009).
- [4] T. A. Loring and M. B. Hastings, *Europhys. Lett.* **92**, 67004 (2010).
- [5] Z. Ringel and Y. E. Kraus, *Phys. Rev. B* **83**, 245115 (2011).
- [6] M. B. Hastings and T. A. Loring, *Ann. Phys.* **326**, 1699 (2011).
- [7] I. C. Fulga, F. Hassler, A. R. Akhmerov, and C. W. J. Beenakker, *Phys. Rev. B* **83**, 155429 (2011).
- [8] A. R. Akhmerov, J. P. Dahlhaus, F. Hassler, M. Wimmer, and C. W. J. Beenakker, *Phys. Rev. Lett.* **106**, 057001 (2011).
- [9] M. Wimmer, A. R. Akhmerov, J. P. Dahlhaus, and C. W. J. Beenakker, *New J. Phys.* **13**, 053016 (2011).
- [10] X.-L. Qi, T. L. Hughes, and S.-C. Zhang, *Phys. Rev. B* **78**, 195424 (2008).
- [11] S. Ryu, C. Mudry, H. Obuse, and A. Furusaki, *New J. Phys.* **12**, 065010 (2010).
- [12] D. J. Thouless, M. Kohmoto, M. P. Nightingale, and M. den Nijs, *Phys. Rev. Lett.* **49**, 405 (1982).
- [13] B. I. Halperin, *Phys. Rev. B* **25**, 2185 (1982).

- 
- [14] M. Büttiker, Phys. Rev. B **38**, 9375 (1988).
- [15] R. B. Laughlin, Phys. Rev. B **23**, 5632 (1981).
- [16] M. Büttiker, H. Thomas, and A. Prêtre, Z. Phys. B **94**, 133 (1994).
- [17] P. W. Brouwer, Phys. Rev. B **58**, R10135 (1998).
- [18] G. Bräunlich, G. M. Graf, and G. Ortelli, Commun. Math. Phys. **295**, 243 (2010).
- [19] J. Zak, Phys. Rev. Lett. **62**, 2747 (1989).
- [20] S. Ryu and Y. Hatsugai, Phys. Rev. Lett. **89**, 077002 (2002).
- [21] C. Mahaux and H. A. Weidenmüller, *Shell-Model Approach to Nuclear Reactions* (North-Holland, Amsterdam, 1969).
- [22] M. Stone, C.-K. Chiu, and A. Roy, J. Phys. A: Math. Theor. **44** 045001 (2011).
- [23] J. C. Y. Teo, C. L. Kane, Phys. Rev. B **82**, 115120 (2010).
- [24] A. Y. Kitaev, Phys.-Usp. **44**, 131 (2001).
- [25] X.-L. Qi, T. L. Hughes, and S.-C. Zhang, Phys. Rev. B **81**, 134508 (2010).
- [26] L. Fu and C. L. Kane, Phys. Rev. B **74**, 195312 (2006).
- [27] D. Meidan, T. Micklitz, and P. W. Brouwer, Phys. Rev. B **84**, 075325 (2011).
- [28] D. Meidan, T. Micklitz, and P. W. Brouwer, Phys. Rev. B **84**, 195410 (2011).
- [29] S. Ryu, J. E. Moore, and A. W. W. Ludwig, Phys. Rev. B, **85**, 045104 (2012).
- [30] Z. Wang, X.-L. Qi, and S.-C. Zhang, Phys. Rev. B **84**, 014527 (2011).
- [31] E. Prodan, J. Phys. A: Math. Theor. **44**, 113001 (2011).
- [32] T. A. Loring, A. P. W. Sørensen, arXiv:1107.4187 (2011).
- [33] M. Z. Hassan and C. L. Kane, Rev. Mod. Phys. **82**, 3045 (2010).

- [34] L. Fu, C. L. Kane, and E. J. Mele, *Phys. Rev. Lett.* **98**, 106803 (2007).
- [35] J. E. Moore and L. Balents, *Phys. Rev. B* **75**, 121306 (2007).
- [36] A. P. Schnyder and S. Ryu, *Phys. Rev. B* **84**, 060504 (2011).
- [37] X. Wan, A. M. Turner, A. Vishwanath, and S. Y. Savrasov, *Phys. Rev. B* **83**, 205101 (2011).
- [38] A. George, *SIAM J. Num. Anal.* **10** (2), 345 (1973).
- [39] S. Li, S. Ahmed, G. Klimeck, and E. Darve, *J. Comp. Phys.* **227** (22), 9408 (2008).
- [40] M. Wimmer, *ACM Trans. Math. Softw.* **38**, 30 (2012).
- [41] B. A. Bernevig, T. L. Hughes, and S.-C. Zhang, *Science* **314**, 1757 (2006).
- [42] E. Prodan, *Phys. Rev. B* **83**, 195119 (2011)
- [43] J. T. Chalker and P. D. Coddington, *J. Phys. C* **21**, 2665 (1988).
- [44] S. Cho and M. P. A. Fisher, *Phys. Rev. B* **55**, 1025 (1997).
- [45] S. Ryu, A. P. Schnyder, A. Furusaki, and A. W. W. Ludwig, *New J. Phys.* **12**, 065010 (2010).
- [46] The Supplemental Material at  
'<http://arxiv.org/src/1106.6351v4/anc>' shows movies of this 'fingerprint' in classes A, AII, and DIII.
- [47] H. Zhang, C.-X. Liu, X.-L. Qi, X. Dai, Z. Fang. and S.-C. Zhang, *Nature Physics* **5**, 438 (2009).



## Chapter 4

# Topological quantum number and critical exponent from conductance fluctuations at the quantum Hall plateau transition

### 4.1 Introduction

A two-dimensional electron gas in a strong perpendicular magnetic field has an insulating bulk and a conducting edge. While the conductance  $G_{\text{edge}}$  for transport along the edge is quantized in units of  $e^2/h$ , the conductance  $G_{\text{bulk}}$  for transport between opposite edges is strongly suppressed. This is the regime of the (integer) quantum Hall effect [1]. Upon variation of magnetic field or Fermi energy, a transition occurs in which  $G_{\text{edge}}$  varies from one quantized plateau to the next, accompanied by a peak in  $G_{\text{bulk}}$ .

The quantum Hall plateau transition is not smooth, but exhibits fluctuations reminiscent of the universal conductance fluctuations in metals [2–8]. In small samples the fluctuations take the form of sharp peaks, due to resonant scattering between opposite edges mediated by quasi-bound states in the bulk [9]. In larger samples the intermediate states form a percolating network at the plateau transition, resulting in

a smooth peak in  $G_{\text{bulk}}$  with rapid fluctuations superimposed [10].

The conductance fluctuations are typically analyzed in a context that emphasises their random, sample-specific nature [7]. Here we wish to point out one feature of these fluctuations that has a sample independent *topological* origin.

The quantum Hall plateau transition is a topological phase transition, because a topological quantum number  $Q$  changes from one plateau to the next [11]. We show that a change in  $Q$  is associated with a resonance in the amplitude  $\Delta G$  of the magnetoconductance oscillations in a ring (Corbino) geometry. Each unit increment of  $Q$  corresponds to a resonant amplitude  $\Delta G = e^2/h$  (times spin degeneracies). Our analysis relies on a scattering formula for the topological quantum number, which relates  $Q$  to the winding number of the determinant of the reflection matrix [12, 13].

The analytical considerations in Sec. 4.2 are supported by numerical calculations in Sec. 4.3. These show, in particular, that the plateau transition in a disordered system is reentrant: there are multiple increments of  $Q$ , alternatingly  $+1$  and  $-1$ , each associated with an  $e^2/h$  resonance in  $\Delta G$ . We conclude in Sec. 4.4 by showing that the critical exponent of the phase transition can be extracted from the sample-size dependence of the width of the resonance, in a way which preserves information on which side of the phase transition one is located. The Appendices contain details of the numerical calculations.

## 4.2 Topological quantum number and conductance resonance

To isolate  $G_{\text{bulk}}$  from  $G_{\text{edge}}$  we consider a Corbino geometry, see Fig. 4.1, consisting of a ring-shaped two-dimensional electron gas (2DEG) connected to an electrode at the inner and outer perimeters. The two-terminal conductance  $G = G_{\text{bulk}}$  is then fully due to the current through the bulk,  $I$ , without contributions from the currents circulating along the edges.

We assume that the outer electrode, at a voltage  $V$  relative to the inner electrode, is connected via an  $N$ -mode lead to the 2DEG. (For simplicity we do not include spin as a separate degree of freedom.) The reflection amplitudes  $r_{mn}$  from mode  $n$  to mode  $m$  are contained in the  $N \times N$  reflection matrix  $r$ . The conductance  $G = I/V$  (in units of the



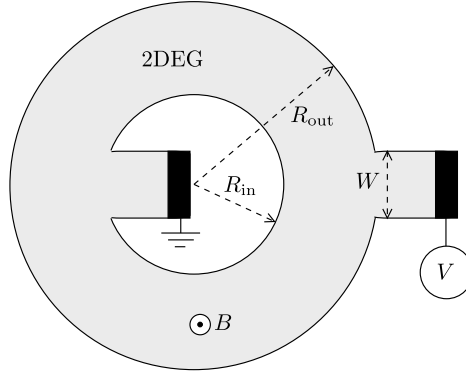


**Figure 4.1.** Corbino geometry consisting of a ring-shaped two-dimensional electron gas (2DEG, grey) in a perpendicular magnetic field  $B$ . A pair of electrodes (black), at a voltage difference  $V$ , is attached to the inner and outer edges of the ring.

conductance quantum  $G_0 = e^2/h$  follows from

$$G = G_0 \text{Tr}(\mathbf{1} - rr^\dagger) = G_0 \sum_n (1 - R_n), \quad (4.1)$$

with  $\mathbf{1}$  the  $N \times N$  unit matrix. The reflection eigenvalues  $R_n \in [0, 1]$  are eigenvalues of the Hermitian matrix product  $rr^\dagger$ . Away from the plateau transition all  $R_n$ 's are close to unity and  $G \ll e^2/h$ .

The topological quantum number  $\mathcal{Q} \in \mathbb{Z}$  of the quantum Hall effect in a translationally invariant system is the Chern number of the bands below the Fermi level [11]. An alternative formulation [12, 13], applicable also to a finite disordered system, obtains  $\mathcal{Q}$  as the winding number of the determinant of the reflection matrix,

$$\mathcal{Q} = \frac{1}{2\pi i} \int_0^{2\pi} d\phi \frac{d}{d\phi} \ln \det r(\phi), \quad (4.2)$$

where  $\Phi \equiv \phi \times \hbar/e$  is the magnetic flux enclosed by the inner perimeter of the ring. To define the winding number one needs to vary  $\phi$  at constant magnetic field in the 2DEG, so that  $r(\phi)$  is  $2\pi$ -periodic. The conductance (4.1) then oscillates periodically as a function of  $\phi$ , with amplitude  $\Delta G$ . (We will examine in the next Section to what extent this applies to the realistic situation of a uniform magnetic field.)

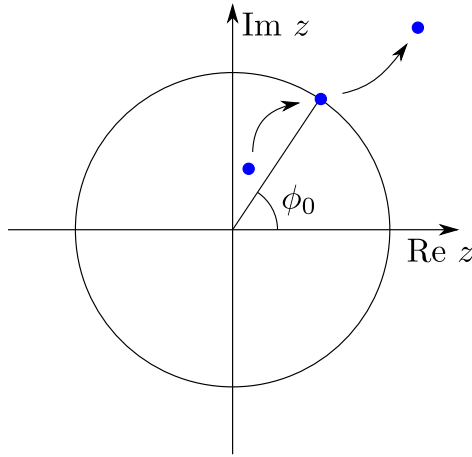


**Figure 4.2.** Example of a path taken in the complex plane  $z = e^{i\phi}$  by a zero (blue dot) of  $\det r$ , as the system is driven through a phase transition in which  $\mathcal{Q} \rightarrow \mathcal{Q} - 1$ . At the transition, the zero crosses the unit circle and a reflection eigenvalue vanishes for some flux  $\phi_0$ . The speed at which the zero crosses the unit circle determines the critical exponent of the quantum Hall phase transition, see Sec. 4.4.

If the  $\phi$ -dependence of  $r$  is continued analytically to arbitrary complex  $z = e^{i\phi}$ , the winding number

$$\mathcal{Q} = n_{\text{zero}} - n_{\text{pole}} \quad (4.3)$$

equals the difference of the number of zeros and poles of  $\det r$  inside the unit circle  $|z| = 1$ . A pole may annihilate a zero, but the difference  $n_{\text{zero}} - n_{\text{pole}}$  can only change when a pole or zero crosses the unit circle. Unitarity of the scattering matrix requires  $|\det r(\phi)| \leq 1$  for real  $\phi$ , so poles cannot cross the unit circle. A topological phase transition, corresponding to a change in  $\mathcal{Q}$ , is therefore signaled by a zero of  $\det r$  crossing the unit circle [13], see Fig. 4.2.

We conclude that at the transition point  $\det r(\phi) = 0$  for some real value of  $\phi$ , which implies that (at least) one of the  $R_n$ 's vanishes. If the zeros are well separated, and all other  $R_n$ 's remain close to unity, the conductance oscillation amplitude  $\Delta G$  would thus show a peak of  $e^2/h$  whenever  $\mathcal{Q}$  changes by  $\pm 1$ . This transport signature of a topological phase transition is the analogue for a 2D system of the 1D signature of Ref. 14.

### 4.3 Numerical simulations in a disordered system

We have searched for the predicted conductance resonances in a numerical simulation. The Corbino disc is discretized on a square lattice (lattice constant  $a$ , nearest-neighbor hopping energy  $t$ ). Electrostatic disorder is introduced as an uncorrelated random on-site potential, drawn uniformly from the interval  $(-\epsilon_0, \epsilon_0)$ . A uniform perpendicular magnetic field  $B$  is introduced by the Peierls substitution, with  $f = Ba^2e/h$  the flux through a unit cell in units of the flux quantum.

Referring to Fig. 4.1 we take parameters  $R_{\text{out}} = 200a$ ,  $R_{\text{in}} = 150a$ ,  $W = 60a$ . For  $f = 0.005$  we have a magnetic length  $l_m = (\hbar/eB)^{1/2} = 5.6a$ , sufficiently small that the edge states at opposite edges do not overlap. These parameter values are representative for a  $\mu\text{m}$ -size GaAs Corbino disc in a field of 5 T. The disorder strength was fixed at  $\epsilon_0 = 0.2t$ .

We calculate the reflection matrix  $r$  at energy  $\mu$  as a function of the flux  $f$  using the recursive Green function technique. This gives the conductance  $G$  via Eq. (4.1). The topological quantum number  $\mathcal{Q}$  is calculated from Eq. (4.3), by locating the zeros and poles of  $\det r$  in the complex flux plane using the method of Ref. 13. (We summarize this method in App. 4.5.1.) Results are shown in Fig. 4.3. Since we are interested in mesoscopic, sample-specific effects, this is data for a single disorder realization, without ensemble averaging.

The left panels show that we can access regions with different topological quantum number by varying flux and Fermi energy. This represents a wide sweep in parameter space, with plateau regions of constant  $\mathcal{Q} = 1, 2, 3, 4, 5$  separated by transition regions of fluctuating  $\mathcal{Q}$ . The conductance  $G$ , which in the Corbino geometry is the bulk conductance, vanishes on the plateau regions and fluctuates in the transition regions.

The right panels zoom in on the  $\mathcal{Q} = 0$  to 1 transition. The conductance oscillations as a function of the flux are only approximately periodic, because the magnetic field changes uniformly (and not just inside the inner perimeter of the ring). Still, a dominant periodicity  $\Delta f = 1.1 \cdot 10^5$  can be extracted, corresponding to an  $h/e$  flux through a disc of radius  $R_{\text{eff}} \approx 170a$ , about halfway between the inner and outer radii of the ring. (For a  $\mu\text{m}$ -size Corbino disc this would correspond to a field scale of  $\Delta B \approx 10\text{mT}$ .)

To search for the predicted signature of the topological phase transition, we calculate the amplitude  $\Delta G = G_{\text{max}} - G_{\text{min}}$  of the conductance

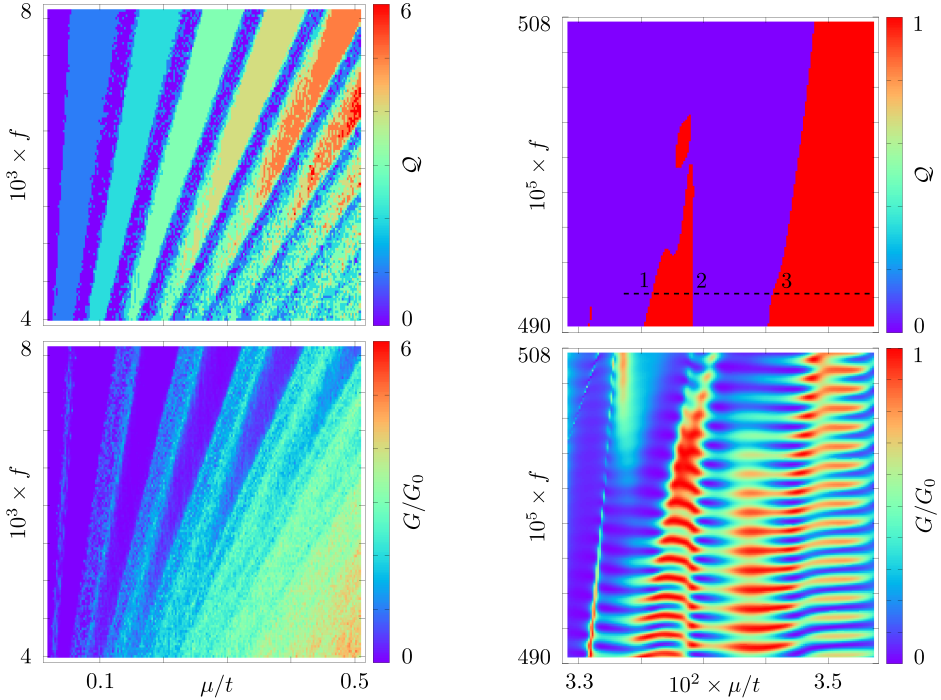


**Figure 4.3.** Topological quantum number (top panels) and conductance (bottom panels) of a disordered 2DEG in the Corbino disk geometry. The left panels give a broad range of flux  $f$  and Fermi energy  $\mu$ , while the right panels show a close-up of the  $\mathcal{Q} = 0 \rightarrow 1$  transition. (Note the different color scales for the left and right panels.) The horizontal dashed line indicates the three reentrant phase transitions (see Fig. 4.7).

oscillations over one period ( $f, f + \Delta f$ ). This amplitude is plotted in Fig. 4.4 as a function of Fermi energy, for different fluxes  $f$ . The  $\mathcal{Q} = 0 \rightarrow 1$  transition should give at least one  $e^2/h$  peak value of  $\Delta G$ , which is indeed what is observed. For the larger field values there is only a single  $e^2/h$  peak, while for the lower field values three peaks develop, consistent with the  $\mathcal{Q} = 0 \rightarrow 1 \rightarrow 0 \rightarrow 1$  reentrant transition seen in Fig. 4.3 (upper right panel, dashed line).

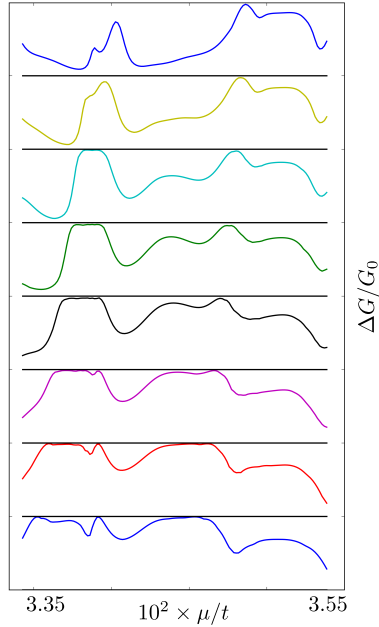


**Figure 4.4.** Dependence of the amplitude of the magnetoconductance oscillations on the Fermi energy for different magnetic fields. The  $n$ -th trace from the bottom shows the  $\mu$ -dependence of  $\Delta G = G_{\max} - G_{\min}$  in the flux interval  $(f_n, f_n + \Delta f)$ , with  $f_n = 490 \cdot 10^{-5} + 2(n-1)\Delta f$  and  $\Delta f = 1.1 \cdot 10^5$ . Successive traces are displaced vertically, with the  $G_0 = e^2/h$  peak value indicated by a horizontal black line.

## 4.4 Discussion and relation to the critical exponent

We have shown that the sample-specific conductance fluctuations at the quantum Hall plateau transition contain a universal feature of a topological origin: The magnetoconductance oscillations in a Corbino disc geometry have an  $e^2/h$  resonant amplitude whenever the topological quantum number  $Q$  is incremented by  $\pm 1$ . The strict  $h/e$  flux periodicity of the magnetoconductance is broken in a realistic setting by the penetration of the flux through the conducting region, but we have shown by numerical simulations that the resonances are still clearly observable.

The theory presented here may motivate an experimental search for the reentrant phase transition that we observed in our simulations. Existing experiments [7] in a GaAs Corbino disc show a maximal amplitude of about  $0.1 e^2/h$  in the  $Q = 1 \rightarrow 2$  plateau transition, an order

of magnitude below the predicted value. This may partly be due to limited phase coherence, and partly to the self-averaging effect of overlapping resonances. In the experimental geometry the entire inner and outer perimeters of the Corbino disc are contacted to current source and drain, while our geometry (Fig. 4.1) has two narrow contacts — which helps to isolate the resonances and make them more easily observable.

From a theoretical perspective, the evolution of zeros of the reflection matrix determinant, see Figs. 4.2 and 4.7, provides a new way to analyse the plateau transition in a disordered mesoscopic system. In particular, the critical exponent  $\nu$  of the quantum Hall phase transition can be extracted from the speed at which a zero  $z_0$  of  $\det r(z)$  crosses the unit circle in the complex flux plane,

$$\lim_{L \rightarrow \infty} \frac{W}{L} \ln |z_0| = \text{const} \times (\mu - \mu_c) W^{1/\nu} + \mathcal{O}(\mu - \mu_c)^2. \quad (4.4)$$

Here  $\mu_c$  is the value of the Fermi energy  $\mu$  at the phase transition, where  $z_0 = e^{i\phi}$  for some real flux  $\phi$ . The Corbino disc has inner perimeter of radius  $L$  and outer perimeter of radius  $L + W$ , with the limit  $L \rightarrow \infty$  taken at constant  $W$ .

We note the following conceptual difference with the usual MacKinnon-Kramer scaling [15, 16]: The MacKinnon-Kramer scaling variable is a Lyapunov exponent, which is a nonnegative quantity. Our scaling variable  $\ln |z_0|$  changes sign at the phase transition, so it contains information on which side of the transition one is located.

In App. 4.5.2 we present a calculation of the critical exponent along these lines. It remains to be seen whether this alternative numerical method has advantages over the conventional method based on MacKinnon-Kramer scaling. It is also still an open question whether the evolution of the zeros of  $\det r$  is more accessible to analytical methods than the evolution of Lyapunov exponents.

## 4.5 Appendix

### 4.5.1 Calculation of the topological quantum number

We summarize the method used to calculate the topological quantum number  $\mathcal{Q}$  of the Corbino disc, following Ref. 13. We insert a flux tube  $\Phi = \phi\hbar/e$  at the center, without changing the magnetic field in the

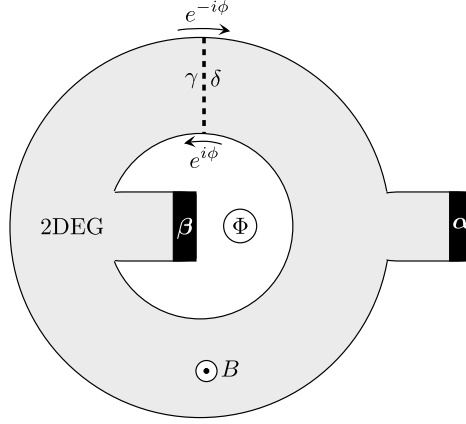


**Figure 4.5.** Corbino disc in a uniform magnetic field  $B$ , containing additionally a flux tube  $\Phi$  inside the inner perimeter. We choose a gauge such that the phase increment  $\phi = e\Phi/\hbar$  due to the flux tube is accumulated upon crossing a cut indicated by the dashed line. Virtual leads  $\gamma, \delta$  are attached at the two sides of the cut. Together with the two physical leads  $\alpha, \beta$  they define the four-terminal scattering matrix (4.5). The reflection matrix  $r$  of the original two-terminal system is obtained from Eq. (4.6), in a formulation which can be analytically continued to arbitrary complex  $z = e^{i\phi}$ .

2DEG, and obtain  $\mathcal{Q}$  as the winding number of  $\det r$ . The integration (4.2) over  $\phi$  can be avoided by going to the complex  $z = e^{i\phi}$  plane and counting the number of zeros and poles of  $\det r$  in the unit circle. The difference  $n_{\text{zero}} - n_{\text{pole}}$  then directly gives  $\mathcal{Q}$ .

### Analytic continuation to complex flux

To perform the analytic continuation to complex flux we cut the disc as indicated in Fig. 4.5. We attach virtual leads (see Fig. 4.6) at the two sides of the cut and construct the four-terminal unitary scattering matrix

$$S = \begin{pmatrix} r_{\alpha\alpha} & t_{\alpha\beta} & t_{\alpha\gamma} & t_{\alpha\delta} \\ t_{\beta\alpha} & r_{\beta\beta} & t_{\beta\gamma} & t_{\beta\delta} \\ t_{\gamma\alpha} & t_{\gamma\beta} & r_{\gamma\gamma} & t_{\gamma\delta} \\ t_{\delta\alpha} & t_{\delta\beta} & t_{\delta\gamma} & r_{\delta\delta} \end{pmatrix}. \quad (4.5)$$

We choose a gauge such that the entire phase increment  $\phi$  from the flux tube is accumulated at the cut, between terminals  $\gamma$  and  $\delta$ . The reflection

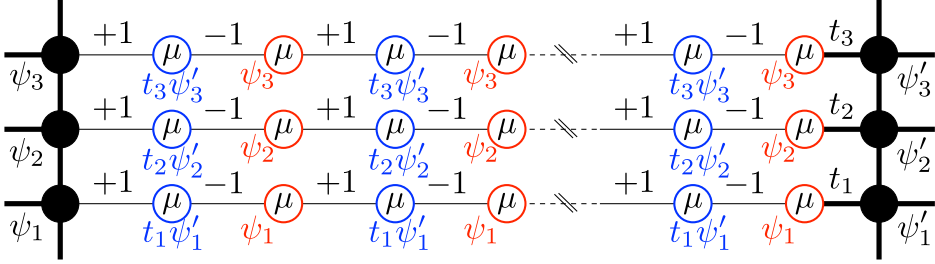


**Figure 4.6.** Construction of a virtual lead, connecting two sides of a tight-binding lattice. The virtual lead consists of parallel 1D chains with on-site energy  $\mu$  and hopping amplitudes alternating between  $+1$  and  $-1$ . The tight-binding equations enforce that every other site in the chain (colored red or blue) has the same wave amplitude at energy  $\mu$ . The wave amplitudes  $\psi_n, \psi'_n$  at the left and right end of the  $n$ -th chain are therefore unaffected by the insertion of the virtual lead. We use this device in Fig. 4.5 to convert a two-terminal geometry into a four-terminal geometry, by cutting the lead at the center and connecting the ends to terminals  $\gamma, \delta$ .

matrix  $r$  of the original two-terminal system (from terminal  $\alpha$  back to  $\alpha$ ) is then obtained from

$$r = r_{\alpha\alpha} - (t_{\alpha\gamma} \ t_{\alpha\delta}) \begin{pmatrix} r_{\gamma\gamma} & t_{\gamma\delta} - z \\ t_{\delta\gamma} - 1/z & r_{\delta\delta} \end{pmatrix}^{-1} \begin{pmatrix} t_{\gamma\alpha} \\ t_{\delta\alpha} \end{pmatrix}. \quad (4.6)$$

This expression is in a form suitable for analytic continuation to arbitrary complex  $z = e^{i\phi}$ .

### Evolution of zeros and poles of $\det r$

The determinant of the reflection matrix (4.6) is computed as a function of the complex variable  $z$  by means of the relation

$$\det(D - CA^{-1}B) = \det \begin{pmatrix} A & B \\ C & D \end{pmatrix} [\det A]^{-1}. \quad (4.7)$$

This results in the expression

$$\det r = \det \begin{pmatrix} r_{\gamma\gamma} & t_{\gamma\delta} - z & t_{\gamma\alpha} \\ t_{\delta\gamma} - 1/z & r_{\delta\delta} & t_{\delta\alpha} \\ t_{\alpha\gamma} & t_{\alpha\delta} & r_{\alpha\alpha} \end{pmatrix} \times \left[ \det \begin{pmatrix} r_{\gamma\gamma} & t_{\gamma\delta} - z \\ t_{\delta\gamma} - 1/z & r_{\delta\delta} \end{pmatrix} \right]^{-1}. \quad (4.8)$$



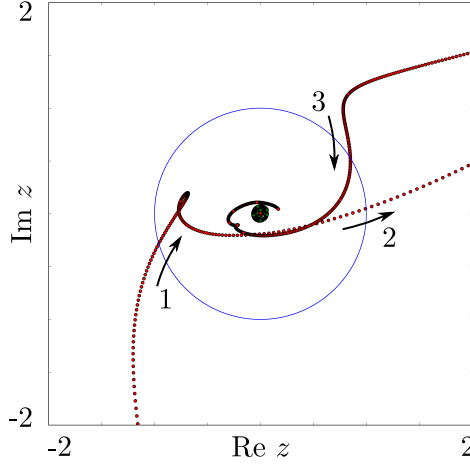


**Figure 4.7.** Positions of the zeros (red) and poles (green, clustered near the origin) of  $\det r$ , along the path indicated by the dashed line in Fig. 4.3. Arrows point in the direction of increasing Fermi energy. The numbers 1,2,3 indicate the three phase transitions in which the topological quantum number  $\mathcal{Q}$  changes first from 0 to 1, then from 1 back to 0, and once again from 0 to 1.

The zeros and poles of  $\det r$  are therefore those values of  $z$  for which, respectively, the determinant in the numerator or denominator of Eq. (4.8) vanishes. By equating each of these determinants to zero we obtain two generalized eigenvalue problems, with the zeros given by

$$\begin{pmatrix} r_{\gamma\gamma} & t_{\gamma\delta} & t_{\gamma\alpha} \\ -1 & 0 & 0 \\ t_{\alpha\gamma} & t_{\alpha\delta} & r_{\alpha\alpha} \end{pmatrix} \begin{pmatrix} \psi_1 \\ \psi_2 \\ \psi_3 \end{pmatrix} = -z \begin{pmatrix} 0 & -1 & 0 \\ t_{\delta\gamma} & r_{\delta\delta} & t_{\delta\alpha} \\ 0 & 0 & 0 \end{pmatrix} \begin{pmatrix} \psi_1 \\ \psi_2 \\ \psi_3 \end{pmatrix}, \quad (4.9)$$

and the poles by

$$\begin{pmatrix} r_{\gamma\gamma} & t_{\gamma\delta} \\ -1 & 0 \end{pmatrix} \begin{pmatrix} \psi_1 \\ \psi_2 \end{pmatrix} = z \begin{pmatrix} 0 & 1 \\ -t_{\delta\gamma} & -r_{\delta\delta} \end{pmatrix} \begin{pmatrix} \psi_1 \\ \psi_2 \end{pmatrix}. \quad (4.10)$$

The numerical solution of generalized eigenvalue problems is quick and accurate. As an example, we show in Fig. 4.7 the motion of the zeros and poles along the reentrant phase transition of Fig. 4.3.

## 4.5.2 Calculation of the critical exponent

In Sec. 4.4 we outlined how the critical exponent of the quantum Hall phase transition can be extracted from the speed at which a zero  $z_0$  of

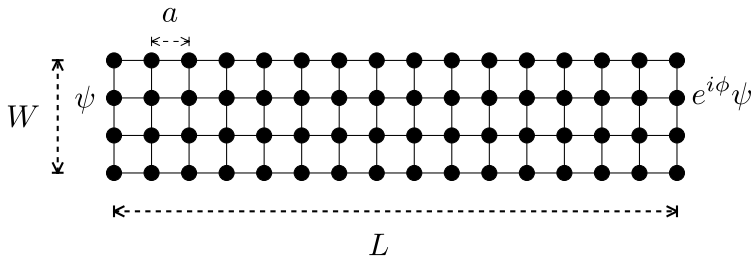


**Figure 4.8.** Geometry of the network model used to calculate the critical exponent. This rolled up strip is topologically equivalent to the Corbino geometry used in the main text.

$\det r(z)$  crosses the unit circle in the complex  $z = e^{i\phi}$  plane. Here we demonstrate that this approach produces results consistent with earlier calculations based on the scaling of Lyapunov exponents [16].

To make contact with those earlier calculations, we use the same Chalker-Coddington network model [17, 18] (rather than the tight-binding model used in the main text). The parameter that controls the plateau transition in the network model is the mixing angle  $\alpha$  of the scattering phase shifts at the nodes of the network. The transition is at  $\alpha_c = \pi/4$ . Disorder is introduced by means of random, uncorrelated phase shifts on the links between nodes, sampled uniformly from  $[0, 2\pi)$ .

The network has a strip geometry, of longitudinal dimension  $L$  and transverse dimension  $W$  (see Fig. 4.8). The longitudinal dimension has twisted boundary conditions,  $\psi \mapsto e^{i\phi}\psi$  upon translation over  $L$ . The transverse dimension is connected to a source and drain reservoir. This geometry is equivalent to a Corbino disc, enclosing a flux  $\Phi = \phi\hbar/e$  and with source and drain contacts extending along the entire inner and outer perimeter.

Taking the self-averaging limit  $L \rightarrow \infty$  of Eq. (4.4) is impractical, but sufficient convergence is reached for an aspect ratio  $L/W = 5$  and an average of  $\ln |z_0|$  over 1000 disorder realizations. Results for the  $W$  and  $\alpha$ -dependence of the scaling parameter  $\Lambda = (W/L)\langle \ln |z_0| \rangle$  are shown in Fig. 4.9.

We extract the critical exponent  $\nu$  using the procedure of Ref. 16, by

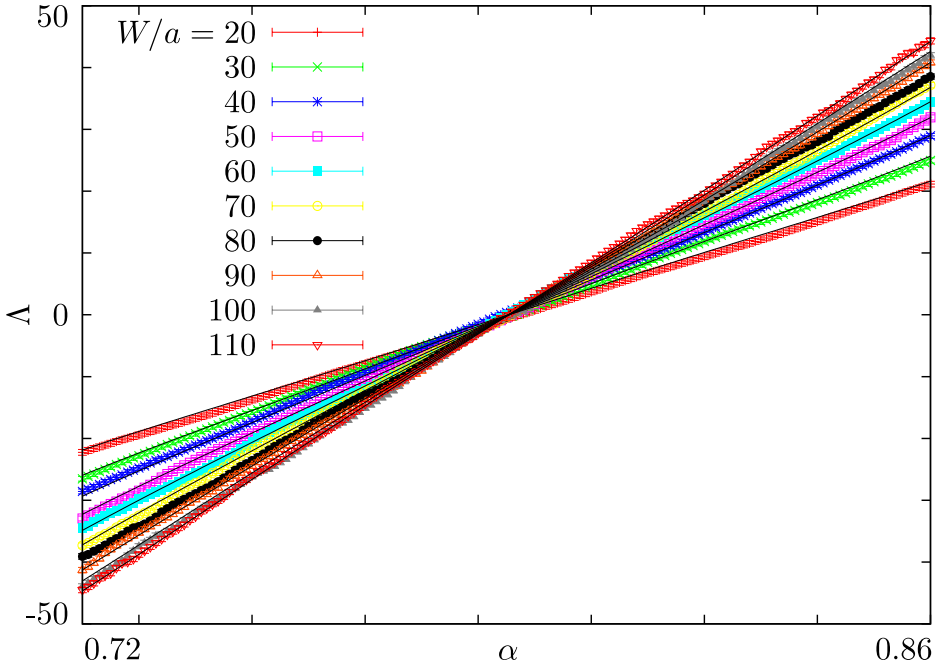


**Figure 4.9.** Scaling variable as obtained numerically (data points) and as fitted to Eq. (4.11) (black lines).

fitting the data to the scaling law

$$\Lambda(W, \alpha) = \sum_{p=1}^n c_p W^{p/\nu} \left[ \sum_{q=1}^{n'} c'_q (\alpha - \alpha_c)^q \right]^p. \quad (4.11)$$

We have checked that corrections to scaling are insignificant in our parameter range. The symmetry of the network model (a time-reversal operation followed by translation over half a unit cell) implies that only odd powers of  $\alpha - \alpha_c$  appear in the series expansion ( $c_p = c'_p = 0$  for  $p$  even). We truncated the expansions such as to keep terms of order  $(\alpha - \alpha_c)^5$  and lower. The result  $\nu = 2.56 \pm 0.03$  is consistent with the value  $\nu = 2.59$  obtained in Ref. 16.



# Bibliography

- [1] *The Quantum Hall Effect*, edited by R. E. Prange and S. M. Girvin (Springer, 1986).
- [2] J. A. Simmons, S. W. Hwang, D. C. Tsui, H. P. Wei, L. W. Engel, and M. Shayegan, *Phys. Rev. B* **44**, 12933 (1991).
- [3] P. C. Main, A. K. Geim, H. A. Carmona, C. V. Brown, T. J. Foster, R. Taboryski, and P. E. Lindelof, *Phys. Rev. B* **50**, 4450 (1994).
- [4] A. A. Bykov, Z. D. Kvon, E. B. Ol'shanetskii, L. V. Litvin, and S. P. Moshchenko, *Phys. Rev. B* **54**, 4464 (1996).
- [5] D. H. Cobden and E. Kogan, *Phys. Rev. B* **54**, R17316 (1996).
- [6] T. Machida, S. Ishizuka, S. Komiyama, K. Muraki, and Y. Hirayama, *Phys. Rev. B* **63**, 045318 (2001).
- [7] F. Hohls, U. Zeitler, and R. J. Haug, *Phys. Rev. B* **66**, 073304 (2002).
- [8] E. Peled, D. Shahar, Y. Chen, E. Diez, D. L. Sivco, and A. Y. Cho, *Phys. Rev. Lett.* **91**, 236802 (2003).
- [9] J. K. Jain and S. A. Kivelson, *Phys. Rev. Lett.* **60**, 1542 (1988).
- [10] N. R. Cooper, B. I. Halperin, C.-K. Hu, and I. M. Ruzin, *Phys. Rev. B* **55**, 4551 (1997).
- [11] D. J. Thouless, M. Kohmoto, M. P. Nightingale, and M. den Nijs, *Phys. Rev. Lett.* **49**, 405 (1982).
- [12] G. Bräunlich, G. M. Graf, and G. Ortelli, *Comm. Math. Phys.* **295**, 1 (2009).

- [13] I. C. Fulga, F. Hassler, and A. R. Akhmerov, *Phys. Rev. B* **85**, 165409 (2012).
- [14] A. R. Akhmerov, J. P. Dahlhaus, F. Hassler, M. Wimmer, and C. W. J. Beenakker, *Phys. Rev. Lett.* **106**, 057001 (2011).
- [15] A. MacKinnon and B. Kramer, *Phys. Rev. Lett.* **47**, 1546 (1981).
- [16] K. Slevin, T. Ohtsuki, *Phys. Rev. B* **80**, 041304 (2009).
- [17] J. T. Chalker and P. D. Coddington, *J. Phys. C* **21**, 2665 (1988).
- [18] B. Kramer, T. Ohtsuki, and S. Kettemann, *Phys. Rep.* **417**, 211 (2005).

## Chapter 5

# Thermal metal-insulator transition in a helical topological superconductor

### 5.1 Introduction

Gapped electronic systems are topological states of matter, subject to phase transitions in which a topological invariant  $Q$  changes its value [1]. For noninteracting electrons in two spatial dimensions,  $Q \in \mathbb{Z}$  is integer valued in the absence of time-reversal symmetry, and  $Q \in \mathbb{Z}_2$  is binary in its presence. Two familiar examples from semiconductor physics are quantum Hall (QH) insulators in a strong magnetic field and quantum spin-Hall (QSH) insulators in zero magnetic field [2, 3]. The topological invariant  $Q$  determines the number of electrically conducting edge states, which changes by  $\pm 1$  at a topological phase transition. The edge states are chiral (unidirectional) in the QH effect and helical (counterpropagating) in the QSH effect.

Superconductors can also have an excitation gap, with topologically protected edge states in two dimensions. The edge states carry heat but no charge, so superconducting analogues of the quantum (spin)-Hall effect refer to the thermal rather than the electrical conductance. The thermal quantum Hall effect ( $Q \in \mathbb{Z}$ ) appears in the absence of time-reversal symmetry, for example, in a single layer of a chiral  $p$ -wave superconductor [4–7]. Time-reversal symmetry is restored in two layers of opposite chirality  $p_x \pm ip_y$ , producing the thermal analogue of the

quantum-spin Hall effect ( $\mathcal{Q} \in \mathbb{Z}_2$ ) [8–11]. The edge states in both effects are Majorana fermions, chiral for the thermal QH effect and helical for the thermal QSH effect.

There is a large literature on topological phase transitions in QH and QSH insulators, as well as in chiral superconductors [12], but the thermal QSH effect in helical superconductors has remained largely unexplored. This is symmetry class DIII, characterized by the absence of spin-rotation symmetry and the presence of both time-reversal and electron-hole symmetry. Here we present a study of the phase diagram and critical behavior in helical superconductors. We use a network model in symmetry class DIII for a numerically efficient approach.

We find that the main qualitative effect of time-reversal symmetry is that the transition between two topologically distinct thermal insulators goes via a thermal metal phase, for finite but arbitrarily weak disorder. In contrast, without time-reversal symmetry (in class D) the value of  $\mathcal{Q}$  changes directly without an intermediate metallic phase for weak disorder. For strong disorder both chiral and helical superconductors have a thermal metal-insulator transition, but the critical behavior is different: We find a localization length exponent  $\nu \approx 2.0$ , about twice as large as the known value for chiral  $p$ -wave superconductors [13].

The outline of this paper is as follows. To put our results for helical superconductors in the proper context, in the next section we first summarize known results for chiral  $p$ -wave superconductors. In Sec. 5.3 we introduce the network model of a helical superconductor, constructed out of two coupled chiral networks [14]. To identify topologically distinct phases we apply a scattering formulation of the topological quantum number [15], as described in Sec. 5.4. In Sec. 5.5 we then present the results of our investigation: the phase diagram with the thermal metal-insulator transition, the scaling of the thermal conductivity at the transition, and the critical exponent for the diverging localization length. We conclude in Sec. 5.6.

## 5.2 Chiral versus helical topological superconductors

According to the Altland-Zirnbauer classification [16], superconductors without spin-rotation symmetry are in class D or DIII depending on whether time-reversal symmetry is broken or not. In two dimensions



both symmetry classes can be in thermally insulating phases which are topologically distinct (with or without edge states). In this section we summarize what is known for the phase diagram in class D, before turning to the effects of time-reversal symmetry in class DIII.

A simple model Hamiltonian in class D represents a chiral  $p$ -wave superconductor in the  $x$ - $y$  plane,

$$H_D = v_\Delta(p_x\tau_x + p_y\tau_y) + \left(\frac{p^2}{2m} + U - \mu\right)\tau_z. \quad (5.1)$$

The Pauli matrices  $\tau_i$  (with  $\tau_0$  the  $2 \times 2$  unit matrix) operate on the electron-hole degree of freedom, coupled by the pair potential  $v_\Delta(p_x \pm ip_y)$ . The Fermi energy is  $\mu$  and  $U(x, y)$  describes a random disorder potential (zero average).

By adding a spin degree of freedom (with Pauli matrices  $\sigma_i$  and unit matrix  $\sigma_0$ ), one can extend  $H_D$  to the Hamiltonian of a helical superconductor in class DIII,

$$H_{\text{DIII}} = v_\Delta(p_x\tau_x\sigma_z + p_y\tau_y\sigma_0) + \left(\frac{p^2}{2m} + U - \mu\right)\tau_z\sigma_0 + K\tau_y\sigma_y. \quad (5.2)$$

Both Hamiltonians have electron-hole symmetry,  $\tau_x H^* \tau_x = -H$ , but only the Hamiltonian (5.2) has time-reversal symmetry,  $\sigma_y H_{\text{DIII}}^* \sigma_y = H_{\text{DIII}}$ . The term  $K\tau_y\sigma_y$  in  $H_{\text{DIII}}$  couples the two spin directions to zeroth order in momentum. Higher-order terms, such as  $p\tau_z\sigma_y$ , can be included as well.

The phase diagram of the chiral  $p$ -wave superconductor was calculated for a lattice model in Ref. 13, by discretizing the Hamiltonian (5.1) on a lattice. A similar phase diagram was obtained earlier [18–20] for a class-D network model (Cho-Fisher model) [14]. As shown in Fig. 5.1, there are two insulating phases plus a metallic phase at strong disorder. The two insulating phases are topologically distinct, one is with and the other without chiral edge states. The disorder-induced thermal metal (Majorana metal) arises because of resonant transmission through zero modes (Majorana fermions), pinned to potential fluctuations where  $U$  changes sign [21–23].

The I-I phase boundary separating the two insulating phases and M-I phase boundary separating insulating and metallic phases meet at a tricritical point. In the insulating phases the thermal conductivity decays exponentially  $\propto e^{-L/\xi}$  with system size  $L$ . The localization length  $\xi$

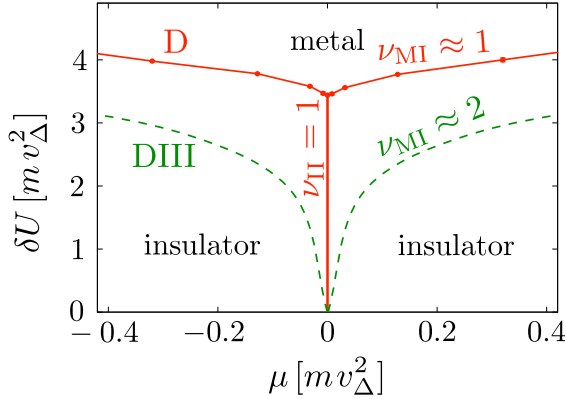


**Figure 5.1.** Solid curves (red): Phase boundaries of a chiral  $p$ -wave superconductor, symmetry class D, calculated in Ref. 13 from a lattice model based on the Hamiltonian (5.1) [17]. The system is a thermal metal (Majorana metal) for strong disorder and a thermal insulator for weak disorder. The dashed (green) lines show qualitatively the effect of time-reversal symmetry in class DIII: the transition between two topologically distinct insulators then goes via an intervening metallic phase. The critical exponents for the various phase transitions are indicated: the value for  $\nu_{II}$  is exact [24], the values for  $\nu_{MI}$  in class D (red, from Ref. 13) and in class DIII (green, from this work) are numerical estimates.

diverges  $\propto |\mu - \mu_c|^{-\nu}$  on approaching a phase boundary at  $\mu = \mu_c$ . The critical exponent on the I-I phase boundary (at  $\mu_c = 0$ ) is known analytically [12, 24],  $\nu_{II} = 1$ . The numerically obtained value [13]  $\nu_{MI} = 1.02 \pm 0.06$  on the M-I phase boundary is very close to  $\nu_{II}$ . Indeed, one would expect [25]  $\nu_{MI} = \nu_{II}$  if the phase boundaries at the tricritical point meet at nonzero angle, which they seem to do.

So much for a summary of known results for chiral superconductors in class D, without time-reversal symmetry. The time-reversally symmetric Hamiltonian  $H_{DIII}$  in (5.2) is just two uncoupled copies of  $H_D$  if  $K = 0$ . Upon increasing the coupling strength  $K$ , the time-reversal symmetry starts to qualitatively modify the phase diagram. As we will show in what follows (as is indicated schematically in Fig. 5.1), a metallic phase develops in between the two insulating phases at weak disorder for  $K \neq 0$ .

## 5.3 Class DIII network model

For numerical efficiency we use a network representation of the class DIII Hamiltonian (5.2). Network models [26] exist for quantum (spin)-Hall insulators [27, 28] and for chiral superconductors [14, 29]. A network model for helical superconductors was still missing and is provided here.

### 5.3.1 Construction

The network is defined on a two-dimensional bipartite square lattice, see Fig. 5.2. Helical Majorana modes propagate along the bonds and are scattered at the nodes. The helicity of the modes signifies that the direction of motion is tied to the spin degree of freedom,  $\uparrow$  and  $\downarrow$ , represented by dashed and solid lines in the figure. The modes encircle local maxima and minima of the electrostatic potential (indicated by  $\pm$  in the figure), in a clockwise or counterclockwise direction depending on the spin. The Majorana character of the modes signifies that there is no separate electron or hole mode, but one single charge-neutral mode per spin direction.

The nodes of the lattice are saddle points between the local potential maxima and minima, alternating between adjacent plaquettes in a checkerboard pattern. Scattering at the nodes is described by  $4 \times 4$  unitary scattering matrices  $S$  and  $S'$  that alternate between adjacent nodes (black and white dots in the figure). The amplitudes  $a_{n\sigma}, b_{n\sigma}$  of incoming and outgoing modes are related by

$$\begin{pmatrix} b_{1\downarrow} \\ b_{2\uparrow} \\ b_{4\uparrow} \\ b_{3\downarrow} \end{pmatrix} = S \begin{pmatrix} a_{1\uparrow} \\ a_{2\downarrow} \\ a_{4\downarrow} \\ a_{3\uparrow} \end{pmatrix}, \quad \begin{pmatrix} b_{1\uparrow} \\ b_{2\downarrow} \\ b_{4\downarrow} \\ b_{3\uparrow} \end{pmatrix} = S' \begin{pmatrix} a_{1\downarrow} \\ a_{2\uparrow} \\ a_{4\uparrow} \\ a_{3\downarrow} \end{pmatrix}. \quad (5.3)$$

(The labels  $\sigma = \uparrow, \downarrow$  and  $n = 1, 2, 3, 4$  refer to Fig. 5.2.)

A class DIII scattering matrix  $S$  at zero excitation energy is constrained by both particle-hole symmetry and time-reversal symmetry. In the basis (5.3) (which relates time-reversed Majorana modes) the unitarity and symmetry constraints read [30]

$$S = S^* = -S^T, \quad S^2 = -1, \quad (5.4)$$

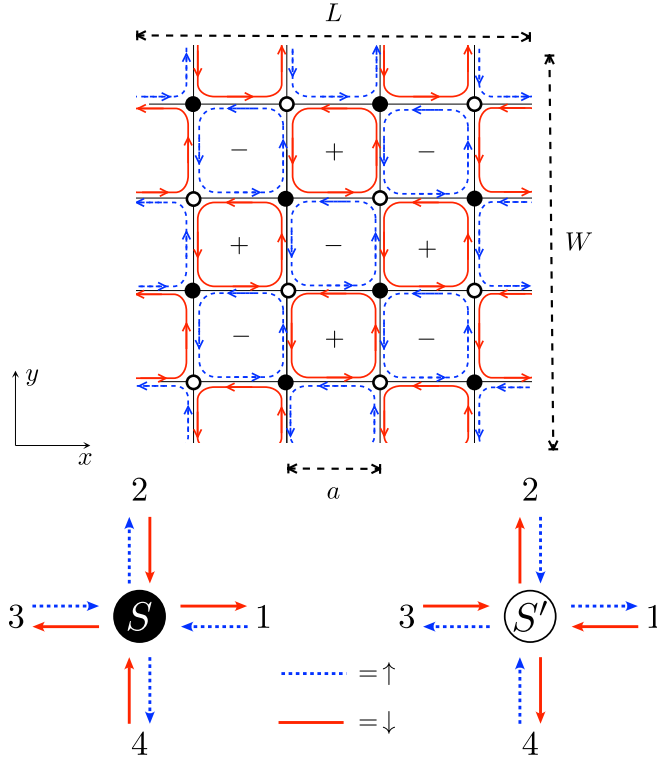


**Figure 5.2.** Illustration of the network model described in the text.

so the scattering matrix is real orthogonal and antisymmetric. (The superscript  $T$  indicates the transpose.)

The most general parameterization contains two real angles  $\alpha, \vartheta \in (0, 2\pi)$  and one  $\mathbb{Z}_2$  index  $\eta \in \{+1, -1\}$  [31],

$$S = \begin{pmatrix} A \cos \alpha & -O^T \sin \alpha \\ O \sin \alpha & -\eta A \cos \alpha \end{pmatrix}, \quad (5.5)$$

$$O = \begin{pmatrix} -\cos \vartheta & -\eta \sin \vartheta \\ \sin \vartheta & -\eta \cos \vartheta \end{pmatrix}, \quad A = \begin{pmatrix} 0 & 1 \\ -1 & 0 \end{pmatrix}. \quad (5.6)$$

The corresponding parameterization for  $S'$  is obtained upon a permuta-

tion of the basis states,

$$S' = PSP^T, \text{ with } P = \begin{pmatrix} 0 & 1 & 0 & 0 \\ 0 & 0 & 0 & 1 \\ 1 & 0 & 0 & 0 \\ 0 & 0 & 1 & 0 \end{pmatrix}, \quad (5.7)$$

which amounts to a  $90^\circ$  rotation.

The angle  $\alpha$  characterizes the scattering at a node for each of the two spin directions separately, while the angle  $\vartheta$  couples them. For  $\vartheta = 0$  we have two independent, time-reversed, copies of the Cho-Fisher model [14], representing a pair of uncoupled chiral superconductors of opposite chirality. The orthogonal matrix  $O$  couples the two copies and produces a network model for a helical superconductor, in much the same way that Obuse et al [28], obtained a network model for a quantum spin-Hall insulator by coupling a pair of Chalker-Coddington models [27] for quantum Hall insulators in opposite magnetic fields.

### 5.3.2 Vortices

One difference between the superconducting network model considered here and the insulating model of Ref. 28, is that here the coupling of time-reversed networks is via real orthogonal rather than complex unitary matrices. This difference expresses the Majorana character of the modes, which have real rather than complex wave amplitudes. Another difference is the appearance of the  $\mathbb{Z}_2$  index  $\eta$ , which determines the parity of the number of (time-reversally invariant) vortices in a plaquette.

To see this, we take  $\alpha = 0$  or  $\alpha = \pi$ , when the network consists of isolated plaquettes. Denoting the value of  $\eta$  for  $S$  and  $S'$  by  $\eta_S$  and  $\eta_{S'}$ , the phase factor acquired by the Majorana mode as it encircles a plaquette is  $\eta_S \eta_{S'}$ . A bound state at zero excitation energy (doubly degenerate because of time-reversal symmetry) results if  $\eta_S \eta_{S'} = 1$ . Since such Majorana zero-modes come in pairs, and each time-reversally invariant vortex in a helical superconductor traps one (doubly-degenerate) zero mode [32], we conclude that the Majorana mode encircles an odd number of vortices for  $\eta_S \eta_{S'} = 1$ .

In what follows we will assume that the system contains no vortices at all in the absence of disorder, so we choose  $\eta_S = 1$ ,  $\eta_{S'} = -1$ . The

scattering matrices then take the form

$$S = \begin{pmatrix} 0 & r & t \cos \vartheta & -t \sin \vartheta \\ -r & 0 & t \sin \vartheta & t \cos \vartheta \\ -t \cos \vartheta & -t \sin \vartheta & 0 & -r \\ t \sin \vartheta & -t \cos \vartheta & r & 0 \end{pmatrix}, \quad (5.8a)$$

$$S' = \begin{pmatrix} 0 & -t \cos \vartheta & -r & -t \sin \vartheta \\ t \cos \vartheta & 0 & t \sin \vartheta & -r \\ r & -t \sin \vartheta & 0 & t \cos \vartheta \\ t \sin \vartheta & r & -t \cos \vartheta & 0 \end{pmatrix}, \quad (5.8b)$$

where we have abbreviated  $r = \cos \alpha$ ,  $t = \sin \alpha$ .

### 5.3.3 Vortex disorder

Disorder is introduced in the network model by varying the scattering parameters in a random way from one node to the other. We choose to keep the coupling strength  $\vartheta$  the same for each node and to vary  $\alpha$ . Following the same procedure as for the Cho-Fisher model [18], we draw  $\alpha_i$  at each node  $i$  independently from a distribution  $P(\alpha_i)$  given by

$$P(\alpha_i) = (1 - q)\delta(\alpha_i - \alpha) + \frac{1}{2}q\delta(\alpha_i + \alpha) + \frac{1}{2}q\delta(\alpha_i + \alpha - \pi). \quad (5.9)$$

The parameter  $q \in [0, 1]$  plays the role of disorder strength.

This is a form of vortex disorder [18]: with probability  $q$  two time-reversally invariant vortices are inserted in the plaquettes adjacent to the  $i$ -th node, one vortex in one plaquette and another one in the diagonally opposite plaquette. The diagonally opposite plaquettes are themselves chosen with equal probability  $1/2$  from the two  $\pm$  sublattices in Fig. 5.2.

We use vortex disorder instead of purely electrostatic disorder [as in the Hamiltonians (5.1) and (5.2)], because it scatters more effectively and allows us to localize wave functions in smaller systems. Both forms of disorder can produce Majorana zero-modes [21, 33], so we do not expect qualitatively different features.

## 5.4 Topological quantum number and thermal conductance

A class DIII topological superconductor in two dimensions has a  $\mathbb{Z}_2$  topological quantum number  $\mathcal{Q} = \pm 1$ . Formulas for  $\mathcal{Q}$  exist based on

the Hamiltonian [35] or on the scattering matrix [15]. Since the network model is described in terms of a scattering matrix, we use the latter formulation.

We consider a rectangular geometry in the  $x$ - $y$  plane, of length  $L = \mathcal{N}'a$  in the  $x$ -direction and width  $W = \mathcal{N}a$  in the  $y$ -direction, where  $a$  is the lattice constant and  $\mathcal{N}, \mathcal{N}'$  are even integers (see Fig. 5.2). In the transverse direction we impose either periodic boundary conditions,  $\psi(x,0) = \psi(x,W)$ , or antiperiodic boundary conditions,  $\psi(x,0) = -\psi(x,W)$ , on the wave functions. In the longitudinal direction we have absorbing boundary conditions [36], corresponding to normal - metal reservoirs at  $x = 0$  and  $x = L$ .

The scattering matrix  $\mathcal{S}$  of the entire structure has  $\mathcal{N} \times \mathcal{N}$  reflection and transmission blocks,

$$\mathcal{S} = \begin{pmatrix} \mathcal{R} & -\mathcal{T}^T \\ \mathcal{T} & \mathcal{R}' \end{pmatrix}. \quad (5.10)$$

The reflection block is a real antisymmetric matrix. Its Pfaffian [34] determines the topological quantum number [15],

$$\mathcal{Q} = \text{sign } Q, \quad Q = (\text{Pf } \mathcal{R}_{\text{pbc}})(\text{Pf } \mathcal{R}_{\text{apbc}}), \quad (5.11)$$

where the labels pbc and apbc refer to the periodic and antiperiodic boundary conditions. (It does not matter if one takes  $\mathcal{R}$  or  $\mathcal{R}'$ , they give the same  $Q$ .)

The use of periodic (or antiperiodic) boundary conditions is convenient to minimize finite-size effects and is sufficient to study bulk properties. To study edge properties, one can impose reflecting boundary conditions by terminating the lattice as described in Ref. 37. Depending on how the lattice is terminated, one would then find that either  $Q = +1$  or  $Q = -1$  produces a helical edge state along the boundary, and therefore represents a topologically nontrivial phase. In the present study, without reflecting boundaries, we can distinguish different topological phases — but we cannot decide which phase is trivial and which nontrivial.

In addition to the topological quantum number we calculate the two-terminal thermal conductance  $G$  of the strip. This transport property is determined by the transmission matrix  $\mathcal{T}$ ,

$$G = G_0 \text{Tr } \mathcal{T} \mathcal{T}^\dagger, \quad (5.12)$$

with  $G_0 = \pi^2 k_B^2 T_0 / 6h$  the thermal conductance quantum and  $T_0$  the temperature of the normal-metal reservoirs. The dimensionless thermal conductivity  $g$  is defined by

$$g = (L/W)(G/G_0). \quad (5.13)$$

For the calculation of the thermal conductivity we take periodic boundary conditions in the  $y$ -direction and a large aspect ratio  $W/L = 4$ , so that the choice of boundary conditions in the transverse direction has only a small effect.

## 5.5 Topological phase transitions

### 5.5.1 Phase diagram without disorder

In the absence of disorder the location of the topological phase transitions can be determined exactly using a duality relation, see App. 5.7.1. We find that the topological quantum number switches sign at critical points  $\alpha_c, \vartheta_c$  that satisfy

$$|\sin \alpha_c \cos \vartheta_c| = |\cos \alpha_c|. \quad (5.14)$$

The phase boundaries are plotted in Fig. 5.3 (left panel), together with the values of the topological quantum number (5.11) at the two sides of the transition. For  $\vartheta_c = 0$  we recover the known value  $\alpha_c = \pi/4$  of the critical point in the chiral Cho-Fisher model [14]. This is as expected, since for  $\vartheta = 0$  our helical network model consists of two independent chiral copies.

### 5.5.2 Scaling of the critical conductivity

At the phase boundaries the excitation gap of the system closes. In the chiral network model this produces a scale-invariant thermal conductivity  $g = 1/\pi$ , regardless of whether the system is disordered or not [13], but in our helical model the conductivity at the critical point scales ballistically  $\propto L$  in the absence of disorder. The ballistic scaling is demonstrated in Fig. 5.4 and can be understood by examining the long-wave length Hamiltonian corresponding to the network model.

The calculation of this Hamiltonian proceeds entirely along the lines of the analogous calculation for the quantum spin-Hall insulator [38], so



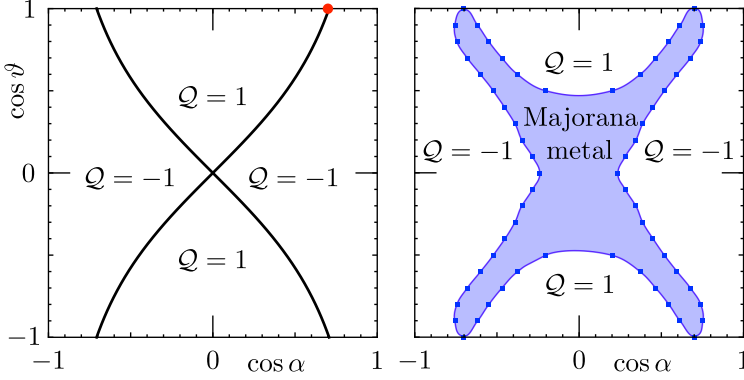


**Figure 5.3.** *Left panel:* Phase diagram of the DIII network model without disorder. The solid curves, given by Eq. (5.14), separate helical topological superconductors with different values  $\mathcal{Q}$  of the  $\mathbb{Z}_2$  topological quantum number. The red dot (at  $\vartheta = 0$ ,  $\alpha = \pi/4$ ) marks the critical point in the Cho-Fisher model [14] of a chiral topological superconductor (class D). *Right panel:* Phase diagram in the presence of disorder ( $q = 0.07$ ), when the topologically distinct phases are separated by a thermal (Majorana) metal.

we only give the result. To first order in the deviation from the Cho-Fisher critical point  $(\alpha, \vartheta) = (\pi/4, 0)$ , we find

$$H = \mathcal{U}^\dagger [p_x \tau_x \sigma_z + p_y \tau_y \sigma_0 + 2(\alpha - \pi/4) \tau_z \sigma_0 + \sqrt{2} \vartheta \tau_y \sigma_y] \mathcal{U} \\ = (p_x \tau_x + p_y \tau_y) \sigma_0 + 2(\alpha - \pi/4) \tau_z \sigma_z + \sqrt{2} \vartheta \tau_0 \sigma_x, \quad (5.15)$$

$$\mathcal{U} = \frac{1}{2}(\tau_0 + i\tau_y) \sigma_0 + \frac{1}{2}(\tau_0 - i\tau_y) \sigma_z. \quad (5.16)$$

Up to a unitary transformation  $\mathcal{U}$ , and to first order in (dimensionless) momentum  $p$ , this Hamiltonian has the form of  $H_{\text{DIII}}$  in Eq. (5.2), with  $\alpha$  playing the role of the chemical potential  $\mu$  and  $\vartheta$  playing the role of the spin coupling strength  $K$ .

The gap closes at  $\alpha = \pi/4$  on a (twofold degenerate) circle  $p_x^2 + p_y^2 = 2\vartheta^2$  in momentum space (inset in Fig. 5.4). The Fermi wavevector  $k_F = \sqrt{2}|\vartheta|/a$  corresponds to a ballistic conductance  $G/G_0 = 2k_F W/\pi$ . Hence we find the ballistic critical conductivity

$$g_c = \frac{2\sqrt{2}|\vartheta|L}{\pi a}, \quad |\vartheta| \ll 1. \quad (5.17)$$

The ballistic scaling of the critical conductivity is a signature of the appearance of a Fermi circle at the phase transition, which is a spe-

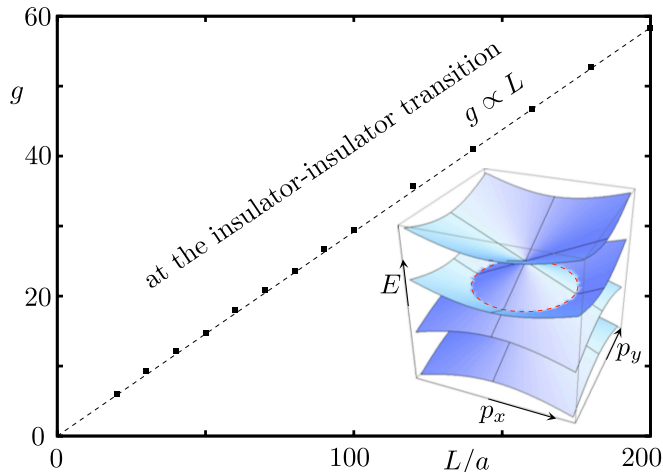


**Figure 5.4.** Data points (with dashed line as a guide to the eye): conductivity as a function of system size (at fixed aspect ratio  $W/L = 4$ ) of the DIII network model without disorder, at criticality for  $\vartheta = 0.4$ . The ballistic scaling  $g \propto L$  results from the Fermi circle of the long-wavelength Hamiltonian (5.15) (red dotted circle in the inset).

cial property of our model (chosen to maximize the coupling between the two opposite chiralities). More generally, the gap in a class-DIII Hamiltonian will close at four isolated points in momentum space [39], resulting in a scale-invariant critical conductivity.

### 5.5.3 Phase diagram with disorder

As disorder is introduced in the system, a metallic phase develops in between the insulating phases, so that the switch from  $Q = +1$  to  $Q = -1$  goes via two metal-insulator transitions. In the metallic region  $Q$  has a random sign, averaging out to zero (see Fig. 5.5, where we averaged  $Q$  rather than  $Q = \text{sign } Q$  to reduce statistical fluctuations). The phase diagram is shown in Fig. 5.3 (right panel) for a fixed disorder strength  $q$  in the  $\alpha$ - $\vartheta$  plane and in Fig. 5.6 for fixed  $\vartheta$  in the  $\alpha$ - $q$  plane. The metallic regions become broader and broader with increasing disorder, and for  $q \gtrsim 0.2$  no insulating phase is left.

Fig. 5.7 shows the sample-size dependence of the average conductivity, both at the metal-insulator transition and in the metallic phase. (The exponential decay  $\propto \exp(-L/\xi)$  in the insulating phase is not shown.)

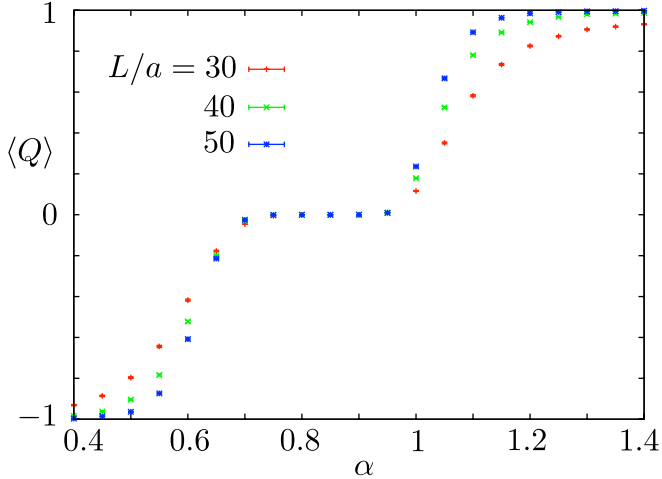


**Figure 5.5.** Disorder average of  $Q$ , defined in Eq. (5.11) as a function of  $\alpha$  for fixed  $\vartheta = 0.5$ ,  $q = 0.1$ , and different values of  $L = W/4$ . The topological quantum number switches from  $-1$  to  $+1$  in the insulating phases via a plateau of zero average in the metallic phase.

While without disorder the conductivity scales ballistically  $\propto L$  at the critical point (see Fig. 5.4), disorder restores the scale invariance that is the hallmark of criticality. In the metallic phase we find a logarithmically increasing conductivity  $\langle g \rangle = c \ln(L/a)$ , characteristic for a Majorana metal [5, 12, 13], with  $c = 1/\pi$  (dotted line in Fig. 5.7).

### 5.5.4 Critical exponent

The metal-insulator transition is associated with a diverging localization length  $\xi \propto |x - x_c|^{-\nu}$ , where  $x$  can be any of the control parameters  $\alpha, \vartheta, q$  and  $x_c$  is the value of  $x$  at the critical point. To determine the critical exponent  $\nu$  we perform a finite-size scaling analysis of the thermal conductivity, in a manner analogous to the work of Slevin and Ohtsuki [40].

Typical data is shown in Fig. 5.8, where we follow the thermal conductivity through the metal-insulator transition upon varying the disorder strength  $q$  at fixed  $\alpha$  and  $\vartheta$ . The dimensions  $L$  and  $W$  of the system are increased at fixed aspect ratio  $W/L = 4$ . The curves are fits of the data to the scaling law, as described in App. 5.7.2. Results are given in Table 5.1.

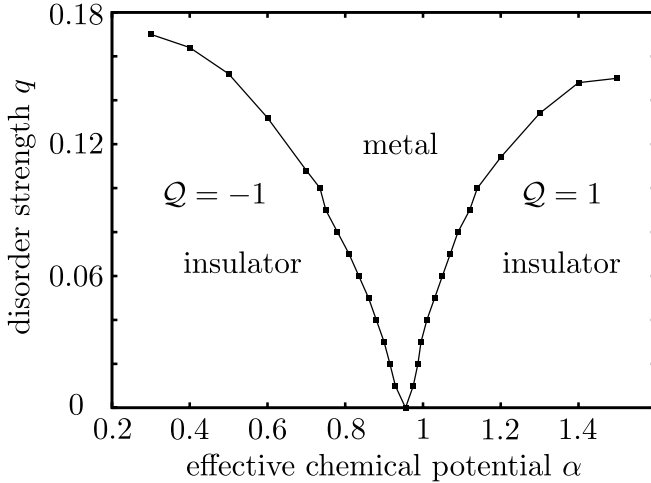


**Figure 5.6.** Phase diagram of the disordered DIII network model for fixed  $\vartheta = 0.785$ .

control parameter	$\nu$	$g_c$
$x \equiv q, \alpha = 1.2, \vartheta = 0.5$	2.04 [1.89, 2.15]	0.75 [0.68, 0.81]
$x \equiv \alpha, q = 0.1, \vartheta = 0.785$	1.93 [1.78, 2.24]	0.73 [0.69, 0.76]

**Table 5.1.** Critical exponent  $\nu$  and critical conductivity  $g_c$ , with  $\pm 3\sigma$  confidence levels indicated by square brackets, extracted from a finite-size scaling analysis with  $x = q$  or  $x = \alpha$  as control parameter to drive the system through a metal-insulator transition. The two cases correspond to transitions into a topological phase with opposite value of  $Q$ .

## 5.6 Conclusion

In conclusion, we have presented a network model of a two-dimensional helical  $p$ -wave superconductor and used it to investigate the topological phase transitions. The presence of time-reversal symmetry (class DIII) leads to differences with the more familiar chiral  $p$ -wave superconductors (class D), of a qualitative nature (the appearance of a thermal metal separating the thermally insulating phases) and also of a quantitative nature (an approximate doubling of the critical exponent). Helical superconductors have not yet been convincingly demonstrated in experiments, but there is an active search and a variety of candidate materials [48–52].

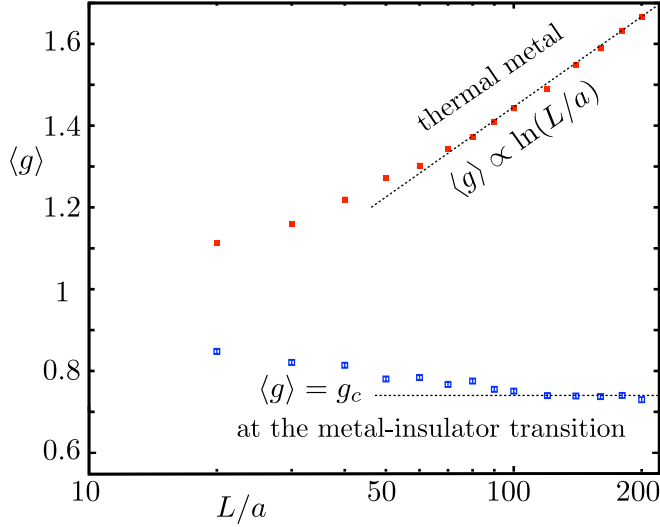


**Figure 5.7.** Scaling of the conductivity in the disordered DIII network model ( $\alpha = 1.2$ ,  $\vartheta = 0.5$ ), at the metal-insulator transition (blue data points,  $q = 0.175$ ) and in the metallic phase (red data points,  $q = 0.2$ ). The dotted lines indicate the scale-invariance of the critical conductivity and the logarithmic scaling of the metallic conductivity.

This study fills in the last missing entry in the list of critical exponents of two-dimensional topological phase transitions (see Table 5.2), completing a line of research on network models that started with the seminal work of Chalker and Coddington on the quantum Hall effect [27]. It is intriguing that the effect of time-reversal symmetry is close to a doubling of the critical exponent (from  $\nu \approx 1.0$  in class D to  $\nu \approx 2.0$  in class DIII), but this may well be accidental.

	symmetry class	time-rev. symmetry	spin-rot. symmetry	topological quantum nr.	insul.-insul. transition	metal-insul. transition	Refs.
quantum Hall insulator	A	×	×	$\mathbb{Z}$	$\nu \approx 2.6$	—	27, 41
quantum spin-Hall insul.	AII	✓	×	$\mathbb{Z}_2$	—	$\nu \approx 2.7$	42, 43, 28, 44, 45
chiral $d$ -wave supercond.	C	×	✓	$\mathbb{Z}$	$\nu = 4/3$	—	46, 47
chiral $p$ -wave supercond.	D	×	×	$\mathbb{Z}$	$\nu = 1$	$\nu \approx 1.0$	13, 24
helical $p$ -wave supercond.	DIII	✓	×	$\mathbb{Z}_2$	—	$\nu \approx 2.0$	<i>this work</i>

**Table 5.2.** Overview of the critical exponents in the five symmetry classes that exhibit a topological phase transition in two dimensions.

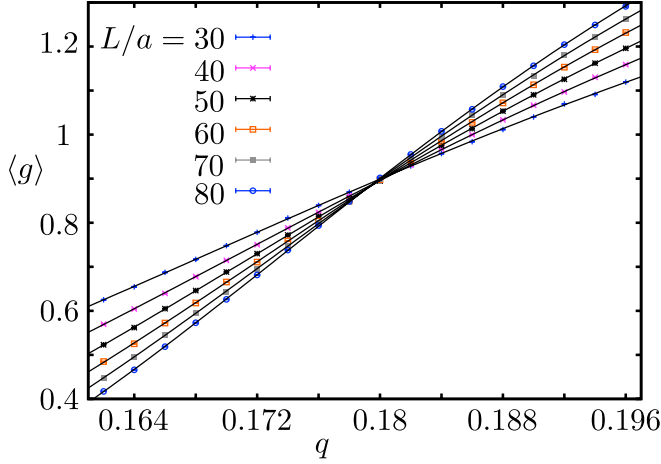


**Figure 5.8.** Disorder-averaged conductivity as a function of disorder strength for various system sizes  $L = W/4$  at fixed  $\alpha = 1.2$ ,  $\vartheta = 0.5$ . Solid curves are a fit to the scaling law, as described in App. 5.7.2.

## 5.7 Appendix

### 5.7.1 Location of the critical point in the network model without disorder

The critical point in the clean DIII network model ( $q = 0$ ) can be obtained from a duality relation: Exchange of the scattering matrices  $S$  and  $S'$  of the two sublattices (black and white nodes in Fig. 5.2) has the effect of exchanging the trivial and nontrivial phases. This can be seen most easily for reflecting boundary conditions, when exchange of the sublattices either creates or removes the helical edge state (see Fig. 7 of Ref. 37).

The exchange of  $S$  and  $S'$  amounts to the transformation of  $\alpha, \vartheta$  into  $\alpha', \vartheta'$ , given by

$$\begin{aligned} \cos \alpha' &= -\sin \alpha \cos \vartheta, & \cos \alpha &= -\sin \alpha' \cos \vartheta', \\ \sin \alpha' \sin \vartheta' &= \sin \alpha \sin \vartheta. \end{aligned} \quad (5.18)$$

Equivalently, the unit vector  $\hat{n} = (\sin \alpha \cos \vartheta, \sin \alpha \sin \vartheta, \cos \alpha)$  is transformed into

$$n'_x = -n_z, \quad n'_y = n_y, \quad n'_z = -n_x, \quad (5.19)$$

which amounts to a reflection in the plane  $x + z = 0$ . The network is selfdual if  $\hat{n}$  lies in this plane. Since a selfdual network is at the critical point, we arrive at a sufficient condition for criticality,  $n_x + n_z = 0$ , or equivalently

$$\sin \alpha_c \cos \vartheta_c + \cos \alpha_c = 0. \quad (5.20)$$

An alternative condition can be obtained by noting that the transformation  $\alpha \mapsto -\alpha$  leaves the reflection matrix  $\mathcal{R}$  unaffected. The topological quantum number (5.11) therefore remains unchanged, so if  $\alpha_c, \vartheta_c$  is critical then also  $-\alpha_c, \vartheta_c$ . We thus have a second sufficient condition for criticality,

$$-\sin \alpha_c \cos \vartheta_c + \cos \alpha_c = 0. \quad (5.21)$$

Eqs. (5.20) and (5.21) together give the condition (5.14).

### 5.7.2 Finite-size scaling analysis

control parameter	fit parameters	irrelevant exp.	reduced $\chi^2$	nr. of degrees of freedom	goodness of fit
$x \equiv q$ $\alpha = 1.2, \vartheta = 0.5$	$n = m_1 = 1, m_0 = 3$ $q_r = 2, q_i = 0$	$y = -0.47$ [-0.76, -0.31]	1.06	98	0.56
$x \equiv \alpha$ $q = 0.1, \vartheta = 0.785$	$n = 1, m_0 = m_1 = 2$ $q_r = 3, q_i = 1$	$y = -0.67$ [-0.78, -0.53]	1.06	128	0.56

**Table 5.3.** Parameters for the nonlinear fitting analysis, giving the critical exponent and conductivity of Table 5.2.

We determine the critical exponent  $\nu$  associated with the metal - insulator transitions on both sides of the metallic phase, by an analysis of the system size  $L = W/4$  dependence of the disorder averaged conductivity  $g$ . Following the general approach of Slevin and Ohtsuki [40], we take into account finite-size corrections to scaling in the form of nonlinearities in the scaling variable  $u$ , as well as the presence of an irrelevant scaling exponent  $y < 0$ .

The finite-size scaling law reads

$$g = F(u_0 L^{1/\nu}, u_1 L^y), \quad (5.22)$$

in terms of the relevant scaling variable  $u_0$  and the leading irrelevant scaling variable  $u_1$ . We perform a Taylor expansion, first up to order  $n$  in powers of  $u_1$ ,

$$g = \sum_{k=0}^n u_1^k L^{ky} F_k(u_0 L^{1/\nu}), \quad (5.23)$$

and then on each of the functions  $F_k$  up to order  $m_k$  in powers of  $u_0$ ,

$$F_k(u_0 L^{1/\nu}) = \sum_{j=0}^{m_k} u_0^j L^{j/\nu} F_{kj}. \quad (5.24)$$

We tune through the metal-insulator transition by varying one parameter  $x \in \{\alpha, \vartheta, q\}$  through the critical point  $x_c$ , keeping the other two parameters fixed. Nonlinearities are taken into account by Taylor expanding the relevant and irrelevant scaling variables in powers of  $x - x_c$ , up to orders  $q_r$  and  $q_i$  respectively,

$$u_0(x - x_c) = \sum_{k=1}^{q_r} b_k (x - x_c)^k, \quad (5.25)$$

$$u_1(x - x_c) = \sum_{k=0}^{q_i} c_k (x - x_c)^k. \quad (5.26)$$

The expansion of the relevant scaling variable does not contain a zeroth order term, due to the requirement  $u_0(0) = 0$  for a scale-invariant critical conductivity.

The average conductivity is determined up to a precision between  $\sim 0.2\%$  and  $\sim 0.07\%$  (error bars much smaller than the size of the symbols in Fig. 5.8). We perform the fit by minimizing the  $\chi^2$  statistic, and express the goodness of fit as well as the degree of uncertainty in the fit parameters through a Monte Carlo resampling technique [53], as appropriate for a non-linear fitting function. Results are collected in Tables 5.1 and 5.3.



# Bibliography

- [1] S. Ryu, A. Schnyder, A. Furusaki, and A. Ludwig, *New J. Phys.* **12**, 065010 (2010).
- [2] M. Z. Hasan and C. L. Kane, *Rev. Mod. Phys.* **82**, 3045 (2010).
- [3] X.-L. Qi and S.-C. Zhang, *Rev. Mod. Phys.* **83**, 1057 (2011).
- [4] N. Read and D. Green, *Phys. Rev. B* **61**, 10267 (2000).
- [5] T. Senthil and M. P. A. Fisher, *Phys. Rev. B* **61**, 9690 (2000).
- [6] A. Vishwanath, *Phys. Rev. Lett.* **87**, 217004 (2001).
- [7] The thermal QH effect also appears in a chiral *d*-wave superconductor, with spin-singlet rather than spin-triplet pairing, but the thermal QSH effect requires the broken spin-rotation symmetry of spin-triplet pairing.
- [8] S. Ryu, J. E. Moore, and A. W. W. Ludwig, *Phys. Rev. B* **85**, 045104 (2012).
- [9] Z. Wang, X-L. Qi, and S-C. Zhang, *Phys. Rev. B* **84**, 014527 (2011).
- [10] K. Nomura, S. Ryu, A. Furusaki, and N. Nagaosa, *Phys. Rev. Lett.* **108**, 026802 (2012).
- [11] M. Stone, *Phys. Rev. B* **85**, 184503 (2012).
- [12] F. Evers and A. D. Mirlin, *Rev. Mod. Phys.* **80**, 1355 (2008).
- [13] M. V. Medvedyeva, J. Tworzydło, and C. W. J. Beenakker, *Phys. Rev. B* **81**, 214203 (2010).

- [14] S. Cho and M. P. A. Fisher, *Phys. Rev. B* **55**, 1025 (1997).
- [15] I. C. Fulga, F. Hassler, A. R. Akhmerov, *Phys. Rev. B*, **85**, 165409 (2012).
- [16] A. Altland and M. R. Zirnbauer, *Phys. Rev. B* **55**, 1142 (1997).
- [17] In the lattice model of Ref. 13 the lattice constant  $a$  of the two-dimensional square lattice provides an effective mass  $m = \hbar/av_{\Delta}$  in the continuum Hamiltonian (5.1). The disorder potential  $U$  fluctuates from site to site, uniformly in the range  $(-\delta U, \delta U)$ . In the continuum formulation this amounts to a correlator  $\int \langle U(0)U(\mathbf{r}) \rangle d\mathbf{r} \simeq (\hbar\delta U/mv_{\Delta})^2$ .
- [18] J. T. Chalker, N. Read, V. Kagalovsky, B. Horowitz, Y. Avishai, and A. W. W. Ludwig, *Phys. Rev. B* **65**, 012506 (2001).
- [19] A. Mildenberger, F. Evers, A. D. Mirlin, and J. T. Chalker, *Phys. Rev. B* **75**, 245321 (2007).
- [20] V. Kagalovsky and D. Nemirovsky, *Phys. Rev. Lett.* **101**, 127001 (2008).
- [21] M. Wimmer, A. R. Akhmerov, M. V. Medvedyeva, J. Tworzydło, and C. W. J. Beenakker, *Phys. Rev. Lett.* **105**, 046803 (2010).
- [22] Y. E. Kraus and A. Stern, *New J. Phys.* **13**, 105006 (2011).
- [23] C. R. Laumann, A. W. W. Ludwig, D. A. Huse, and S. Trebst, *Phys. Rev. B* **85**, 161301(R) (2012).
- [24] A. W. W. Ludwig, M. P. A. Fisher, R. Shankar, and G. Grinstein, *Phys. Rev. B* **50**, 7526 (1994).
- [25] J. M. J. van Leeuwen, private communication (2011).
- [26] B. Kramer, T. Ohtsuki, and S. Kettmann, *Phys. Rep.* **417**, 211 (2005).
- [27] J. T. Chalker and P. D. Coddington, *J. Phys. C* **21**, 2665 (1988).
- [28] H. Obuse, A. Furusaki, S. Ryu, and C. Mudry, *Phys. Rev. B* **76**, 075301 (2007).

- [29] V. Kagalovsky, B. Horowitz, Y. Avishai, and J. T. Chalker, *Phys. Rev. Lett.* **82**, 3516 (1999).
- [30] I. C. Fulga, F. Hassler, A. R. Akhmerov, and C. W. J. Beenakker, *Phys. Rev. B* **83**, 155429 (2011).
- [31] The parameterization (5.5) follows from the general polar decomposition of a class DIII scattering matrix of dimension  $2\mathcal{N} \times 2\mathcal{N}$  given in Ref. 30. The  $\mathcal{N} = 2$  result is simplified by means of the identity  $OAO^T = \eta A$ , with  $\eta = \text{Det } O$ .
- [32] X.-L. Qi, T. L. Hughes, S. Raghu, and S.-C. Zhang, *Phys. Rev. Lett.* **102**, 187001 (2009).
- [33] Ref. 21 shows that electrostatic disorder in a chiral  $p$ -wave superconductor can produce Majorana zero-modes, just like vortex disorder, but this requires a nonzero  $p^2$  term in the Hamiltonian. Random-mass Dirac fermions in graphene have a long-wavelength Hamiltonian of the form (5.1), without the  $p^2$  term and therefore lack zero modes. See: J. H. Bardarson, M. V. Medvedyeva, J. Tworzydło, A. R. Akhmerov, and C. W. J. Beenakker, *Phys. Rev. B* **81**, 121414(R) (2010).
- [34] To calculate the Pfaffian we used the efficient numerical routine of M. Wimmer, *ACM Trans. Math. Software* **38**, 30 (2012).
- [35] X.-L. Qi, T. L. Hughes, and S.-C. Zhang, *Phys. Rev. B* **81**, 134508 (2010).
- [36] The orientation of the network in Fig. 5.2 is chosen such that the interface resistance at the absorbing boundaries  $x = 0, L$  is minimized. A  $45^\circ$  rotation is more convenient to create reflecting boundaries at  $y = 0, W$ , but gives a substantially larger interface resistance at the absorbing boundaries.
- [37] H. Obuse, A. Furusaki, S. Ryu, and C. Mudry, *Phys. Rev. B* **78**, 115301 (2008).
- [38] S. Ryu, C. Mudry, H. Obuse, and A. Furusaki, *New J. Phys.* **12**, 065005 (2010).
- [39] B. Béri, *Phys. Rev. B* **81**, 134515 (2010).

- 
- [40] K. Slevin, T. Ohtsuki, Phys. Rev. Lett. **82**, 382 (1999).
- [41] K. Slevin and T. Ohtsuki, Phys. Rev. B **80**, 041304(R) (2009); arXiv:1203.1384.
- [42] Y. Asada, K. Slevin, and T. Ohtsuki, Phys. Rev. B **70**, 035115 (2004).
- [43] P. Markoš, and L. Schweitzer, J. Phys. A **39**, 3221 (2006).
- [44] K. Kobayashi, T. Ohtsuki, and K. Slevin, arXiv:1201.0244.
- [45] E. P. L. van Nieuwenburg, J. M. Edge, J. P. Dahlhaus, J. Tworzydło, and C. W. J. Beenakker, Phys. Rev. B **85**, 165131 (2012).
- [46] I. A. Gruzberg, A. W. W. Ludwig, and N. Read, Phys. Rev. Lett. **82**, 4524 (1999).
- [47] E. J. Beamd, J. Cardy, and J. T. Chalker, Phys. Rev. B **65**, 214301 (2002).
- [48] Y. Tanaka, T. Yokoyama, A. V. Balatsky, and N. Nagaosa, Phys. Rev. B **79**, 060505 (2009).
- [49] M. Sato and S. Fujimoto, Phys. Rev. B **79**, 094504 (2009).
- [50] C.-X. Liu and B. Trauzettel, Phys. Rev. B **83**, 220510 (2011).
- [51] L. M. Wong and K. T. Law, arXiv:1110.4575.
- [52] S. Nakosai, Y. Tanaka, and N. Nagaosa, Phys. Rev. Lett. **108**, 147003 (2012).
- [53] W. Press, B. Flannery, and S. Teukolsky, *Numerical Recipes in Fortran*, Chapter 15 (Cambridge University Press, Cambridge, 1992).

## Chapter 6

# Adaptive tuning of Majorana fermions in a quantum dot chain

### 6.1 Introduction

Majorana fermions are the simplest quasiparticles predicted to have non-Abelian statistics [1, 2]. These topologically protected states can be realized in condensed matter systems, by making use of a combination of strong spin-orbit coupling, superconductivity, and broken time-reversal symmetry [3–8]. Recently, a series of experiments have reported the possible observation of Majorana fermions in semiconducting nanowires [9–12], attracting much attention in the condensed matter community.

Associating the observed experimental signatures exclusively with these non-Abelian quasiparticles, however, is not trivial. The most straightforward signature, the zero bias peak in Andreev conductance [13, 14] is not unique to Majorana fermions, but can appear as a result of various physical mechanisms [15–21], such as the Kondo effect or weak anti-localization. It has also been pointed out that disorder has a detrimental effect on the robustness of the topological phase, since in the absence of time-reversal symmetry it may close the induced superconducting gap [22]. This requires experiments performed with very clean systems. Additionally, the presence of multiple transmitting modes reduces the amount of control one has over such systems [23–26], and the contribution of extra modes to conductance hinders the observation of

Majorana fermions [27]. Thus, nanowire experiments need setups in which only few modes contribute to conductance.

In this work we approach the problem of realizing systems in a non-trivial topological phase from a different angle. Following the work by Sau and Das Sarma [28], we wish to emulate the Kitaev chain model [29] which is the simplest model exhibiting unpaired Majorana bound states. The proposed system consists of a chain of quantum dots (QDs) defined in a two-dimensional electron gas (2DEG) with spin orbit coupling, in proximity to superconductors and subjected to an external magnetic field. Our geometry enables us to control the parameters of the system to a great extent by varying gate potentials and superconducting phases. We will show how to fine tune the system to the so-called “sweet spot” in parameter space, where the Majorana fermions are well-localized at the ends of the system, making the topological phase maximally robust. A sketch of our proposed setup is presented in Fig. 6.1a).

The setup we propose and the tuning algorithm is not restricted solely to systems created in a two-dimensional electron gas. The essential components are the ability to form a chain of quantum dots and tune each dot separately. In semiconducting nanowires the dots can be formed from wire segments separated by gate-controlled tunnel barriers, and all the tuning can be done by gates, except for the coupling to a superconductor. This coupling, in turn, can be controlled by coupling two superconductors to each dot and applying a phase difference to these superconductors. The layout of a nanowire implementation of our proposal is shown in Fig. 6.1b).

This geometry has the advantage of eliminating many of the problems mentioned above. By using single level quantum dots, and also quantum point contacts (QPC) in the tunneling regime, we solve issues related to multiple transmitting modes. Additional problems, such as accidental closings of the induced superconducting gap due to disorder, are solved because our setup allows us to tune the system to a point where the topological phase is most robust, as we will show.

We present a step-by-step tuning procedure which follows the behavior of the system in parallel to that expected for the Kitaev chain. As feedback required to control every step we use the resonant Andreev conductance, which allows to track the evolution of the system’s energy levels. We expect that the step-by-step structure of the tuning algorithm should eliminate the large number of non-Majorana explanations of the

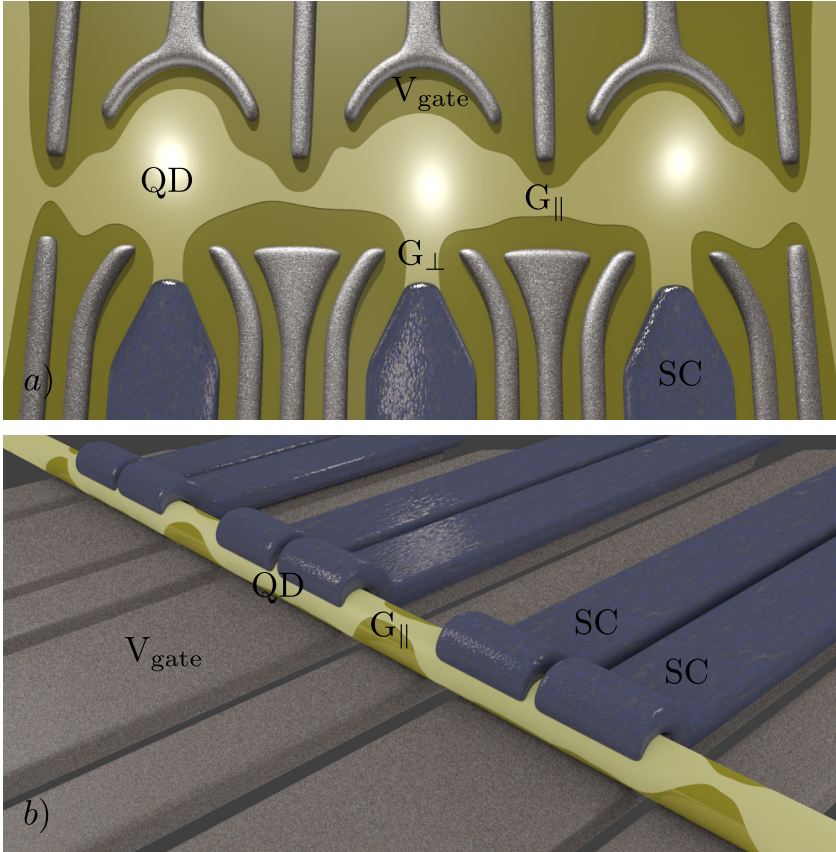


**Figure 6.1.** Examples of systems allowing implementation of a Kitaev chain. Panel (a): a chain of quantum dots in a 2DEG. The QDs are connected to each other, and to superconductors (labeled SC), by means of quantum point contacts. The first and the last dots are also coupled to external leads. The normal state conductance of quantum point contacts (QPCs) between adjacent dots or between the end dots and the leads is  $G_{\parallel}$ , and of the QPCs linking a dot to a superconductor is  $G_{\perp}$ . The confinement energy inside each QD can be controlled by varying the potential  $V_{\text{gate}}$ . Panel (b): Realization of the same setup using a nanowire, with the difference that each dot is coupled to two superconductors in order to control the strength of the superconducting proximity effect without the use of QPCs.

zero bias peaks.

A related layout together with the idea of simulating a Kitaev chain was proposed recently by Sau and Das Sarma [28]. (See also the two dot

limit of that proposal, analyzed in Ref. 30.) Although similar in nature, the geometry which we consider has several advantages. First of all, coupling the superconductors to the quantum dots in parallel, allows us to not rely on crossed Andreev reflection. More importantly, being able to control inter-dot coupling separately from all the other properties allows to address each dot or each segment of the chain electrically. This in turn makes it possible to perform the tuning of the system to the sweet spot regime in a scalable manner. This can be achieved by opening all the QPCs except for the ones that contact the desired dots.

This setup can also be extended to more complicated geometries which include T-junctions of such chains. Benefiting from the high tunability of the system and the localization of the Majorana fermions, it might then be possible to implement braiding [31, 32] and demonstrate their non-Abelian nature.

The rest of this work is organized as follows. In section 6.2 we briefly review a generalized model of Kitaev chain, and identify the "sweet spot" in parameter space in which the Majorana fermions are the most localized. The system of coupled quantum dots is described in section 6.3. For the purpose of making apparent the resemblance of the system to the Kitaev chain, we present a simple model which treats each dot as having a single spinful level. We then come up with a detailed tuning procedure describing how one can control the parameters of the simple model, in order to bring it to the desired point in parameter space. In section 6.4 our tuning prescription is applied to the suggested system of a chain of QDs defined in a 2DEG, and it is shown using numerical simulations that at the end of the process the system is indeed in a robust topological phase. We conclude in section 6.5.

## 6.2 Generalized Kitaev chain

In order to realize unpaired Majorana bound states, we start from the Kitaev chain [29] generalized to the case where the on-site energies as well as the hopping terms are not uniform and can vary from site to site. The generalized Kitaev chain Hamiltonian is defined as

$$H_K = \sum_{n=1}^{L-1} \left[ \left( t_n e^{i\theta_n} a_{n+1}^\dagger a_n + \Delta_n e^{i\phi_n} a_{n+1}^\dagger a_n^\dagger + h.c. \right) + \varepsilon_n a_n^\dagger a_n \right], \quad (6.1)$$



where  $a_n$  are fermion annihilation operators,  $\varepsilon_n$  are the on-site energies of these fermions,  $t_n \exp(i\theta_n)$  are the hopping terms, and  $\Delta_n \exp(i\phi_n)$  are the p-wave pairing terms.

The chain supports two Majorana bound states localized entirely on the first and the last sites, when (i):  $\varepsilon_n = 0$ , (ii):  $\Delta_n = t_n$ , and (iii)  $\phi_{n+1} - \phi_n - \theta_{n+1} - \theta_n = 0$ . The larger values of  $t_n$  lead to a larger excitation gap. The condition (iii) is equivalent, up to a gauge transformation, to the case where the hopping terms are all real, and the phases of the p-wave terms are uniform. The energy gap separating the Majorana modes from the first excited state then equals

$$E_{\text{gap}} = 2 \min \{t_n\}_n. \quad (6.2)$$

The above conditions (i)–(iii), constitute the “sweet spot” in parameter space to which we would like to tune our system. Since all of these conditions are local and only involve one or two sites, our tuning procedure includes isolating different parts of the system and monitoring their energy levels. For that future purpose we will use the expression for excitation energies of a chain of only two sites with  $\varepsilon_1 = \varepsilon_2 = 0$ :

$$E_{12} = \pm(t_1 \pm \Delta_1). \quad (6.3)$$

Exactly at the sweet spot, in order to couple Majorana fermions formed at the ends of the chain, one needs to change at least  $L$  Hamiltonian parameters, where  $L$  is the length of the chain. This happens because any local perturbation would only delocalize Majorana between the dots on which it acts. Hence if a typical imperfection of the tuning due to presence of noise or the imperfection of tuning itself is of an order  $\delta$ , then the residual coupling between Majoranas will be of order of  $(\delta/t)^L$ . Quadratic protection from noise for two such dots in the sweet spot regime was reported in Ref. 30. While for quantum computation applications the length of chains required for sufficient noise tolerance may be relatively large, as we show in Sec. 6.4, in order to detect robust signatures of Majorana fermions, three dots may be sufficient.

## 6.3 System description and the tuning algorithm

The most straightforward way to emulate the Kitaev chain is to create an array of spinful quantum dots, and apply a sufficiently strong Zeeman

field such that only one spin state stays close to the Fermi level. Then the operators of these spin states span the basis of the Hilbert space of the Kitaev chain. If we require normal hopping between the dots and do not utilize crossed Andreev reflection, then in order to have both  $t_n$  and  $\Delta_n$  nonzero we need to break the particle number conservation and spin conservation. The former is achieved by coupling each dot to a superconductor, the latter can be achieved by spatially varying Zeeman coupling [33, 34], or more conventionally by using a material with a sufficiently strong spin-orbit coupling. Examples of implementation of such a chain of quantum dots in a two dimensional electron gas and in semiconducting nanowires are shown in Fig. 6.1.

We neglect all the levels in the dots except for the one closest to the Fermi level, which is justified if the level spacing in the dot is larger than all the other Hamiltonian terms. We neglect the Coulomb blockade, since we assume that the conductance from the dot to the superconductor is larger than the conductance quantum [35]. We consider a single Kramers doublet per dot with creation and annihilation operators  $c_{n,s}^\dagger$  and  $c_{n,s}$ , with  $n$  the dot number and  $s$  the spin degree of freedom. Since we consider dots with spin-orbit interaction,  $c_{n,s}$  is not an eigenstate of spin. Despite that, only singlet superconducting pairing is possible between  $c_{n,s}$  and  $c_{n,s'}$  as long as the time reversal symmetry breaking in a single dot is weak. By applying a proper SU(2) rotation in the  $s$ - $s'$  space we may choose the Zeeman field to point in  $z$ -direction in each dot. As long as the Zeeman field does not change the wave functions of the spin states the superconducting coupling stays  $s$ -wave. The general form of the BdG Hamiltonian describing such a chain of spinful single-level dots is thus given by:

$$\begin{aligned}
 H_S = & \sum_{n,s,s'} \left( \mu_n \sigma_0^{s,s'} + V_z \sigma_z^{s,s'} \right) c_{n,s}^\dagger c_{n,s'} \\
 & + \frac{1}{2} \left( \Delta_{\text{ind},n} e^{i\Phi_n} i \sigma_y^{s,s'} c_{n,s}^\dagger c_{n,s'}^\dagger + \text{h.c.} \right) \\
 & + \left( w_n \left( e^{i\lambda_n \sigma} \right)^{s,s'} c_{n,s}^\dagger c_{n+1,s'} + \text{h.c.} \right),
 \end{aligned} \tag{6.4}$$

where  $\sigma_i$  are Pauli matrices in spin space. The physical quantities entering this Hamiltonian are the chemical potential  $\mu_n$ , the Zeeman energy  $V_z$ , the proximity-induced pairing  $\Delta_{\text{ind},n} \exp(i\Phi_n)$ , and the inter-dot hopping  $w_n$ . The vector  $\lambda_n$  characterizes the amount of spin rotation happening during a hopping between the two neighboring dots (the spin

rotates by a  $2|\lambda|$  angle). This term may be generated either by a spin-orbit coupling, or by a position-dependent spin rotation, required to make the Zeeman field point in the local  $z$ -direction [36, 33, 34]. The induced pairing in each dot  $\Delta_{\text{ind},n} \exp(i\Phi_n)$  is not to be confused with the  $p$ -wave pairing term  $\Delta_n \exp(i\phi_n)$  appearing in the Kitaev chain Hamiltonian (6.1).

In order for the dot chain to mimic the behavior of the Kitaev chain in the sweet spot, each dot should have a single fermion level with zero energy, so that  $\varepsilon_n = 0$ . Diagonalizing a single dot Hamiltonian yields the condition for this to happen:

$$\mu_n = \sqrt{V_z^2 - \Delta_{\text{ind},n}^2}. \quad (6.5)$$

When this condition is fulfilled, each dot has two fermionic excitations

$$a_n = \frac{e^{i\frac{\Phi_n}{2}}}{\sqrt{2V_z}} \left( \sqrt{V_z - \mu_n} c_{n\uparrow}^\dagger - e^{-i\Phi_n} \sqrt{V_z + \mu_n} c_{n\downarrow} \right) \quad (6.6)$$

$$b_n = \frac{e^{i\frac{\Phi_n}{2}}}{\sqrt{2V_z}} \left( \sqrt{V_z - \mu_n} c_{n\downarrow}^\dagger + e^{-i\Phi_n} \sqrt{V_z + \mu_n} c_{n\uparrow} \right). \quad (6.7)$$

The energy of  $a_n$  is zero, the energy of  $b_n$  is  $2V_z$ . If the hopping is much smaller than the energy of the excited state,  $w_n \ll V_z$ , we may project the Hamiltonian (6.4) onto the Hilbert space spanned by  $a_n$ . The resulting projected Hamiltonian is identical to the Kitaev chain Hamiltonian of Eq. (6.1), with the following effective parameters:

$$\varepsilon_n = 0, \quad (6.8a)$$

$$t_n e^{i\theta_n} = w_n (\cos \lambda_n + i \sin \lambda_n \cos \rho_n) \times \left[ \sin(\alpha_{n+1} + \alpha_n) \cos(\delta\Phi_n/2) + i \cos(\alpha_{n+1} - \alpha_n) \sin(\delta\Phi_n/2) \right], \quad (6.8b)$$

$$\Delta_n e^{i\phi_n} = iw_n \sin \lambda_n \sin \rho_n e^{i\tilde{\zeta}_n} \times \left[ \cos(\alpha_{n+1} + \alpha_n) \cos(\delta\Phi_n/2) + i \sin(\alpha_{n+1} - \alpha_n) \sin(\delta\Phi_n/2) \right], \quad (6.8c)$$

where

$$\mu_n = V_z \sin(2\alpha_n), \Delta_{\text{ind},n} = V_z \cos(2\alpha_n), \quad (6.9)$$

$$\lambda_n = \lambda_n (\sin \rho_n \cos \zeta_n, \sin \rho_n \sin \zeta_n, \cos \rho_n)^T, \quad (6.10)$$

and  $\delta\Phi_n = \Phi_n - \Phi_{n+1}$ .

It is possible to extract most of the parameters of the dot Hamiltonian from level spectroscopy, and then tune the effective Kitaev chain Hamiltonian to the sweet spot. The tuning, however, becomes much simpler if two out of three of the dot linear dimensions are much smaller than the spin-orbit coupling length. Then the direction of spin-orbit coupling does not depend on the dot number, and as long as the magnetic field is perpendicular to the spin-orbit field, the phase of the prefactors in Eqs. (6.8) becomes position-independent. Additionally, if the dot size is not significantly larger than the spin-orbit length, the signs of these prefactors are constant. This ensures that if  $\delta\Phi_n = 0$ , the phase matching condition of the Kitaev chain is fulfilled. Since  $\delta\Phi_n = 0$  leads to both  $t_n$  and  $\Delta_n$  having a minimum or maximum as a function of  $\delta\Phi_n$ , this point is straightforward to find. The only remaining condition,  $t_n = \Delta_n$  at  $\delta\Phi = 0$ , requires that  $\alpha_n + \alpha_{n+1} = \lambda_n$ .

The above calculation leads to the following tuning algorithm:

1. Open all the QPCs, except for two contacting a single dot. By measuring conductance while tuning the gate voltage of a nearby gate, ensure that there is a resonant level at zero bias. After repeating for each dot the condition  $\varepsilon_n = 0$  is fulfilled.
2. Open all the QPCs except the ones near a pair of neighboring dots. Keeping the gate voltages tuned such that  $\varepsilon_n = 0$ , vary the phase difference between the neighboring superconductors until the lowest resonant level is at its minimum as a function of phase difference, and the next excited level at a maximum. This ensures that the phase tuning condition  $\phi_{n+1} - \phi_n - \theta_{n+1} - \theta_n = 0$  is fulfilled. Repeat for every pair of neighboring dots.
3. Start from one end of the chain, and isolate pairs of dots like in the previous step. In the pair of  $n$ -th and  $n + 1$ -st dots tune simultaneously the coupling of the  $n + 1$ -st dot to the superconductor and the chemical potential in this dot, such that  $\varepsilon_{n+1}$  stays equal to 0. Find the values of these parameters such that a level at zero

appears in two dots when they are coupled. After that proceed to the following pair.

Having performed the above procedures, the coupling between all of the dots in the chain is resumed, at which point we expect the system to be in a robust topological phase, with two Majorana fermions located on the first and last dots. In practice one can also resume the coupling gradually by, for instance, isolating triplets of adjacent dots, making sure they contain a zero-energy state, and making fine-tuning corrections if necessary, and so on.

## 6.4 Testing the tuning procedure by numerical simulations

We now test the tuning procedure by applying it to a numerical simulation of a chain of three QDs in a 2DEG. The two-dimensional BdG Hamiltonian describing the entire system of the QD chain reads:

$$\begin{aligned} \mathcal{H}_{\text{QDC}} = & \left( \frac{p^2}{2m} + V(x, y) \right) \tau_z + \frac{\alpha}{\hbar} (\sigma_x p_y - \tau_z \sigma_y p_x) \\ & + \Delta_{\text{ind}} (\cos(\Phi) \tau_y + \sin(\Phi) \tau_x) \sigma_y + V_z \tau_z \sigma_z. \end{aligned} \quad (6.11)$$

Here,  $\sigma_i$  and  $\tau_i$  are Pauli matrices acting on the spin and particle-hole degrees of freedom respectively. The term  $V(x, y)$  describes both potential fluctuations due to disorder, and the confinement potential introduced by the gates. The second term represents Rashba spin-orbit coupling,  $\Delta_{\text{ind}}(x, y) \cdot \exp(\Phi(x, y))$  is the s-wave superconductivity induced by the coupled superconductors, and  $V_z$  is the Zeeman splitting due to the magnetic field. Full description of the tight-binding equations used in the simulation is presented in Appendix 6.6.1.

The chemical potential of the dot levels  $\mu_n$  is tuned by changing the potential  $V(x, y)$ . For simplicity we used a constant potential  $V_n$  added to the disorder potential, such that  $V(x, y) = V_n + V_0(x, y)$  in each dot. Varying the magnitude of  $\Delta_{\text{ind},n}$  is done by changing conductance  $G_{\perp}$  of the quantum point contacts, which control the coupling between the dots and the superconductors. Finally, varying the superconducting phase  $\Phi(x, y)$  directly controls the parameter  $\Phi_n$  of the dot to which the superconductor is coupled, although they need not be the same.

The tuning algorithm required monitoring the energy levels of different parts of the system. This can be achieved by measuring the resonant Andreev conductance from one of the leads. The Andreev conductance is given by [37, 38]

$$G/G_0 = N - \text{tr}(r_{ee}r_{ee}^\dagger) + \text{tr}(r_{he}r_{he}^\dagger), \quad (6.12)$$

where  $G_0 = e^2/h$ ,  $N$  is the number of modes in a given lead, and  $r_{ee}$  and  $r_{he}$  are normal and Andreev reflection matrices. Accessing parts of the chain (such as a single dot or a pair of dots) can be done by opening all inter-dot QPCs, and closing all the ones between dots and superconductors, except for part of the system that is of interest.

We begin by finding such widths of QPCs that  $G_{\parallel} \approx 0.02$  and  $G_{\perp} \approx 4G_0$ . This ensures that conductance between adjacent dots, is in tunneling regime and that the dots are strongly coupled to the superconductors such that the effect of Coulomb blockade is reduced [35]. The detailed properties of QPCs are described in App. 6.6.1 and their conductance is shown in Fig. 6.8.

*First step: tuning chemical potential.* We sequentially isolate each dot, and change the dot potential  $V_n$ . The Andreev conductance as a function of  $V_n$  and bias voltage for the second dot is shown in Fig. 6.2. We tune  $V_n$  to the value where a conductance resonance exists at zero bias. This is repeated for each of the dots and ensures that  $\mu_n = 0$ .

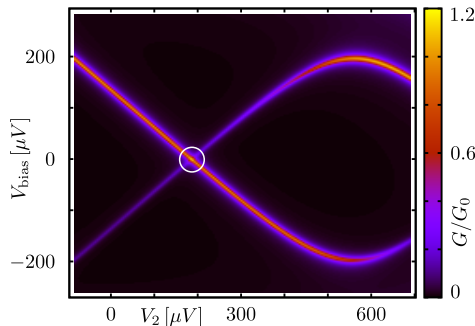


**Figure 6.2.** Andreev conductance measured from the left lead as a function of bias voltage and QD potential (measured relative to quarter filling) for the second dot. Changing the chemical potential allows to tune quasi-bound states to zero energy (white circle).

*Second step: tuning the superconducting phases.* We now set the phases of the induced pairing potentials  $\Phi_n$  to constant. As explained in the previous section, this occurs when  $\Delta_n$  and  $t_n$  experience their maximal and minimal values. According to Eq. (6.3) this happens when the separation between the energy levels of the pair of dots subsection is maximal. Fig. 6.3 shows the evolution of these levels as a function of the phase difference between the two superconductors. The condition  $\delta\Phi_1 = 0$  is then satisfied at the point where their separation is maximal.

*Third step: tuning the couplings.* Finally we tune  $t_n = \Delta_n$ . This is achieved by varying  $G_\perp$ , while tracking the Andreev conductance peak corresponding to the  $t_n - \Delta_n$  eigenvalue of the Kitaev chain we are emulating. After every change of  $G_\perp$  we readjust  $V_n$  in order to make sure that the condition  $\varepsilon_n = 0$  (or equivalently  $V_z^2 = \mu_n^2 + \Delta_n^2$ ) is maintained. This is necessary because not just  $\Delta_n$ , but also  $\mu_n$  depend on  $G_\perp$ . Therefore, successive changes of  $G_\perp$  and  $V_n$  are performed until the smallest bias peak is located at zero bias. The tuning steps of the first two dots are shown in Fig. 6.4. We repeat steps 2 and 3 for each pair of dots in the system.

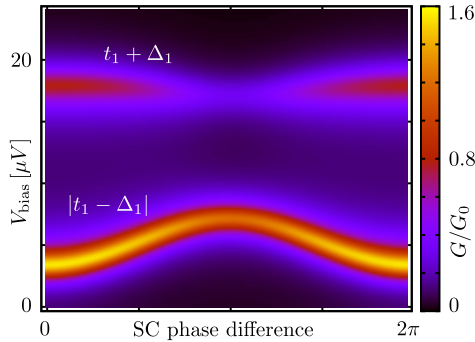


**Figure 6.3.** Conductance as a function of bias voltage and superconducting phase difference for a two-dot system. The two lowest energy levels are given by Eq. (6.3) of a two site Kitaev chain, as indicated. At the point where their separation is maximal (SC phase difference 0 in the plot), the phase difference  $\delta\Phi_n$  of the induced superconducting gaps vanishes.

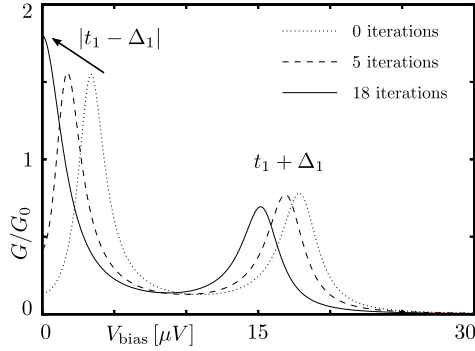


**Figure 6.4.** Conductance as a function of bias voltage during simultaneous tuning of  $G_{\perp}$  and  $V_n$  for the first pair of dots. The three different plots represent the situation before (dotted line), at an intermediate stage (dashed line), and after (solid line) the tuning. The arrow indicates the evolution of the first peak upon tuning, and the number of successive changes of  $G_{\perp}$  and  $V_n$  are shown for each curve. By bringing the first peak to zero, the third tuning step is achieved.

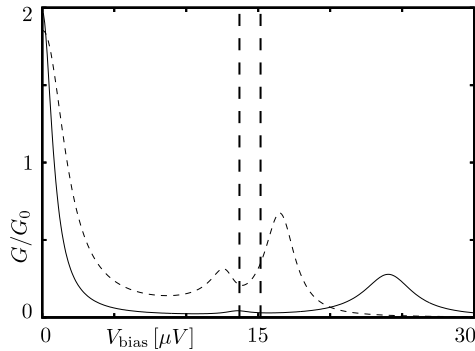


**Figure 6.5.** Conductance as a function of bias voltage for a system composed of three tuned quantum dots (dashed line). The zero bias peak signals the presence of Majorana bound states at the ends of the chain. The first and second excited states are consistent with those expected for a three-site Kitaev chain, namely  $E_1 = 2t_1$  and  $E_2 = 2t_2$  (vertical dashed lines), given the measured values of  $t_1 = \Delta_1$  and  $t_2 = \Delta_2$ , obtained after finalizing the two dot tuning process. As described in the main text, after increasing the transparency of the lead QPC leads to a zero bias peak having a height  $G = 1.98G_0$  (solid line).



Finally, having full all three conditions required for a robust topologically non-trivial phase, we probe the presence of localized Majorana bound state in the full three-dot system by measuring Andreev conductance (see Fig. 6.5). In this specific case, the height of the zero bias peak is approximately  $1.85 G_0$ , signaling that the end states are well but not completely decoupled. Increasing the transparency of the QPC connecting the first dot to the lead brings this value to  $G = 1.98 G_0$ .

## 6.5 Conclusion

In conclusion, we have demonstrated how to tune a linear array of quantum dots coupled to superconductors in presence of Zeeman field and spin-orbit coupling to resemble the Kitaev chain that hosts Majorana bound states at its ends. Furthermore, we have presented a detailed procedure by which the system is brought to the so-called “sweet spot” in parameter space, where the Majorana bound states are the most localized. This procedure involves varying the gates potentials and superconducting phases, as well as monitoring of the excitation spectrum of the system by means of resonant Andreev conductance.

We have tested our procedure using numerical simulations of a system of three QDs, defined in a 2DEG, and found that it works in systems with experimentally reachable parameters. It can be also applied to systems where quantum dots are defined by other means, for example formed in a one-dimensional InAs or InSb wire.

## 6.6 Appendix

### 6.6.1 System parameters in numerical simulations

In this section, we describe the parameters used throughout the numerical simulations. The quantum dots and quantum point contacts are modeled using a tight-binding model defined on a square lattice, with leads and superconductors taken as semi-infinite.

The characteristic length and energy scales of this system are the spin-orbit length  $l_{\text{SO}} = \hbar^2 / m\alpha$ , and the spin-orbit energy  $E_{\text{SO}} = m\alpha^2 / \hbar^2$ . We simulate an InAs system in which the effective electron mass is  $m = 0.015m_e$ , where  $m_e$  is the bare electron mass, taking values of  $E_{\text{SO}} = 1 \text{ K} = 86 \mu\text{eV}$  and  $l_{\text{SO}} = 250 \text{ nm}$ .

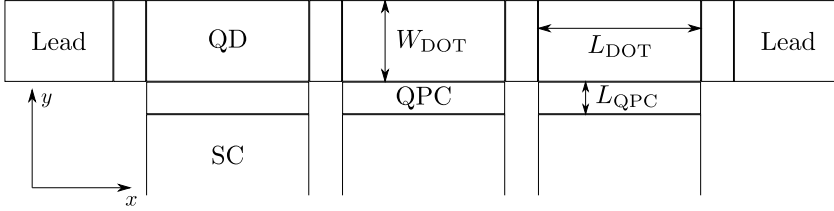


**Figure 6.6.** Geometry of the quantum dot chain. The quantum dots have a width  $W_{\text{DOT}}$  and length equal to  $L_{\text{DOT}}$ . Quantum point contacts have a longitudinal size  $L_{\text{QPC}}$  and a transverse dimension equal to either  $L_{\text{DOT}}$  or  $W_{\text{DOT}}$ . Leads are semi-infinite in the  $x$  direction, and superconductors are modeled as semi-infinite systems in the  $y$  direction.

We consider a setup composed of three quantum dots, like the one shown in Fig. 6.6. Each of the three dots has a length of  $L_{\text{DOT}} = 208$  nm and a width  $W_{\text{DOT}} = 104$  nm. Quantum point contacts have a longitudinal dimension of  $L_{\text{QPC}} = 42$  nm, which is the same as the Fermi wavelength at quarter filling.

The value of the hopping integral is  $t = \hbar^2 / (2ma^2) = 55.8$  meV, with  $a = 7$  nm. Disorder is introduced in the form of random uncorrelated onsite potential fluctuations, leading to a mean free path  $l_{\text{mfp}} = 218.8$  nm. The system is placed in a perpendicular magnetic field characterized by a Zeeman splitting  $V_z = 336$   $\mu\text{eV}$ , which, given a  $g$ -factor of  $35K/T$ , corresponds to a magnetic field  $B_z = 111$  mT. Each dot is additionally connected to a superconductor characterized by a pairing potential  $|\Delta_{\text{SC}}| = 0.86$  meV.

The potential profile across a quantum point contact is given by

$$V_{\text{QPC}}(x) = \frac{\tilde{h}}{2} \left( 2 - \tanh \left( \frac{\tilde{s}}{\tilde{L}} \left( x + \frac{\tilde{w}}{2} \right) \right) + \tanh \left( \frac{\tilde{s}}{\tilde{L}} \left( x - \frac{\tilde{w}}{2} \right) \right) \right), \quad (6.13)$$

where  $x \in [-\tilde{L}/2, \tilde{L}/2]$  is the transverse coordinate across the quantum point contact,  $\tilde{h}$  is the maximum height of  $V_{\text{QPC}}$ ,  $\tilde{s}$  fixes the slope at which the potential changes, and  $\tilde{w}$  is used to tune the QPC transparency. Two examples of potential profiles are shown in Fig. 6.7.

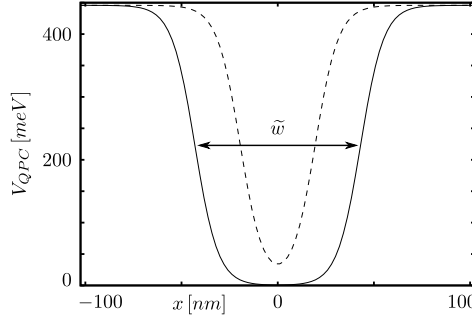


**Figure 6.7.** Potential profile  $V_{\text{QPC}}(x)$  across the transverse direction of a quantum point contact. For the maximum value of this potential, no states are available for quasiparticles in the 2DEG. The two curves show potential profiles for two different QPC transparencies, corresponding to  $\tilde{s} = 17$  and  $\tilde{w} = 87.4, 39.5$  nm for the solid and dashed curves respectively.

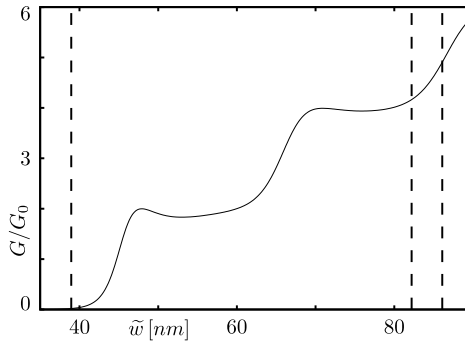


**Figure 6.8.** Conductance of a quantum point contact as a function of  $\tilde{w}$  of Eq. (6.13), for a single QPC. The vertical lines indicate the values at which QPCs are set after tuning. The inter-dot QPCs are all set to the tunneling regime while the ones connecting the dots to the superconductors are set to higher transparencies.



# Bibliography

- [1] J. Alicea, *Rep. Prog. Phys.* **75**, 076501 (2012).
- [2] C. W. J. Beenakker, *Annu. Rev. Con. Mat. Phys.* **4**, 113 (2013).
- [3] L. Fu and C. L. Kane, *Phys. Rev. Lett.* **100**, 096407 (2008).
- [4] M. Sato, Y. Takahashi, and S. Fujimoto, *Phys. Rev. Lett.* **103**, 020401 (2009).
- [5] J. D. Sau, R. M. Lutchyn, S. Tewari, and S. Das Sarma, *Phys. Rev. Lett.* **104**, 040502 (2010).
- [6] J. Alicea, *Phys. Rev. B* **81**, 125318 (2010).
- [7] Y. Oreg, G. Refael, and F. von Oppen, *Phys. Rev. Lett.* **105**, 177002 (2010).
- [8] R. M. Lutchyn, J. D. Sau, and S. Das Sarma, *Phys. Rev. Lett.* **105**, 077001 (2010).
- [9] V. Mourik, K. Zuo, S. M. Frolov, S. R. Plissard, E. P. A. M. Bakkers, and L. P. Kouwenhoven, *Science* **336**, 1003 (2012).
- [10] M. T. Deng, C. L. Yu, G. Y. Huang, M. Larsson, P. Caroff, and H. Q. Xu, *Nano Lett.* **12**, 6414 (2012).
- [11] A. Das, Y. Ronen, Y. Most, Y. Oreg, M. Heiblum, and H. Shtrikman, *Nat. Phys.* **8**, 887 (2012).
- [12] L. P. Rokhinson, X. Liu, and J. K. Furdyna, *Nat. Phys.* **8**, 795 (2012).
- [13] C. J. Bolech and E. Demler, *Phys. Rev. Lett.* **98**, 237002 (2007).

- 
- [14] K. T. Law, P. A. Lee, and T. K. Ng, *Phys. Rev. Lett.* **103**, 237001 (2009).
- [15] S. Sasaki, S. D. Franceschi, J. M. Elzerman, W. G. v. d. Wiel, M. Eto, S. Tarucha, and L. P. Kouwenhoven, *Nature* **405**, 764 (2000).
- [16] D. I. Pikulin, J. P. Dahlhaus, M. Wimmer, H. Schomerus, and C. W. J. Beenakker, *New J. Phys.* **14**, 125011 (2012).
- [17] K. Flensberg, *Phys. Rev. B* **82**, 180516 (2010).
- [18] G. Kells, D. Meidan, and P. W. Brouwer, *Phys. Rev. B* **85**, 060507 (2012).
- [19] S. Tewari, T. D. Stanescu, J. D. Sau, and S. Das Sarma, *Phys. Rev. B* **86**, 024504 (2012).
- [20] F. Pientka, G. Kells, A. Romito, P. W. Brouwer, and F. von Oppen, *Phys. Rev. Lett.* **109**, 227006 (2012).
- [21] J. Liu, A. C. Potter, K. T. Law, and P. A. Lee, *Phys. Rev. Lett.* **109**, 267002 (2012).
- [22] P. Anderson, *J. Phys. Chem. Solids* **11**, 26 (1959).
- [23] A. C. Potter and P. A. Lee, *Phys. Rev. Lett.* **105**, 227003 (2010).
- [24] T. D. Stanescu, R. M. Lutchyn, and S. Das Sarma, *Phys. Rev. B* **84**, 144522 (2011).
- [25] P. W. Brouwer, M. Duckheim, A. Romito, and F. von Oppen, *Phys. Rev. Lett.* **107**, 196804 (2011).
- [26] M.-T. Rieder, G. Kells, M. Duckheim, D. Meidan, and P. W. Brouwer, *Phys. Rev. B* **86**, 125423 (2012).
- [27] M. Wimmer, A. R. Akhmerov, J. P. Dahlhaus, and C. W. J. Beenakker, *New J. Phys.* **13**, 053016 (2011).
- [28] J. D. Sau and S. D. Sarma, *Nat. Comm.* **3**, 964 (2012).
- [29] A. Y. Kitaev, *Phys.-Usp.* **44**, 131 (2001).
- [30] M. Leijnse and K. Flensberg, *Phys. Rev. B* **86**, 134528 (2012).

- 
- [31] J. Alicea, Y. Oreg, G. Refael, F. v. Oppen, and M. P. A. Fisher, *Nat. Phys.* **7**, 412 (2011).
- [32] J. D. Sau, D. J. Clarke, and S. Tewari, *Phys. Rev. B* **84**, 094505 (2011).
- [33] T.-P. Choy, J. M. Edge, A. R. Akhmerov, and C. W. J. Beenakker, *Phys. Rev. B* **84**, 195442 (2011).
- [34] M. Kjaergaard, K. Wlms, and K. Flensberg, *Phys. Rev. B* **85**, 020503 (2012).
- [35] H. Grabert and M. H. Devoret, *Single Charge Tunneling: Coulomb Blockade Phenomena in Nanostructures* (Plenum, New York, 1992).
- [36] B. Braunecker, G. I. Japaridze, J. Klinovaja, and D. Loss, *Phys. Rev. B* **82**, 045127 (2010).
- [37] A. L. Shelankov, *Zh. Eksp. Teor. Fiz., Pis ma.* **32**, 2, 122 (1980).
- [38] G. E. Blonder, M. Tinkham, and T. M. Klapwijk, *Phys. Rev. B* **25**, 4515 (1982).





# Chapter 7

## Statistical Topological Insulators

### 7.1 Introduction

One common definition of a topological insulator (TI) is that it is a bulk insulator which has a gapless surface Hamiltonian that cannot be continuously transformed into a gapped one [1, 2]. The surface states of a TI are protected from Anderson localization and, since there is an anomaly associated with the bulk field theory of such a material [3–5], they are also robust against interactions as long as the latter respect the discrete symmetry of the system. Other possible descriptions of TIs arise naturally from nonlinear sigma-models [6], K-theory [7], Green's functions [8–10], and even string theory [11].

There are, however, several known examples of disordered systems which have a surface whose Hamiltonian can be continuously deformed into a gapped one, and yet is protected against Anderson localization. One such example is a so-called weak TI, a three-dimensional material made by stacking many layers of a two-dimensional TI. Its surface has two Dirac cones which can be coupled by a mass term, producing a gapped system. Despite that, Ringel *et al.* [12] have argued that since an odd number of weak TI layers is conducting, its surface must always be metallic. This prediction was tested numerically [13] and later explained by Fu and Kane [14] in terms of  $\mathbb{Z}_2$  vortex fugacity of a corresponding field theory. Another example of a system avoiding localization is a TI subject to a random magnetic field as long as the magnetic field is zero

on average [15]: a random sign gap appears in the surface dispersion, driving the surface to a critical point of the Chalker-Coddington network model [16].

These two examples share one common trait. In order for the surface to avoid localization, the disordered ensemble has to be invariant under a certain symmetry: translation for a weak TI or time-reversal for a strong TI with a random magnetic field. We show that this property defines a broad class of systems, which we call statistical topological insulators (STI). An STI is an ensemble of disordered systems belonging to the same symmetry class. This ensemble, as a whole, also has to be invariant under an extra symmetry, which we call statistical symmetry since it is not respected by single elements of the ensemble. These elements have surfaces pinned to the middle of a topological phase transition and protected from localization due to the combined presence of the statistical symmetry and the symmetry of each element, if any. For example, for a weak TI the statistical symmetry is translation, while the symmetry of each element is time-reversal.

Some STIs without disorder become topological crystalline insulators, introduced by Liang Fu [17, 18], or in other words, they have a gapless surface dispersion protected by their crystalline symmetry. Nevertheless, not all the topological crystalline insulators become STIs once disorder is added, and the ensemble symmetry need not be crystalline, as in the case of a TI in a random magnetic field.

We show that STIs are a true bulk phase: in order for the surface to become localized without breaking the symmetries, the bulk must undergo a phase transition. This significantly extends the list of possible topological phases. Since the bulk transition of an STI is a topological phase transition by itself, it is possible to construct a higher dimensional system with its surface pinned to the middle of an STI phase transition. Such a construction makes every single topological phase transition [7, 6] give rise to infinitely many higher-dimensional descendant topological phases.

In the following, we start by defining the STI topological invariant when the statistical symmetry group that protects it is  $\mathbb{Z}_2$ . Then we show how to build a tight-binding model for an STI in any dimension and symmetry class, using statistical reflection symmetry. Finally, we check the properties of STIs numerically.

## 7.2 Construction of an STI topological invariant

To determine the necessary conditions required to obtain an STI, let us consider an ensemble of  $d$ -dimensional systems with  $(d-1)$ -dimensional surface. We require that the Hamiltonian  $H_i$  of each element of the ensemble be local, belong to the same symmetry class, and that the correlation function of the matrix elements of this Hamiltonian be sufficiently short-ranged. Additionally, we require that the bulk be insulating. The surface should have a combination of dimensionality and symmetry class allowing it to be in a topological phase with invariant  $Q_{d-1}$ . We consider  $d \geq 2$ , so that both the surface and the bulk are self-averaging [19]. Finally, the ensemble should also possess a statistical symmetry. This means that every ensemble element  $H_i$  is equally likely to appear as  $\mathcal{U}H_i\mathcal{U}^{-1}$ , with  $\mathcal{U}$  a unitary or anti-unitary operator. Examples of such symmetries are reflection, inversion, and time-reversal. Alternatively the ensemble may possess a statistical anti-symmetry, such as particle-hole or chiral symmetry, in which case  $H_i$  appears equally likely as  $-\mathcal{U}H_i\mathcal{U}^{-1}$ .

We consider an interface between two elements of the ensemble,  $H_i$  and  $\pm\mathcal{U}H_i\mathcal{U}^{-1}$ , shown in Fig. 7.1a. Since the combined system is also an element of the ensemble, its bulk should be insulating. Furthermore, if the surfaces of  $H_i$  and  $\pm\mathcal{U}H_i\mathcal{U}^{-1}$  are also insulating, then due to self-averaging they should share the same topological properties. Hence the  $(d-2)$ -dimensional boundary separating the surfaces should carry no topologically protected gapless states. Our aim is to show that for certain ensembles the number of such states must be non-zero, thus leading to a contradiction with the assumption of an insulating surface.

The number of topologically protected gapless states at the boundary can be computed from the full Hamiltonian, as described by Teo and Kane in Ref. [20]. Instead, we deform our system into a simpler one [see Fig. 7.1(a)]. First we add a translationally-invariant surface term  $H_s \equiv \mp\mathcal{U}H_s\mathcal{U}^{-1}$  to  $H_i$  which strongly breaks the statistical symmetry and gaps the surface. For instance, if the statistical symmetry is time-reversal,  $H_s$  could be a strong, uniform Zeeman field at the surface. Simultaneously, a term  $-H_s \equiv \pm\mathcal{U}H_s\mathcal{U}^{-1}$  is added to  $\pm\mathcal{U}H_i\mathcal{U}^{-1}$ , on the other side of the interface. If in the process of adding  $H_s$  to  $H_i$  the surface gap closes, so does the surface gap on the symmetry-reversed side. This means that the parity of the number of topologically protected gapless states at the boundary does not change. Then, we deform  $H_i$

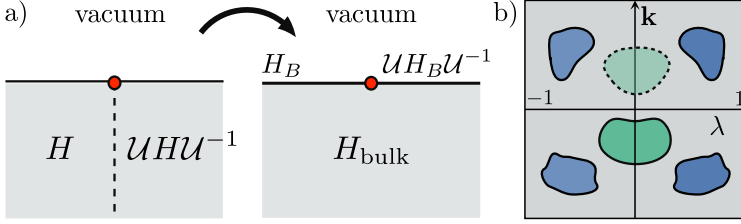


**Figure 7.1.** (a): Given two disordered systems  $H_i, \mathcal{U}H_i\mathcal{U}^{-1}$  mapped into each other by a symmetry  $\mathcal{U}$  and fused into a single system, the presence of gapless states at the domain wall formed at the common surface interface (red circle) reveals a difference in their surface topological invariant. The presence of gapless states can be determined by deforming the system into a clean one with a common,  $\mathcal{U}$ -symmetric  $H_{\text{bulk}}$  and a domain wall between two  $\mathcal{U}$ -symmetry-broken surfaces, as described in the text. (b): Examples of possible patterns of surface Fermi surfaces as a function of the parameter  $\lambda$ , interpolating between a surface and its symmetry reverse, and the surface momenta  $k$ . Green and blue puddles represent Fermi surfaces located at the symmetric point  $\lambda = 0$  or away from it, respectively. A non-trivial STI has an odd number of Fermi surfaces at the symmetric point, while a trivial one has an even number. Thus, in this example, the STI invariant  $\mathcal{Q}$  takes value  $-1(+1)$  in the absence (presence) of the dashed Fermi surface.

and  $\pm\mathcal{U}H_i\mathcal{U}^{-1}$  to remove both disorder and symmetry-breaking, while taking care that in the process the gap does not close anywhere: neither in the bulk of  $H_i$  and  $\pm\mathcal{U}H_i\mathcal{U}^{-1}$  nor at their interface. The new bulk Hamiltonian  $H_{\text{bulk}}$  has no disorder and satisfies  $H_{\text{bulk}} = \pm\mathcal{U}H_{\text{bulk}}\mathcal{U}^{-1}$ . For weak disorder, this step corresponds to reducing disorder strength to zero. While finding  $H_{\text{bulk}}$  in the case of strong disorder is non-trivial, we do not know of any obstructions which would make it impossible, nor of counter-examples.

The evaluation of the number of topologically protected boundary states is straightforward in this new system, since it amounts to the study of a domain wall between the two clean, gapped surfaces. This number is given by the difference in surface topological invariant,  $\Delta Q_{d-1}$ , which can be computed by standard methods, see e.g. Ref. [10], applied to the Hamiltonian  $H = H_{\text{bulk}} + \lambda H_s$ , with  $\lambda \in [-1, 1]$ . In Fig. 7.1(b) we show two possible configurations of gap closings of  $H$  in  $(k, \lambda)$  space, with  $k$  the momentum parallel to the surface. Since a gap closing at a finite value of  $\lambda$  always has a partner at  $-\lambda$ , the parity of  $\Delta Q_{d-1}$  is

dictated by the properties of  $H(\mathbf{k}, \lambda = 0) \equiv H_{\text{bulk}}$ .

If the number of topologically protected gapless states at the boundary is non-zero,  $H_i$  and  $\pm \mathcal{U}H_i\mathcal{U}^{-1}$  must have different topological properties. Since the latter are self-averaging quantities in insulating phases and  $H_i$  and  $\pm \mathcal{U}H_i\mathcal{U}^{-1}$  are equally probable elements of the ensemble, an odd value of  $\Delta Q_{d-1}$  implies that the surface cannot be insulating, because the number of topologically gapless states has to be different from zero in this case. On the other hand, if  $\Delta Q_{d-1}$  is even, the ensemble symmetry does not prevent the insulating phase from appearing, and does not protect the surface states from localization.

We thus define  $\mathcal{Q} = (-1)^{\Delta Q_{d-1}}$  as the  $\mathbb{Z}_2$  topological invariant of an STI. The STI topological invariant  $\mathcal{Q}$  is a bulk property, e.g. the parity of the mirror Chern number, the weak or strong TI invariant. Nevertheless, the evaluation of  $\mathcal{Q}$  for large disorder strength is in general a hard problem, since it is necessary to find a symmetric  $H_{\text{bulk}}$  which can be connected to an  $H_i$  without closing the bulk gap.

This construction can be repeated in a recursive fashion as follows. Consider an ensemble of  $(d+1)$ -dimensional systems with a  $d$ -dimensional surface and a second statistical symmetry  $\mathcal{U}_2$  in addition to  $\mathcal{U}_1$ . The surfaces of the elements of this ensemble, if gapped, possess a  $d$ -dimensional STI invariant  $\mathcal{Q}$ , protected by the statistical symmetry  $\mathcal{U}_1$ . We may now ask whether protected gapless states appear at a  $(d-1)$ -dimensional boundary between the surfaces of two elements  $H_i^{(d+1)}$  and  $\pm \mathcal{U}_2 H_i^{(d+1)} \mathcal{U}_2^{-1}$  of the ensemble. In other words, we want to know if the boundary between the surfaces of  $H_i^{(d+1)}$  and  $\pm \mathcal{U}_2 H_i^{(d+1)} \mathcal{U}_2^{-1}$  is itself a protected surface of an STI. By following the same procedure of removing the disorder explained for the lower-dimensional case, the problem can be reduced to the study of the gap closings of a clean Hamiltonian  $H^{(d+1)} = H_{\text{bulk}}^{(d+1)} + \lambda_2 H_{s_2}$ , where  $\lambda_2 \in [-1, 1]$  and  $H_{s_2}$  strongly breaks the statistical symmetry  $\mathcal{U}_2$  but commutes with  $\mathcal{U}_1$ . The parity of the change  $\Delta \mathcal{Q}$  of the  $d$ -dimensional STI invariant is determined by the gap closings at  $\lambda_2 = 0$ . If  $\Delta \mathcal{Q}$  is odd, then topologically protected states must appear at the interface between the two surfaces, contradicting the assumption that the surfaces are gapped and topologically equivalent. Hence, the ensemble must have gapless surfaces, protected from localization by the combined presence of  $\mathcal{U}_1$  and  $\mathcal{U}_2$ . By repeatedly adding more symmetries and dimensions it is then possible to construct STIs in dimension  $d+n$  using an ensemble  $\mathbb{Z}_2^n$  symmetry and a  $d$ -dimensional

topological invariant.

### 7.3 STIs with reflection symmetry

Ensemble reflection symmetry allows us to construct a  $d$ -dimensional STI in any symmetry class which allows a non-trivial invariant in  $(d - 1)$  dimensions. Consider an infinite stack of  $(d - 1)$ -dimensional layers weakly coupled to each other. We alternate layers of  $A$ - and  $B$ -type characterized by bulk topological invariants  $Q_A$  and  $Q_B$  respectively. We take  $Q_B$  to be the inverse group element of  $Q_A$  (i.e.  $Q_B = -Q_A$  for  $\mathbb{Z}$  invariants and  $Q_B = Q_A$  for  $\mathbb{Z}_2$ ), so that coupling two layers results in a topologically trivial system. Such a model has a reflection symmetry with respect to each layer. Once short-ranged disorder is added, this symmetry is broken, and becomes an ensemble symmetry instead.

For a sufficiently weak disorder we may choose the clean system as  $H(\lambda = 0)$  and the symmetry-breaking perturbation  $H_s$  as a staggered interlayer coupling. The number of Fermi surfaces at the symmetric point equals  $|Q_A|$ , while at a finite value of  $\lambda$  the eigenstates of reflection symmetry couple (see supplementary material for details). Hence, if each layer carries an odd number of topologically protected edge states, the layered system is a nontrivial STI. This procedure allows one to construct tight-binding models showing an STI phase in any symmetry class.

### 7.4 Numerical Simulations

We have used the Kwant code [21] to perform numerical checks of our predictions. As an example of a two-dimensional STI we consider a stack of coupled Kitaev chains. The two dimensional lattice Hamiltonian of this system has the form

$$H = (2t \cos k_y - V)\sigma_z + \Delta\sigma_y \sin k_y + \alpha\sigma_x \sin k_x, \quad (7.1)$$

where  $\sigma_i$  are Pauli matrices in Nambu space, and  $x, y$  are integer coordinates perpendicular and along the chain direction. The Hamiltonian parameters are chosen as follows: the normal hopping is  $t = 1$ , the onsite disorder potential  $V$  is uniformly distributed in the interval  $[-\delta/2, \delta/2]$ , the  $p$ -wave pairing strength within each chain is  $\Delta = 1$ , and the interlayer coupling strength is  $\alpha = 0.45$ . This Hamiltonian belongs

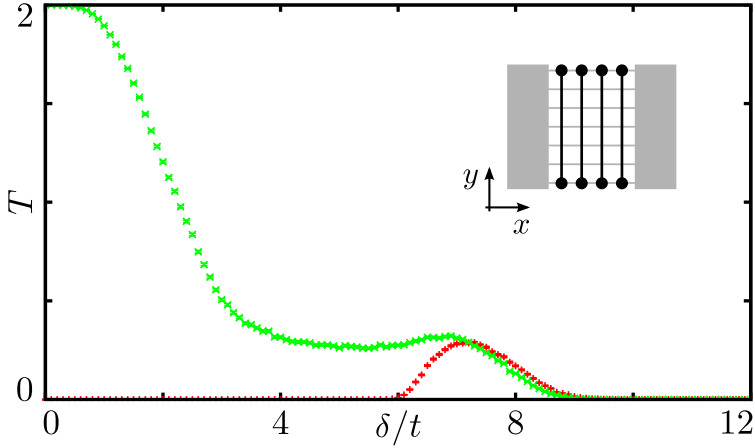


**Figure 7.2.** Transmission through a stack of 49 coupled Kitaev chains, each chain 150 sites long with hard wall (green) and periodic (red) boundary conditions versus disorder strength  $\delta$ . Each point is obtained by averaging over approximately  $6 \times 10^3$  disorder realizations, with error bars smaller than symbol sizes. The appearance of a finite transmission at high disorder strength in the case of periodic boundary conditions is the signature of a bulk gap closing, which we interpret as an STI-trivial insulator transition. The inset shows the sample geometry with Kitaev chains drawn as black lines, and with leads attached shown as gray rectangles.

to symmetry class D with particle-hole symmetry  $H = -\sigma_x H^* \sigma_x$ . It is also related to a Hamiltonian with an ensemble reflection symmetry by a gauge transformation  $\psi(x) \rightarrow (-1)^{\lfloor x/2 \rfloor} \psi(x)$ .

We have attached ideal leads to a stack of such Kitaev chains along the  $x$ -direction. In the  $y$ -direction we have used periodic or hard-wall boundary conditions. The calculated total quasiparticle transmission between the leads  $T = \text{Tr}(t^\dagger t)$  with  $t$  the transmission block of the scattering matrix is shown in Fig. 7.2. The clean system with  $\delta = 0$  and hard wall boundary conditions has transmission  $T = 2$  due to a non-chiral Majorana mode being present at each edge. This transmission is reduced by disorder, however it only disappears after the bulk goes through a delocalization transition to become a trivial Anderson insulator, as can be seen from the transmission with periodic boundary conditions.

To test the properties of the transmitting edges, we calculate the dependence of  $T$  on the number of Kitaev chains  $N$  at a fixed  $\delta$ . In order to

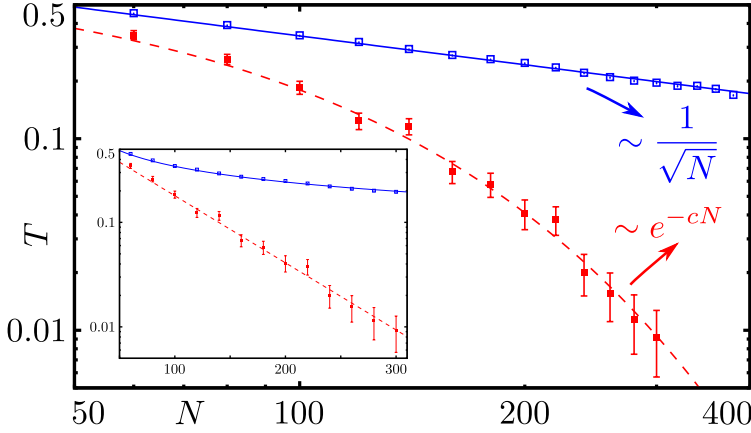


**Figure 7.3.** Transmission as a function of number of Kitaev chains (blue, solid line) or of number of BDI chains with  $Q = \pm 2$  (red, dashed line) in a stack. The inset shows the same curves in log-linear scale. In both cases, each point was obtained by averaging approximately  $2 \times 10^4$  disorder realizations with  $\delta = 3t$  and chain length of 40 lattice sites.

verify that it is the parity of the number of gap closings that determines whether an ensemble is an STI or not, we compare this result to the same calculation done for a reflection symmetric stack of chains in symmetry class BDI with alternating topological invariants  $Q = \pm 2$ . Our results are shown in Fig. 7.3. We find that  $T \sim N^{-1/2}$  for the stack of Kitaev chains, as expected for a chain of randomly coupled Majorana bound states (MBS), or more generally for 1D systems at the critical point [22–25]. Also in agreement with our expectations, we find that the edges of a BDI stack are localized with  $T \sim \exp(-cN)$ .

To test STIs in a dimension two higher than the dimension of the original topological invariant, we consider a triangular lattice of MBS [26–28], which is a surface model of a 3D array of coupled Kitaev chains. The tight binding Hamiltonian of this model is given by

$$H = \sum_{\langle ij \rangle} it_{ij} \gamma_i \gamma_j, \quad (7.2)$$

with real  $t_{ij} = -t_{ji}$ . If in a clean translationally invariant system with one MBS per unit cell the hoppings have equal magnitude, then the system has a reflection symmetry with respect to a plane passing through one



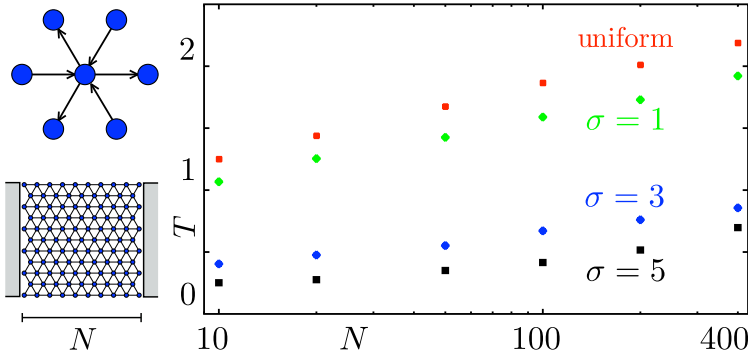


**Figure 7.4.** *Top left:* Arrows show the directions in a triangular Majorana lattice in which we choose the average hopping values to be positive. *Bottom left:* The setup in which we calculate transmission through disordered Majorana lattice. The leads are shown as grey rectangles. *Right:* Transmission through the Majorana lattice versus system size. The red curve corresponds to the case of hoppings  $t_{ij}$  uniformly distributed in a range  $[-t, 2t]$ . The other three curves correspond to log-normal distributed  $t_{ij}$ , with zero log-mean and different values of the log-variance  $\sigma$ .

of the hoppings and a reflection anti-symmetry ( $H$  changes sign) with respect to a perpendicular plane passing through any site. There are three Fermi surfaces (an odd number) in the clean system, hence any disorder that preserves the two reflection symmetries on average should make this lattice of MBS a surface model of an STI. The STI invariant in this system equals the parity of the number of MBS per unit cell.

We have calculated the total transmission through a square-shaped region of a disordered Majorana lattice for different types of disorder. Our results are shown in Fig. 7.4. We have found that transmission increases with system size for any disorder strength, confirming our expectations. Our results explain the thermal metal observed in Refs. [27, 28]. These two numerical works reported a metallic phase of a triangular Majorana lattice with random uncorrelated hopping signs. Since in that case the ensemble has the reflection symmetries described in the previous paragraph, the metallic phase is a consequence of it being a surface model of an STI. As a further confirmation of this topological origin, we have checked that removing the statistical symmetries via staggered hoppings causes a transition from positive to negative scaling (see supplementary material).

## 7.5 Conclusions and discussion

To conclude, we have unified several known examples of systems protected from localization by ensemble symmetries into the new class of statistical topological insulators. We were able to present a proof of why STIs avoid localization, by showing that the ensemble symmetry prevents them from having a definite value of a surface topological invariant. We have introduced a universal construction of STIs from any topological invariant using reflection symmetry, and were able to explain the thermal metal phase of Refs. [27, 28] as being a surface model of an STI. Since the identification of the bulk STI invariant with a gap closing relies on the regular TI invariant, STIs should be protected from interactions, as long as the interactions do not introduce spontaneous symmetry breaking with long-range correlations, as reported in Ref. [29] for weak TIs.

A natural extension of our approach would include providing a more complete relation between ensemble symmetry groups and STIs. While we have focused on  $\mathbb{Z}_2^n$  symmetries for simplicity, translational symmetries or antisymmetries must also be sufficient to construct STI, as is the case for the weak TIs, or also the triangular Majorana lattice. STIs using fractionalized phases may provide a new way to construct fractional topological insulators. The way the presence of several TI and STI phases in the same symmetry class enriches the phase diagram of Anderson insulators provides another interesting direction to study. Finally, we are as yet unable to solve the problem of efficiently evaluating the STI topological invariant on a general basis. It is sufficiently simple for several classes, e.g. weak TI, but becomes hard for more complicated ensemble symmetries.

## 7.6 Appendix

### 7.6.1 Tight-binding construction for statistical topological insulators with reflection symmetry

In this appendix we provide more details on the explicit tight-binding construction for statistical topological insulators based on ensemble reflection symmetry. As mentioned in the main text, we consider a stack of alternating  $(d - 1)$ -dimensional layers of two types  $A$  and  $B$ , charac-

terised by Hamiltonians  $H_A$  and  $H_B$ , shown in Fig. 7.5.  $H_A$  and  $H_B$  are in a symmetry class which in  $(d - 1)$  dimensions allows them to have a non-trivial topological invariant  $Q_A$  and  $Q_B$ . We consider in particular the case in which  $H_A$  and  $H_B$  carry opposite topological invariant  $Q_B = Q_A^{-1}$ , so that they have an equal number of topologically protected gapless states at the surface. For instance, in the unitary symmetry class with  $d = 2$ ,  $H_B$  may be the time-reversed partner of  $H_A$ , with an opposite Chern number. The alternating layers would then support  $|Q_A|$  chiral edge states propagating in opposite directions.

We consider a geometry where each layer is semi-infinite along one spatial dimension. The edge of each layer has  $(d - 1)$ -spatial dimensions, so that the whole stack has a  $d$ -dimensional surface. Let us denote with  $\psi_A$  and  $\psi_B$  the wave functions on layers of  $A$ - and  $B$ -type respectively. If the layers are coupled by a hopping  $h$ , the tight binding equations of the layered system take the form

$$E\psi_A = H_A\psi_A + h\psi_B + h^\dagger e^{-ik}\psi_B, \quad (7.3a)$$

$$E\psi_B = H_B\psi_B + h^\dagger\psi_A + h e^{ik}\psi_A, \quad (7.3b)$$

with  $k$  the momentum along the stacking direction. In matrix form, the tight-binding Hamiltonian  $H(k)$  is

$$H(k) = \begin{pmatrix} H_A & h + h^\dagger e^{-ik} \\ h^\dagger + h e^{ik} & H_B \end{pmatrix}, \quad (7.4)$$

acting on the Bloch wave function  $\Psi_k(x) = e^{ikx} (\psi_A, \psi_B)^T$ .

If the terms contained in  $h$  are much smaller than the bulk gap, as we will assume in the following,  $H_A$  and  $H_B$  can be chosen to be the effective surface Hamiltonians of the topologically protected surface states belonging to layers of type  $A$  and  $B$ , and the tight-binding equations (7.3) become an effective model for the surface shown in Fig. 7.5. We observe that since  $Q_B = Q_A^{-1}$ , it is always possible to choose a hopping term  $h$  without breaking any exact symmetry and such that  $H(k)$  is gapped for all  $k$ . This is not true, however, for hoppings which obey a reflection (anti-)symmetry with respect to the stacking direction. In this case,  $H(k)$  will have a number of gap closings determined by  $Q_A$ , as we will show in the following.

Let us denote with  $M$  a reflection operation with respect to an  $A$ -type

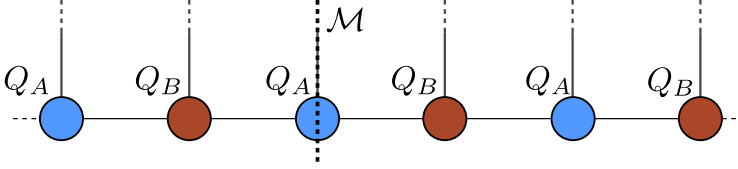


**Figure 7.5.** A stacked system consisting of infinitely many layers of two different types,  $A$  and  $B$ . The end of each layer is marked by an open circle (site), with adjacent stacks having staggered topological charges  $Q_A$  and  $Q_B$ . The system is translationally invariant, with a unit cell composed of two layers.

layer. The mirrored wave function  $M\psi_k(x)$  is given by

$$M\psi_k(x) = \begin{pmatrix} 1 & 0 \\ 0 & e^{-ik} \end{pmatrix} \psi_{-k}(x) \quad (7.5)$$

The mirrored Hamiltonian is

$$M^{-1}HM = \begin{pmatrix} 1 & \\ & e^{ik} \end{pmatrix} H(-k) \begin{pmatrix} 1 & \\ & e^{-ik} \end{pmatrix} \quad (7.6)$$

$$= \begin{pmatrix} H_A & h^\dagger + h e^{-ik} \\ h + h^\dagger e^{ik} & H_B \end{pmatrix} \quad (7.7)$$

Let us treat the case of a reflection symmetry first. The condition  $M^{-1}HM = H$  imposes  $h = h^\dagger$ , so that a reflection-symmetric Hamiltonian is given by

$$H(k) = \begin{pmatrix} H_A & h + h e^{-ik} \\ h + h e^{ik} & H_B \end{pmatrix}, \quad (7.8)$$

which, at  $k = \pi$ , becomes

$$H(\pi) = \begin{pmatrix} H_A & 0 \\ 0 & H_B \end{pmatrix}. \quad (7.9)$$

Clearly, due to the diagonal structure of  $H(\pi)$ , the number of zero energy eigenstates of  $H(\pi)$  is equal to twice the number of topologically protected states of  $H_A$  (or, equivalently, of  $H_B$ ), i.e. it is equal to  $2|Q_A|$ . Therefore,  $H(k)$  will possess  $|Q_A|$  (non-chiral) Fermi surfaces centered around  $k = \pi$ .

An odd value of  $|Q_A|$  leads to an STI phase in the presence of disorder with ensemble reflection symmetry. Depending on the details of the model, disorder which respects reflection symmetry on average can be introduced in the tight-binding equations (7.3) in either the onsite or hopping terms. For weak disorder, the STI invariant can be computed following the prescription in the main text, by choosing Eq. (7.8) as  $H_{\text{bulk}}$  and adding a reflection symmetry-breaking term  $\lambda H_s$ . An example of  $H_s$  is the term

$$H_s = \begin{pmatrix} 0 & h - he^{-ik} \\ h - he^{ik} & 0 \end{pmatrix}, \quad (7.10)$$

which introduces staggered hoppings  $h(1 + \lambda)$  and  $h(1 - \lambda)$  between alternating  $A$  and  $B$  layers.

For a reflection antisymmetry, on the other hand, we should impose the condition  $M^{-1}HM = -H$ , which in turn requires the substitution  $h = -h^\dagger$  before Eq. (7.8). The same reasoning then follows, only for zero energy eigenvalues at  $k = 0$  instead of  $k = \pi$ .

### 7.6.2 Localization on the Majorana triangular lattice by broken statistical reflection symmetry

To further investigate the role of statistical reflection symmetry in protecting the metallic phase of the 2D triangular Majorana lattice model, we have analyzed the same system with broken statistical reflection symmetry. In particular, we have introduced staggered hoppings in the way shown in the left panel of Fig. 7.6. Red, thick hoppings in the figure are stronger by a positive quantity  $t_1$  than the black, thin hoppings. We have considered this configuration in the presence of uniform disorder, for increasing values of the staggering  $t_1$ . A non-zero value of  $t_1$  breaks both statistical reflection symmetries that are present in the non-staggered lattice. In accordance with our expectations based on the STI origin of the thermal metal phase, we have observed a transition from positive to negative conductance scaling of the system as a consequence of the breaking of the statistical reflection symmetries, as shown in the right panel of Fig. 7.6.

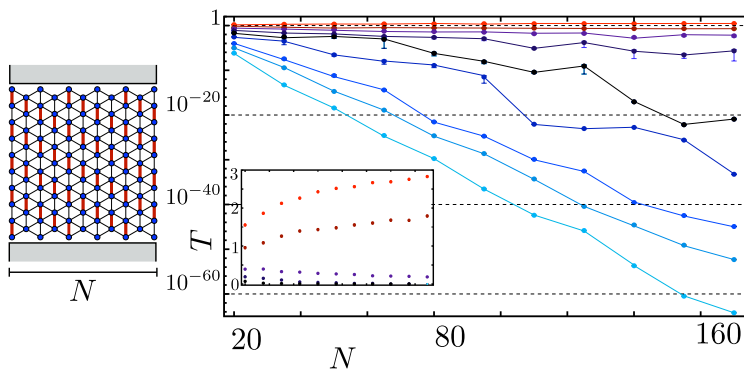


**Figure 7.6.** Left panel: triangular Majorana lattice with staggered hoppings. Red hoppings have strength  $t + t_1$ , with  $t$  the strength of the thin, black hoppings. Right panel: Transmission  $T$  as a function of system size  $N$ , for system with unit aspect ratio. Different colors correspond to different staggering strengths, with  $t_1/t = 2.6, 3.0, 3.1, 3.2, 3.3, 3.4, 3.6, 3.8, 4.2$  going from red to light blue, and top to bottom in the figure. In all cases, all hoppings have an additional disordered component, uniformly distributed with strength  $0.8t$ . Lines are guides for the eye. As the staggering is increased, the system localizes, with exponentially decaying transmission. The transition from positive to negative scaling is also shown in the inset, where the transmission axis has a linear scale. We show curves for  $t_1/t = 2.6, 2.8, 3.0, 3.1, 3.2$  going from top to bottom.

# Bibliography

- [1] M. Z. Hasan and C. L. Kane, *Rev. Mod. Phys.* **82**, 3045 (2010).
- [2] X.-L. Qi and S.-C. Zhang, *Rev. Mod. Phys.* **83**, 1057 (2011).
- [3] X.-L. Qi, T. L. Hughes, and S.-C. Zhang, *Phys. Rev. B* **78**, 195424 (2008).
- [4] S. Ryu, J. E. Moore, and A. W. W. Ludwig, *Phys. Rev. B* **85**, 045104 (2012).
- [5] Z. Wang, X.-L. Qi, and S.-C. Zhang, *Phys. Rev. B* **84**, 014527 (2011).
- [6] S. Ryu, A. P. Schnyder, A. Furusaki, and A. W. W. Ludwig, *New J. Phys.* **12**, 065010 (2010).
- [7] A. Yu. Kitaev, *AIP Conf. Proc.* **1134**, 22 (2009).
- [8] G. Volovik, *The Universe in a Helium droplet* (Oxford University Press, Oxford, 2003).
- [9] V. Gurarie, *Phys. Rev. B* **83**, 085426 (2011).
- [10] A. M. Essin and V. Gurarie, *Phys. Rev. B* **84**, 125132 (2011).
- [11] S. Ryu and T. Takayanagi, *Phys. Rev. D* **82**, 086014 (2010).
- [12] Z. Ringel, Y. E. Kraus, and A. Stern, *Phys. Rev. B* **86**, 045102 (2012).
- [13] R. S. K. Mong, J. H. Bardarson, and J. E. Moore, *Phys. Rev. Lett.* **108**, 076804 (2012).
- [14] L. Fu and C. L. Kane, *Phys. Rev. Lett.* **109**, 246605 (2012).

- [15] K. Nomura, S. Ryu, M. Koshino, C. Mudry, and A. Furusaki, *Phys. Rev. Lett* **100**, 246806 (2008).
- [16] J. T. Chalker and P. D. Coddington, *J. Phys. C* **21**, 2665 (1988).
- [17] L. Fu, *Phys. Rev. Lett.* **106**, 106802 (2011).
- [18] T. H. Hsieh, H. Lin, J. Liu, W. Duan, A. Bansil, and L. Fu, *Nat. Comm.* **3**, 982 (2012).
- [19] It is interesting to note that although STI's do not seem possible in 1D, there is a precursor to the STI phase transition in a half-filled Anderson chain [30].
- [20] J. C. Y. Teo and C. L. Kane, *Phys. Rev. B* **82**, 115120 (2010).
- [21] C. W. Groth, M. Wimmer, A. R. Akhmerov, and X. Waintal, *arXiv:1309.2926* (2013).
- [22] P. W. Brouwer, A. Furusaki, I. A. Gruzberg, and C. Mudry, *Phys. Rev. Lett.* **85**, 1064 (2000).
- [23] P. W. Brouwer, A. Furusaki, and C. Mudry, *Phys. Rev. B* **67**, 014530 (2003).
- [24] O. Motrunich, K. Damle, and D. A. Huse, *Phys. Rev. B* **63**, 224204 (2001).
- [25] I. A. Gruzberg, N. Read, and S. Vishveshwara, *Phys. Rev. B* **71**, 245124 (2005).
- [26] R. R. Biswas, L. Fu, C. R. Laumann, and S. Sachdev, *Phys. Rev. B* **83**, 245131 (2011).
- [27] Y. E. Kraus and A. Stern, *New J. Phys.* **13**, 105006 (2011).
- [28] C. R. Laumann, A. W. W. Ludwig, D. A. Huse, and S. Trebst, *Phys. Rev. B* **85**, 161301(R) (2012).
- [29] C.-X. Liu, X.-L. Qi, S.-C. Zhang, *Physica E* **44**, 906-911 (2012).
- [30] M. Kappus and F. Wegner, *Z. Phys. B* **45**, 15 (1981).



# Samenvatting

Aan het oppervlak van een materiaal, of op het grensvlak tussen twee materialen, vind men meestal oppervlakte-toestanden. Het bijzondere aan topologische isolatoren en topologische supergeleiders is dat deze toestanden zo robuust zijn. Ze ontstaan niet “toevallig”, maar ze zijn onvermijdelijk en kunnen niet verdwijnen door vervorming van het materiaal — zo lang als bepaalde fundamentele symmetrieën van het systeem behouden blijven. Om deze reden noemen we de oppervlakte-toestanden “topologisch beschermd”. Het onderwerp van dit proefschrift is de karakterisatie van topologisch beschermde toestanden, met de nadruk op hun effect op elektrische geleiding in de aanwezigheid van wanorde.

Het ontstaan van geleidende oppervlakte-toestanden in een isolerend materiaal kan begrepen worden in termen van een zogenaamde topologische invariant — dat is een getal wat bepaald wordt door de bandstructuur en het aantal oppervlakte-toestanden telt. Een oud en bekend voorbeeld is de zogenaamde TKNN of Chern-invariant, die berekend wordt door Bloch golffuncties te integreren over de Brillouinzone. Translatie-invariantie is hiervoor noodzakelijk, dus deze invariant kan niet uitgerekend worden in de aanwezigheid van wanorde.

In experimenten is wanorde onvermijdelijk en is translatie-invariantie gebroken. Om deze reden leiden we in hoofdstuk 2 en 3 alternatieve uitdrukkingen af voor de topologische invariant, die geen gebruik maken van translatie-invariantie maar uitgaan van de verstrooiingsmatrix. Een bijkomend voordeel is dat deze nieuwe formule efficiënter uit te rekenen is dan de integraal over de Brillouinzone, omdat alleen eigenschappen bij een enkele energie nodig zijn (de Fermi-energie). De grotere efficiëntie maakt het mogelijk om grotere, meer realistische systemen te beschouwen.

Er is nog een voordeel aan de aanpak die uitgaat van de verstrooiingsmatrix, en dat is dat er een direct verband is met transporteigenschappen (zoals elektrische geleiding). In hoofdstuk 3 laten we zien dat het verband tussen Chern-invariant en de polen en nulpunten van de verstrooiingsmatrix de geleidingsfluctuaties van orde  $e^2/h$  kan verklaren. Bovendien vinden we zo een nieuwe methode om de kritische exponent van de fase-overgang in het quantum Hall-effect te berekenen (zie hoofdstuk 4).

In het eerste deel van het proefschrift staan de topologische invarianten centraal, en in het tweede deel onderzoeken we de eigenschappen en de stabiliteit van de topologische toestanden. Wederom maken we hierbij gebruik van verstrooiingstheorie.

In hoofdstuk 5 onderzoeken we de fase-overgangen in een tweedimensionale topologische supergeleider in aanwezigheid van tijdsomkeersymmetrie. We bepalen de systeemgrootte-afhankelijkheid van de elektrische geleiding en berekenen de kritische exponenten van de fase-overgang tussen een toestand met en een toestand zonder oppervlakte-toestanden.

Een onderwerp dat de laatste tijd sterk in de belangstelling heeft gestaan, is de detectie van Majorana-deeltjes aan de uiteinden van een supergeleidende draad. Een piek in het geleidingsvermogen rond spanning nul zou een aanwijzing voor deze deeltjes zijn. De huidige experimenten hebben iets van "trial and error", er ontbreekt een systematische manier om de Majorana-deeltjes op te roepen. In hoofdstuk 6 stellen we een methode voor, die gebruik maakt van het geleidingsvermogen om Majorana-deeltjes als het ware van de grond af te construeren.

Tenslotte analyseren we in hoofdstuk 7 wat het effect is van wanorde op de stabiliteit van de topologische fase. We hebben ontdekt dat, zelfs als de fundamentele symmetrieën door de wanorde verbroken zijn, de topologische fase toch kan blijven bestaan mits die symmetrieën na middelling over de wanorde behouden blijven. We spreken van een "statistische" topologische isolator. Deze ontdekking is een belangrijke uitbreiding van het type systemen waar topologische fasen gevonden kunnen worden.

# Summary

At the surface of a material, or at the interface between two of them there usually are surface states. What makes topological insulators and superconductors remarkable is the robustness of these states. Rather than being accidental, they are expressions of bulk properties, and cannot be removed by smooth deformations of the system as long as the bulk gap is maintained, and the symmetries of the system, if any, are not violated. In this sense, the protection is topological in nature. This thesis deals mainly with the characterization of topologically non-trivial phases as well as the transitions to and between them, with a focus on transport properties and the effects of disorder.

The correspondence between the gapped bulk and the conducting edges can be understood in terms of topological invariants, expressions determined from the bulk and which essentially count the number of protected edge states. Initially, topological quantum numbers were obtained in the framework of band theory, as was the case of the TKNN or Chern invariant, which was computed as an integral of translationally invariant Bloch wave functions over the Brillouin zone.

In experiments however, the presence of disorder is unavoidable and leads to the breaking of translational symmetry. Motivated by this fact, in Chapters 2 and 3 we derived expressions for the topological invariants of systems without making use of translational invariance, but starting from the scattering matrix. Not only is this approach naturally tailored to the study of disordered systems, but it is oftentimes numerically easier to evaluate than Hamiltonian expressions. Only the scattering matrix at the Fermi level is needed, as opposed to the full spectrum and/or wave functions of the Hamiltonian below the Fermi energy, leading to an efficient evaluation and the possibility of numerically studying larger systems.

Another advantage of the computation of a topological invariant in terms of the scattering matrix is the connection to transport properties and the scaling theory of localization. The understanding of the Chern number in terms of the zeros and poles of the reflection matrix determinant, as done in Chapter 3, leads to the prediction of  $e^2/h$  oscillations in bulk conductance along the phase transition line. Also, it provides a novel scaling variable that allows to estimate the critical exponent of the quantum Hall transition without the need to include corrections in the form of irrelevant scaling variables. Both these features are explored in Chapter 4.

The second half of this thesis moves away from scattering formulations of topological invariants, and focuses mainly on the description of the properties and stability of topological phases. Here too, scattering theory proves to be a powerful tool.

In the fifth chapter we look at the universal properties of phase transitions in two-dimensional helical topological superconductors. We study the behavior of conductance with varying system size in a model which was introduced directly in terms of its scattering matrix. We characterize the phase transitions which appear, computing the relevant and irrelevant critical exponents, as well as the critical conductance.

Away from the transitions, inside topological phases of matter, transport signatures may be used to analyze their characteristics. This is especially important given that conductance is an experimentally accessible observable, and indeed much attention has been given to the transport signature of Majorana fermions, the zero bias peak.

In Chapter 6, we go beyond the examination of the zero bias peak as an indicator for Majoranas, using conductance measurements to adaptively tune a realistic system deep into the topological phase. We model a one-dimensional topological superconductor in a bottom-up fashion, so that individual subsections can be independently addressed, depending on the input that is provided by resonant Andreev conductance spectroscopy.

Finally, in Chapter 7 we analyze the robustness of topological phases and their surface states to the presence of disorder. We find that even if disorder breaks the symmetries that protect the conducting surface, it can still persist as long as disorder preserves those symmetries on average. This opens the hunt for new non-trivial phases, those protected by an average symmetry, some of which can be identified by their atyp-

ical transport properties, such as a conductance scaling characteristic of lower-dimensional systems.



# List of Publications

- *Two case studies of post – seismic regime in The Vrancea Region*, C. Ciucu and C. Fulga, Romanian Rep. Phys. **60**, 173 (2008).
- *Background analysis of field-induced electron emission from nanometer scale heterostructured emitters*, V. Filip, D. Nicolaescu, I. C. Fulga, T. Mitran, and H. Wong, J. Vac. Sci. Technol. B **27**, 711 (2009).
- *Nonzero temperature effects on antibunched photons emitted by a quantum point contact out of equilibrium*, I. C. Fulga, F. Hassler, and C. W. J. Beenakker, Phys. Rev. B **81**, 115331 (2010).
- *Scattering formula for the topological quantum number of a disordered multi-mode wire*, I. C. Fulga, F. Hassler, A. R. Akhmerov, and C. W. J. Beenakker, Phys. Rev. B **83**, 155429 (2011) [Chapter 2].
- *Topological quantum number and critical exponent from conductance fluctuations at the quantum Hall plateau transition*, I. C. Fulga, F. Hassler, A. R. Akhmerov, and C. W. J. Beenakker, Phys. Rev. B **84**, 245447 (2011) [Chapter 4].
- *Scattering theory of topological insulators and superconductors*, I. C. Fulga, F. Hassler, and A. R. Akhmerov, Phys. Rev. B **85**, 165409 (2012) [Chapter 3].
- *Thermal metal-insulator transition in a helical topological insulator*, I. C. Fulga, A. R. Akhmerov, J. Tworzydło, B. Béri, and C. W. J. Beenakker, Phys. Rev. B **86**, 054505 (2012) [Chapter 5].
- *Adaptive tuning of Majorana fermions in a quantum dot chain*, I. C. Fulga, A. Haim, A. R. Akhmerov, and Y. Oreg, New J. Phys. **15**, 045020 (2013) [Chapter 6].

- *Statistical Topological Insulators*, I. C. Fulga, B. van Heck, J. M. Edge, and A. R. Akhmerov, arXiv:1212.6191 [Chapter 7].
- *Phase-locked magnetoconductance oscillations as a probe of Majorana edge states*, M. Diez, I. C. Fulga, D. I. Pikulin, M. Wimmer, A. R. Akhmerov, and C. W. J. Beenakker, Phys. Rev. B **87**, 125406 (2013).
- *Flux-controlled quantum computation with Majorana fermions*, T. Hyart, B. van Heck, I. C. Fulga, M. Burrello, A. R. Akhmerov, and C. W. J. Beenakker, Phys. Rev. B **88**, 035121 (2013).
- *Effects of disorder on Coulomb-assisted braiding of Majorana fermions*, I. C. Fulga, B. van Heck, M. Burrello, and T. Hyart, arXiv:1308.0244.
- *Topological phase transitions driven by non-Abelian gauge potentials in optical square lattices*, M. Burrello, I. C. Fulga, E. Alba, L. Lepori, and A. Trombettoni, arXiv:1308.0750.
- *Quantum phase transitions of a disordered antiferromagnetic topological insulator*, P. Baireuther, J. M. Edge, I. C. Fulga, C. W. J. Beenakker, J. Tworzydło, arXiv:1309.5846.



# Curriculum Vitæ

I was born in Bucharest, Romania, on the 2<sup>nd</sup> of October 1986, where I completed my primary, secondary, and high school education. In 2004, while attending the George Cosbuc bilingual high school, I won the National Public Speaking Competition, organized by the English Speaking Union.

After graduating in 2005, I started studying physics at the Faculty of Physics of the University of Bucharest. During my bachelor studies I worked on research projects under the guidance of Prof. Valeriu Filip, and the late Prof. Cristian Ciucu. I graduated in 2008 cum laude, writing a bachelor thesis under the supervision of Prof. Virgil Băran, entitled “Transport Phenomena in Mesoscopic Systems: the Role of Quantum Effects”.

After receiving my B.Sc. in Bucharest, I spent a short time at the Laboratoire de Physique Corpusculaire in Clermont-Ferrand, France, doing a research internship on “Research beyond the Standard Model”. Afterwards I moved to Leiden, where I enrolled in the Physics Master Program of Leiden University, track Theoretical Physics. During my Master’s studies I worked as a student assistant for Leiden University, was awarded the Leiden University Fund scholarship, and received the Shell Stipend for Theoretical Physics. With a Master’s thesis supervised by Prof. Carlo Beenakker and titled “Anti-bunched photons emitted by a Quantum Point Contact”, I received an M.Sc. cum laude in 2010.

After completing my Master’s education I remained in the group of Prof. Carlo Beenakker for my Ph.D. studies, being employed by the Foundation for Fundamental Research on Matter (FOM). Part of the research I performed during the last three years is presented in this thesis.

During my Ph.D. studies I was a teaching assistant in the course “Statistical and Thermal Physics 2”, taught by Prof. Helmut Schiessel. I attended multiple schools, workshops and conferences, presenting my work in The Netherlands, Italy, and Germany.

# Stellingen

behorende bij het proefschrift

*Scattering theory of topological phase transitions*

1. The topological properties of a disordered system can be determined without knowing its spectrum.  
Chapter 3
2. Finite size corrections at the quantum Hall plateau transition can be greatly reduced by choosing a scaling function that changes sign across the transition.  
Chapter 4
3. The critical exponent for the divergence of the localization length in a helical topological superconductor is twice that of a chiral topological superconductor.  
Chapter 5
4. Some topological insulators are protected by symmetries that are only present on average.  
Chapter 7
5. In a Corbino geometry, magnetoconductance oscillations can distinguish between Dirac and Majorana edge modes.  
M. Diez, I. C. Fulga, D. I. Pikulin, M. Wimmer,  
A. R. Akhmerov, and C. W. J. Beenakker,  
Phys. Rev. B **87**, 125406 (2013)
6. Majorana bound states can be braided without moving them.
7. Zhang and Hu's four-dimensional quantum Hall effect is a quantum spin Hall effect *avant la lettre*.  
S. C. Zhang and J. Hu, Science **294**, 823 (2001)
8. The 125 GeV mass of the Higgs Boson implies that vacuum is analogous to a *type-II* superconductor.
9. Video games are a great way of learning mathematics and physics.

Ion Cosma Fulga  
Leiden, November 21<sup>st</sup>, 2013